Some applications of Nonlinear Physics to Ocean Dynamics:
from Lagrangian Chaos to Genetic Algorithms.

Cristóbal López
Departamento de Física Interdisciplinar,
Instituto Mediterráneo de Estudios Avanzados (IMEDEA).

12 de Septiembre de 2000

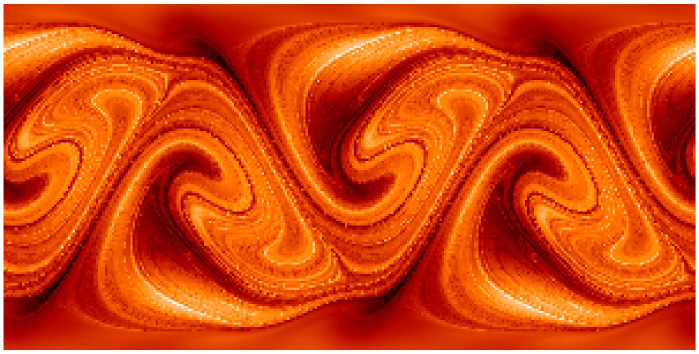

Memoria presentada por
Cristóbal López Sánchez en el Departamento
de Física de la Universidad de las Islas Baleares
para optar al grado de Doctor en Ciencias Físicas.

La presente Tesis ha sido dirigida
por el Doctor *Emilio Hernández García*.

Contents

Emilio Hernández García, profesor titular del Dpto. de Física de la Universidad de las Islas Baleares,

CERTIFICA

que la presente memoria ha sido realizada por Cristóbal López Sánchez bajo su dirección en este departamento y que constituye su Tesis para optar al título de Doctor en Ciencias Físicas.

Y, para que conste, firma la presente en Palma de Mallorca a 12 de Septiembre de 2000.

Emilio Hernández García

Agradecimientos

Quisiera expresarle mi más sincero agradecimiento a Emilio. Siempre tuvo tiempo para conversar conmigo o sentarse a mi lado a hacer cálculos, y, además, su contagiosa ilusión por la Ciencia ha sido y es un grato y continuo estímulo; todavía me sigue sorprendiendo no haberle visto un solo día de mal humor desde que le conozco. Asimismo, agradezco a Pedro que confiara en mí y que guiara mis primeros pasos en la investigación científica. Realmente, me siento un privilegiado por haber tenido la oportunidad de colaborar con dos científicos tan brillantes y aun mejores personas.

Zoltán Neufeld has played a fundamental role in the development of this Thesis. I warmly acknowledge him all our discussions, his ideas and the time he spent trying to solve my doubts. También agradezco a Alberto Álvarez nuestras fructíferas y amenas conversaciones, que espero que se prolonguen en el futuro.

Una sonrisa me ilumina la cara cuando pienso en todos los buenos momentos que he tenido la suerte de compartir con los compañeros de este singular espacio vital llamado ’*F*’, así como con los antiguos compañeros de Granada. Les agradezco profundamente que hayan convertido la rutina diaria en algo ameno y muy divertido.

También hago extensivo mi agradecimiento a todos los miembros del grupo de Física Estadística y No lineal de Mallorca; son muchas las cosas que he aprendido de ellos. I also want to acknowledge all the members of the TNT group in Rome their warm hospitaly.

Por último, dedico esta memoria a los que más quiero: a mis amigos, los de siempre, por estar ahí; a Alejandra, por su sonrisa, por existir; a mis hermanos, Paco (y familia), José y M. Isabel. Pero sobretodo quisiera dedicar este trabajo a mi tía y mis padres. Ellos son un ejemplo constante de esfuerzo, ilusión y generosidad, y dado que estas cosas no se suelen decir a diario, quisiera aprovechar unas líneas para recordarles todo el amor y cariño que les tengo.

But when I knew him, he was a desiccated little old man, well past doing any scientific work. Intellectual strength had left him forever, but not the desire, the fascination, which are at the root of scientific work. When he could corner some colleague at the university, he would tell the unfortunate about his research on the ds^2 *of music or the mathematical theory of the shape of the liver. Indeed, music, shapes, and forms are recurrent themes that fascinate scientists. Here are some others: time and its irreversibility, chance and randomness, life. There is one phenomenon -the motion of fluids- that seems to reflect and combine all these themes. Think of air flowing through organ pipes, of water forming eddies and whorls perpetually changing and moving as if they had their own free will. Think of volcanic eruptions, think of wells and cascades.*

Chance and Chaos
David Ruelle

Chapter 1

Introduction

An important breakthrough in the development of chaotic dynamics appeared with the original work of Lorenz [1]. With the aim of weather forecasting, he proposed his now well-known model as a low dimensional (three coupled ordinary differential equations) approximation to an infinite dimensional model (a partial differential equation) of the dynamical evolution of the atmosphere. Thus, the impact of Chaos theory or Nonlinear Dynamics on Geophysical fluid dynamics, i.e., fluid mechanics as it is applied to atmospheric or oceanic systems, has been important even since the first steps of this new field of Science. Briefly, *this Thesis will be concerned with some possibly useful applications of different mathematical, computational and physical tools coming from Nonlinear Dynamics to specifically motivated oceanic problems*. Of course, this is a very general assertion which we will try to clarify along this introduction.

Therefore, several things have to be pointed out. First, the subjects of our studies, the formerly called *motivated oceanic problems*: these will be phenomena of physical, biological or chemical origin that can happen in the ocean and where, obviously, the transport produced by the oceanic fluid flow is of primary importance. Two different kinds of these will be considered in our work: a) the so-called *passive tracers*, which are any physical, biological or chemical substances that are driven by a flow, producing no feedback action on the flow dynamics, and which lack of their own intrinsic dynamics. An example of this type of magnitude that is just transported by the flow is a dye which marks the fluid or also, in the case that they do not modify significantly the density of the fluid, the temperature or the salinity of sea water. On the contrary, b) *active tracers* are substances advected by a flow (also without modifying it) with possess their own dynamics. Examples are any biological species, for e.g. plankton communities, obeying certain population dynamics rules, or ozone or any chemical pollutants undergoing some chemical reaction dynamics.

We have to mention that this nomenclature (the one we are using in this work) is not standard, i.e., sometimes the names *active or passive* refer to substances that are transported by a flow *with or without* modifying it, respectively. Moreover, both active and passive (in the last sense) substances can be reacting if they have their own dynamics, or nonreacting when this is not the case.

An important remark is the fact that we are explicitly studying the influence of oceanic flows. This comes from two different considerations, first because we explicitly study, in some of the Chapters, real data of the oceanic surface and second, when we deal with mathematical models of flows, these are two-dimensional and incompressible. This is a good approximation for geophysical flows in a certain range of scales [2]. Concerning bidimensionality: horizontal scales are much larger than the vertical scale for the Earth's atmosphere and oceans, and, also, it can be shown that one of the effects of rotation is to induce two-dimensionality in the flow. This effect is known as the *Taylor-Proudman* theorem and essentially establishes that uniform rotation of a plane layer of fluid about an axis perpendicular to the plane (z axis) tends to lock the fluid into two-dimensional flow independent of z. In addition, incompressibility, that is, the conservation of the fluid density following the flow, is a very good assumption for liquids and, therefore, for ocean dynamics. Moreover, due to the *continuity equation* for the fluid density, the incompresibility condition reduces to $\nabla \cdot \mathbf{v} = 0$, where $\mathbf{v}$ is the fluid velocity field.

Therefore $2d$ incompressible fluid flows are widely used in models of the atmosphere and the ocean. In these, three-dimensionality is, quite often, approached by considering different layers of fluid with different densities, and where the flow is assumed to be $2d$ in every layer. In fact, rotation and stratification are the two striking ingredients of geophysical flows [2, 3].

Now, once we have introduced the subjects of our work, that is, *active or passive tracers advected by two-dimensional incompressible flows*, we will try to argue why Nonlinear Dynamics or Chaos Theory can be useful when treating geophysical phenomena and which are the particular tools used in this work to try to better understand, model, and predict these. In our opinion, the main reason for the usefulness of Nonlinear Dynamics is obvious: the ocean is turbulent, i.e. it is disordered in space and time, and disordered systems are the subject of study of Chaos Theory. More precisely, we believe that the following features of turbulent or spatiotemporal chaotic systems are at the heart of the success of the nonlinear dynamics approach:

- A fundamental characteristic of turbulence is that it is hard to predict: a small uncertainty at a given initial time will amplify so as to render impossible, after a long enough time, a precise deterministic prediction of its evolution. However, some order is always present in turbulent phenomena: winter always follows summer in a predictable pattern, for example. It is worth to say that this *order within chaos* is one of the main features of chaotic systems.

  In the ocean, the exponential separation of fluid particles trajectories is a property that has been empirically observed with the throwing of floating buoys, and which has deserved much attention mainly because, before the arrival of satellite images of large areas of the ocean, empirical data of oceanic magnitudes where obtained measuring directly by immersing the experimental set into the ocean.

- The existence of localized spatiotemporal structures (the so-called coherent structures), like vortices or jets. Specifically, the recognition of the relevant role of these has allowed, when the dynamical processes are dominated by the coherent structures, the reduction of the very high number of degrees of freedom in turbulent flows. The idea here is to reduce the full flow dynamics to the dynamics of the coherent structures, i.e., to create a low-dimensional model (a system of ordinary differential equations) of the turbulent flow by just resolving these structures, and in the study of these low-dimensional approximations is where nonlinear dynamics may enter in the game.

- To end with this argumentation, we mention the most successful tool, in our opinion, in the field of the applications of nonlinear dynamics to chaotic systems in general: *nonlinear data analysis*. Mathematical concepts like fractal dimensions, Lyapunov exponents, embedding, etc..., are being widely used in any kind of data sets to characterize and make predictions about future states of the system. However, in the context of spatially extended chaotic systems, like it is the case of the ocean, nonlinear data series analysis is still in its beginnings. In addition, the availability of large real (not from numerical simulations) spatiotemporal data sets in general, and of tubulent flows in particular, is nowadays rather poor; but since the launch of different satellite missions this situation is changing, opening a new era in the knowledge of ocean dynamics.

Up to now we have indicated the subjects of our work and some of the reasons for the use of nonlinear dynamics tools in the study of these. The obvious next step is to introduce the particular mathematical and physical concepts used along our work and then to point out some of the results. About these, we can say that they are promising, otherwise this Thesis could not have been completed, and they will be detailed in the subsequent Chapters. Concerning the principal tools we have used, key words in our work are: *Eulerian and Lagrangian descriptions of fluid motion, Lagrangian Chaos, the Proper Orthogonal Decomposition and Genetic Algorithms*. Other more particular concepts playing a fundamental role in this Thesis are: *Lyapunov exponents, multifractality and quasigeostrophic dynamics*, which will not be presented now and we remit the reader to the widely existing literature about them ([2], [3], [4] and references therein). Therefore, and despite the fact that they are discussed in some of the different Chapters, we next proceed to the introduction of these principal tools with the aim of providing the reader a general overview of the context of our work.

1.1 Some basic concepts and tools

1.1.1 Eulerian and Lagrangian descriptions

The description of fluid motion can be addressed following two different ways. One can deal at any time with velocity, pressure and density fields at any spatial point in the fluid, or either, one deals with the trajectory of each *fluid particle*. The first approach is usually called *Eulerian* and the second one *Lagrangian*. In principle both are equivalent, and if we denote by $\mathbf{v}(\mathbf{x}, t)$ the Eulerian velocity field, which tells us the value of the fluid velocity at any space-time point $(\mathbf{x}, t)$, then the motion of a fluid particle with initial localization $\mathbf{x}(0)$ is given by

$$\frac{d\mathbf{x}}{dt} = \mathbf{v}(\mathbf{x}, t). \tag{1.1}$$

The expression (1.1) establishes the physical connection between the Eulerian and Lagrangian descriptions. It clearly reads that when a particular fluid particle is known to be at a specific space-time point, its Lagrangian velocity must be equal to the Eulerian field value at that space-time point.

1.1.2 Lagrangian Chaos

In a first part of this memory we will be interested in the transport of substances by flows yielding *Lagrangian chaos*, concept which is related with the formerly mentioned unpredictable character of oceanic flows. Let us briefly mention some ideas about this concept of Lagrangian chaos, also called Lagrangian turbulence or chaotic advection [5], [6]. One speaks of Lagrangian chaos when (1.1) has a sensitive dependence on initial conditions, i.e., initially nearby trajectories diverge exponentially fast. It is important to note that Lagrangian chaos can appear even in flows which are not turbulent in the Eulerian description. Restricting ourselves to the situation of a two-dimensional incompresible flow (the one of interest along our work): $\mathbf{v}(\mathbf{x}, t) = v_x(x, y, t)\hat{x} + v_y(x, y, t)\hat{y}$. Then, the incompressibility condition, $\nabla \cdot \mathbf{v} = \partial v_x/\partial x + \partial v_y/\partial y = 0$, means that we can express $\mathbf{v}$ in terms of a *stream function* $\psi(x, y, t)$,

$$v_x = -\frac{\partial \psi}{\partial y} \tag{1.2}$$

$$v_y = \frac{\partial \psi}{\partial x} \tag{1.3}$$

Now, the motion of a fluid particle given by (1.1) is written in terms of the stream function as:

$$\frac{dx}{dt} = -\frac{\partial \psi}{\partial y} \tag{1.4}$$

$$\frac{dy}{dt} = \frac{\partial \psi}{\partial x}. \tag{1.5}$$

Moreover, the form of the above equations resembles that of a one-degree-of-freedom Hamiltonian system, if we identify the stream function with the Hamiltonian, x with the momentum p, and y with the position q. If $\psi = \psi(x, y, t)$ is time-dependent, Eqs. (1.4, 1.5) are a time-dependent two-dimensional system of ordinary equations. Standard theorems [7] state that chaotic solutions for the above system of equations are likely to occur for particular values of the system parameters. In Hamiltonian dynamics this is the so-called *Hamiltonian Chaos*; that is, Lagrangian chaos, chaotic advection or Hamiltonian chaos are equivalent concepts or approaches, and the tools, theorems, etc., developed for the study of any of these are completely similar in the others.

Hamiltonian systems are just a particular, but very important, type of dynamical systems. In any case, some fundamental concepts coming from Hamiltonian dynamics deserve a further consideration, though we remit to the huge literature on this topic for a deeper insight [8], [9]. First, a most relevant property of these systems is that since they conserve phase space volume (there is no dissipation of energy), they do not possess attractors of the dynamics. Another very important characteristic is that of integrability.

Briefly, a Hamiltonian system with N degrees of freedom is integrable if and only if N independent integrals of the motion exist. More formally, a system with a time-independent Hamiltonian $H(q_i, p_i)$ with N degrees of freedom, i.e., $i = 1, ...N$, is said to be integrable if there exist N independent, smooth constants of motion I_i,

$$\frac{dI_i}{dt} = 0, \tag{1.6}$$

that are in *involution*,

$$[I_i, I_j] = 0, \tag{1.7}$$

where $[,]$ is the Possion bracket, that is,

$$[f, g] = \frac{\partial f}{\partial q_i}\frac{\partial g}{\partial p_i} - \frac{\partial f}{\partial p_i}\frac{\partial g}{\partial q_i}. \tag{1.8}$$

The reason that the constants are required to be smooth and independent is that the equations $I_i = c_i$, where the c_i's are constants, must define N different surfaces of dimension $2N - 1$ in the $2N$-dimensional phase space. The reason for the constants to be in involution is that one wants to use the I's (or combinations of them) as momenta, and momenta must pairwise commute. In coordinates of this type the motion is quite simple.

Sometimes additional requirements are added in definitions of integrability. For example, one can add the requirements that the surfaces $I_i = c_i$ for $i = 1, 2, ..., N$ be compact and connected. If this is the case the motion takes place on an N-torus and there exist *action-angle variables* (J_i, Θ_i) in terms of which Hamilton's equations have the form

$$\frac{dJ_i}{dt} = -\frac{\partial H}{\partial \Theta_i} = 0, \quad \frac{d\Theta_i}{dt} = \frac{\partial H}{\partial J_i} = \Omega_i(\mathbf{J}), \tag{1.9}$$

where $i, j = 1, 2, ..., N$. The second of Eqs. (1.9) is easy to integrate, yielding

$$\Theta_i(t) = \Theta_i(0) + \Omega_i(\mathbf{J})t, \tag{1.10}$$

where Θ is defined *modulo* 2π, and $\Omega_i(\mathbf{J}) \equiv \frac{\partial H}{\partial J_i}$ are the frequencies of motion around the N-torus.

Therefore, an integrable system is characterized by regular trajectories in phase space. Moreover, the trajectories of an N degrees-of-freedom system in the phase space are restricted to lie on a N-dimensional torus, as it is clear from Eq. (1.10). Thus, for integrable systems, we can view the phase space as being completely occupied by N-tori almost all of which are in turn filled by quasiperiodic orbits. Most interesting for us are the nonintegrable or chaotic Hamiltonian systems, just because they are close, in fact they are equivalent, to incompressible fluid systems yielding Lagrangian chaos (with the above mention substitution of real space coordinates of the flow with the phase space coordinates, and stream function with Hamiltonian). These are characterized by irregular or stochastic trajectories in phase space or, exploiting further the equivalence with fluid flows, irregular trajectories of fluid particles in real space. Of a great theoretical relevance are the weakly nonintegrable systems, or in other words, integrable systems that have been slightly perturbed. In these, the Kolmogorov-Arnold-Moser (KAM) theorem establishes the coexistence at all scales of regions of regular trajectories, the so-called KAM tori, and regions of stochastic trajectories. The stronger the perturbation from integrability the smaller the number of surviving KAM tori. These are very important in the context of fluid motion since they can act as transport barriers for the flow, decreasing the mixing properties of the fluid.

As an example of the KAM theorem, we show in Fig. 1.1 the phase space of a nonintegrable system. In particular, the trajectories shown in Fig. 1.1 have been obtained by iterating a Hamiltonian map, that is, a discrete-time version of a Hamiltonian system [4], known as the *standard map*. This is a two-dimensional map defined in the square $[0, 2\pi] \times [0, 2\pi]$ and given by:

$$x_{n+1} = (x_n + K \sin y_{n+1}) \bmod 2\pi \tag{1.11}$$

$$y_{n+1} = (y_n + x_n) \bmod 2\pi. \tag{1.12}$$

When $K \neq 0$ the standard map (1.11,1.12) is not integrable. Moreover, as it is shown in Fig. 1.1, the larger K the less the number of regular trajectories (KAM tori, which in the present case of two dimensions are circular trajectories) in the phase space.

1.1.3 The Proper Orthogonal Decomposition

Another fundamental tool in the development of this thesis is the use of the Proper Orthogonal Decomposition (POD), or Karhunen-Loeve (KL), or Empirical Orthogonal Functions (EOF), just to give some of the names, technique. In a few words, the POD is a linear data analysis technique which separates a given data set into orthogonal spatial and temporal modes. That is, it provides a basis for a modal decomposition, similar to the Fourier basis, but with some striking features.

Suppose that we have an ensemble $\{u^k\}$ of complex scalar fields, each being a function $u = u(x) \in L^2(\Omega)$, $\Omega \subseteq R$ (in particular, in our calculations the ensemble of functions is given by different snapshots of the time evolution of a spatiotemporal field, that is, $\{u^k\} = u(x, t_k)$. The idea behind the POD is straighforward: we want to find a functional basis $\{\phi_j(x)\}_{j=1}^{\infty}$ that is optimal for the data set in the sense that finite-dimensional representations of the form

$$u_N(x) = \sum_{j=1}^{N} a_j \phi_j(x) \tag{1.13}$$

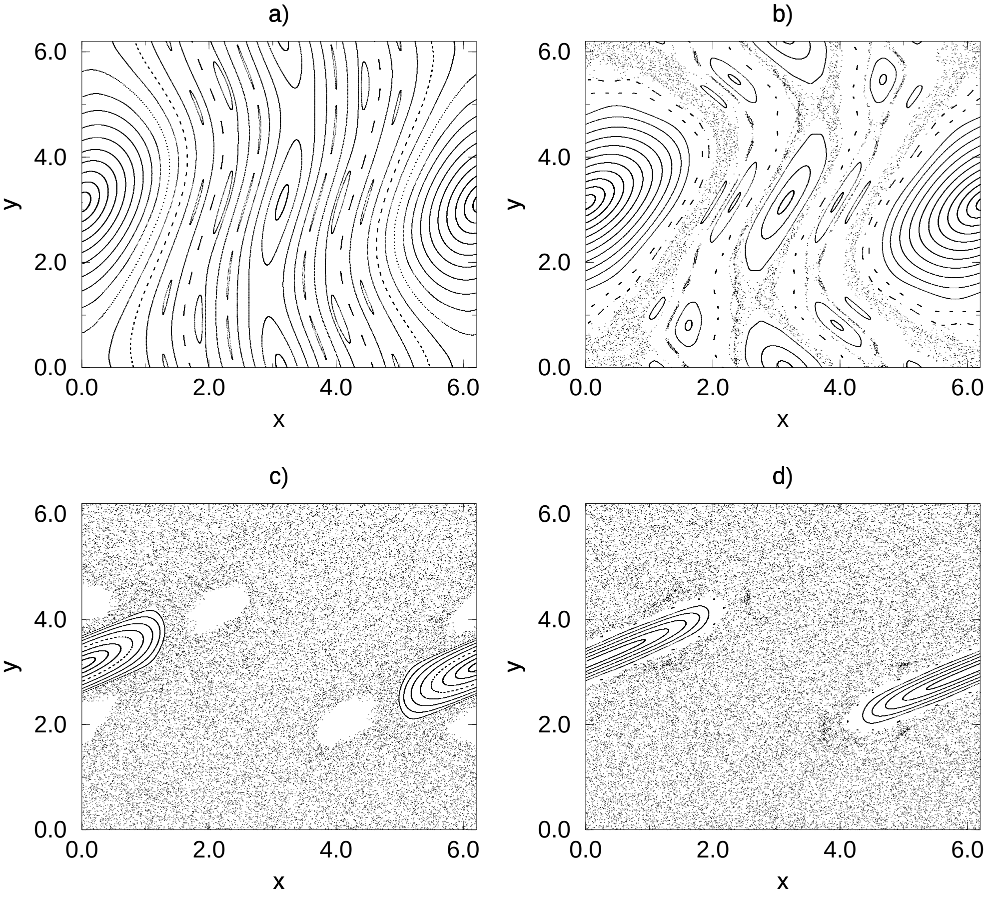

Figure 1.1: Plots of trajectories obtained iterating the standard map (1.11,1.12) for four values of K; a) $K = 0.5$; b) $K = 1.0$; c) $K = 2.5$; d) $K = 4.0$.

describe typical members of the ensemble better than representations of the same dimension N in any other basis.

Therefore, the mathematical statement of optimality is that we should find a $\phi(x) \in L^2(\Omega)$, suitably normalised, that has the maximum averaged projection onto u, i.e.:

$$max_{\Phi(x)\in L^2(\Omega)} \frac{< |(u,\Phi)|^2 >}{|(\Phi,\Phi)|} = \frac{< |(u,\phi)|^2 >}{|(\phi,\phi)|}, \tag{1.14}$$

where $< \cdot >$ is the ensemble average (temporal average in our applications), and $(u, \Phi) = \int_\Omega u(x)\Phi^*(x)dx$ is the usual scalar product in $L^2(\Omega)$ (note that other different functional spaces with different scalar products could be used in this optimization problem, and given rise to another POD basis). A different, but equivalent, way to read the optimization problem (1.14) is that we are interested in finding a structure ϕ which has the largest possible correlation with $u(x)$.

In this way, the problem is one of the calculus of variations: to extremise $< |(u, \phi)|^2 >$ subject to the constraint $|(\phi, \phi)| = 1$. It is easily shown [10] that the problem finally reduces to find the largest eigenvalue of the following integral equation:

$$\int R(x,x')\phi(x')dx' = \lambda\phi(x), \tag{1.15}$$

where $R(x,x') =< u(x)u^*(x') >$.

Moreover, Hilbert-Schmidt theory assures that there is a countable infinity of eigenvalues and eigenfunctions that provides a diagonal decomposition of the averaged autocorrelation function:

$$R(x,x') = \sum_{j=1}^{\infty} \lambda_j \phi_j(x)\phi_j^*(x'), \tag{1.16}$$

and that the eigenfunctions ϕ_j are mutually orthogonal. They are the empirical orthogonal functions. Thus, the optimal basis is given by the eigenfunctions $\{\phi_j\}$ of the integral equation (1.15) whose kernel is the averaged autocorrelation function $R(x,x')$.

Also, almost every member of the ensemble $\{u^k\}$ used in the averaging $< \cdot >$ leading to $R(x,x')$ can be reproduced by a modal decomposition based on the eigenfunctions $\{\phi_j\}_{j=1}^{\infty}$:

$$u(x) = \sum_{j=1}^{\infty} a_j \phi_j(x), \tag{1.17}$$

where the $\{a_j\}_{j=1}^{\infty}$ are random variables satisfying:

$$< a_k a_m^* >= \lambda_k \delta_{km}. \tag{1.18}$$

The eigenvalues λ_k are all positive and are ordered in such a way that the convergence of the representation (1.17) is optimized. The mean square of a_1 is as large as posible, the one of a_2 is the second largest, and so on. We remark that, *among all linear decompositions with respect to an arbitrary basis $\{\Phi_i(x,y)\}$, for a truncation or order N, i.e., $u^N(x,y,t) = \sum_{i=1}^{N} a_i(t)\Phi_i(x,y)$, with $a_i(t) = \int_A u(x,y,t)\Phi_i(x,y)$, the minimum error, defining the error as $\epsilon = \left\langle \int_A (u-u^N)^2 dxdy \right\rangle$, is obtained when $\{Phi_i(x,y)\}$ is the POD basis $\{\phi_i(x,y)\}$.*

Because of the above mentioned characteristics of the POD, the empirical eigenfunctions ϕ_j constitute an optimum basis for a Galerkin approximation to the dynamics, in order to obtain a low dimensional description for this. Suposse that the scalar field is time dependent $u(x,t)$, and obeys an equation of the type

$$\frac{du}{dt} = F(u), \tag{1.19}$$

where $F(\cdot)$ represents a nonlinear operator that may involve spatial derivatives and/or integrals. The optimum Galerkin projection is approached by considering the N-dimensional modal decomposition in terms of the POD basis:

$$u(x,t) = \sum_{j=1}^{N} a_j(t)\phi_j(x), \tag{1.20}$$

where now the coefficients a_j are time dependent. Projecting (1.20) onto (1.19), and using the orthogonality of the basis functions $\{\phi_j\}$, a system of ordinary differential equations (a low dimensional model) is obtained for the coefficients $a_j(t)$:

$$\frac{da_k}{dt} = \left(F\left(\sum_{j=1}^{N} a_j(t)\phi_j(x) \right), \phi_k(x) \right), \quad k = 1, 2, ..., N, \tag{1.21}$$

where $(,)$ is the usual scalar product. We remark that the Galerkin approximation is suitable for any functional basis, like for e.g. the Fourier basis, but the obtained low dimensional model (1.21) is optimum when the POD basis is used in the modal decomposition (1.20).

Just to finish with this brief introduction to the POD technique, let us remark the following points: a) the formulation we have presented is the simplest one, some other POD basis obtained in Sobolev spaces or with a different metric have been studied, for e.g., in [11]. b) Also, the temporal sorting is not used to obtaining the POD basis, i.e., the same basis is obtained for the ensembles $\{u_1\} = \{u(x,t_1), u(x,t_2), ...u(x,t_n)\}$ and $\{u_2\} = \{u(x,t_2), u(x,t_1), ...u(x,t_n)\}$. A POD formulation where information about the temporal sorting is considered can be consulted in [12]. c) The POD is a linear technique: it is just an eigenvalue problem (1.15). Therefore, the POD is, among *all linear decompositions*, the most efficient for reconstructing a signal $u(x,t)$ (once the vectorial space with its metric has been fixed). Nonlinear techniques similar to the POD are unknown to the author, but a very complete review of the POD with extensions and comparisons with other analysis techniques can be consulted in [10, 13].

1.1.4 Genetic Algorithms

To finish of filling up our toolbox of methods, we proceed to introduce the prediction technique of the Genetic Algorithms (GA). These are a kind of evolutionary computational methods, i.e. optimization methods in which the optimal solution is searched through steps inspired in the natural evolution: *selection and survival of the fittest*. Usually the optimization target is a mathematical procedure of known form, but with many undetermined parameters. A population of candidate procedures is generated by expressing different sets of these parameters as binary strings. The perfomance of each procedure is evaluated and those that are *fitter* or do better according to some specific criteria are allowed to reproduce. Reproduction may be sexual, by taking the strings of two fit parent procedures and generating the binary string for the descendant by using cross-over and perhaps mutation, or it may be asexual, in which case just mutation is used. Over many generations, the population tends towards more successful procedures.

A very nice example of the use of the GA's has appeared recently in [14], where automatic design and manufacture of robots is carried out. This can give us an idea of the power and versatility of this technique. In particular, we will use the GA's as predictors for time series. Thus, given a time series $(x_1, x_2, ..., x_T)$, GA's look for a mathematical law relating any variable with some of the past: $x_t = f(x_{t-1}, x_{t-2}, ..., x_{t-L})$. The first step is to choose a subset of the time series, the so-called *training set* $\{x_{L+1}, ..., x_T\}$, where the algorithm will be working on to find an expression like this. Then the algorithm proceed as follows:

- i) **Initialization**. N different expressions f built up from random combinations of real numbers, some of the x_t, and the four basic arithmetic operators, $+, -, \times, and\ \div$, are generated.

- ii) **Fitting and surviving**. For each of these expressions, estimates of x_t in the training set are computed and compared (using the variance, for e.g.) with x_t of the real data. Then, the half of these expressions with best fitting survive and the rest disappear.
- iii) **Reproduction**. The survivors in the former step form mates and reproduce, generating new expressions by interchanging some chains of operators, real numbers and x_t. This is done in such a way that the fitting is improved in any new generation.
- iv) **Mutation**. Some of the parts of the new expressions can be randomly mutated.
- v) **Evolution**. This process is repeated iteratively until an optimum fitting expression is obtained.

Another important part of the algorithm is the encoding of the form of the equation strings into a numerical structure that allows an easier and faster computational handling. This encoding is accomplished through coordinate pairs in the following way: a pair $(k, 1)$ represents an operator in the equation string. The values of k range from 1 to 4 to represent addition, subtraction, multiplication or division, respectively. Pairs of the form $(a, 2)$ with a being a real number distributed in $[-S_1, S_2]$ (S_1, S_2 parameters) represent real arguments of the equation while pairs $(j, 3)$ with j integer verifying $1 \leq j \leq L$ indicate the arguments given by the element $x(t-j)$ in the time series.

In addition, it is used in the algorithm the *postfix* notation, which refers to the notation in which the operator symbol is placed after its two operands. For example, the postfix expression $AB+$ corresponds to the standard notation $A + B$. An example of encoded string in the algorithm is $P = \{(10.1, 2), (3, 3), (1, 1), (2, 3), (3, 1)\}$ that corresponds to $(10.1 + x(t-3))x(t-2)$.

Now and before proceeding to detail the different Chapters of this work, I (please note that it is not written 'we') would like to remark that, though a better knowledge of ocean dynamics has been my principal aim, the *spirit* guiding my almost four years work has been to contribute to the general understanding of the so-called *complex systems*, that is, spatiotemporal disordered systems. I *believe* in the claim by Goldenfeld and Kadanoff [15] that apparently there are no general laws for complexity, and in this sense, the *classical* approach of Physics of looking for simple but general laws seems not to work, at least nowadays, when we manage with complex systems, that is, with the real world. Nonetheless, one must reach for experience and *lessons* that might be learned in one and applied to another. I would like to think that with this thesis I could modestly contribute to this hope.

1.2 Outline of the Thesis

Next, let us outline the contents of this thesis. There are two main different parts: the first one comprises Chapters 2, 3, 4 and 5. This part concerns with the study of spatial structures of active (in the sense defined above) substances, advected by a two dimensional chaotic flow. The second part, formed by Chapters 6, 7 and 8, is dedicated to obtaining low dimensional descriptions of long (real or numerical) data sets and making predictions.

In the following, we give a deeper introduction to the different Chapters of this memory; but first of all, we should say that every Chapter is selfcontained and could be read independently. This fact has given rise to some repetitions and, sometimes, surplus of information, mainly in the introductory sections to every Chapter, which we think (and hope) that do not break the fluent reading of the Thesis.

So, in the second Chapter, entitled *Smooth-filamental transition of active tracer fields stirred by chaotic advection* we study the spatial structure of an active field advected by a chaotic flow. The fundamental restriction is the assumption that the intrinsic dynamics of the field, that is, its chemical or biological dynamics is characterized by a negative Lyapunov exponent. Then, in the limit of small diffusivity, the full dynamics can be divided in its two subsystems, that is, advection plus reaction. Each of these has its own Lyapunov exponent, negative the one of the reaction part, and positive the one of the flow (a chaotic flow is assumed). The main result of this first Chapter is that depending on the relative strength of both exponents, the spatial structure can be *a) smooth*, if the stability of the reaction part overcomes the stirring due to the chaotic flow, and *b) fractal*, in the opposite case. In addition, an expression relating the Hölder exponent of the filamental structure with the Lyapunov exponents of the system is presented. It is important to note that all along this Chapter a monofractal (as opposed to the multifractal studies in Chapter 3) description is assumed. In other words, a spatially uniform Lyapunov exponent for the flow is considered. Also, we perform numerical simulations supporting these theoretical results.

In Chapter 3, *The multifractal structure of chaotically advected chemical fields*, we try to get a deeper insight into the spatial structures previously studied in Chapter 2. We also consider a 2d chaotic flow stirring a chemically stable (Lyapunov negative) substance, but now we particularize to a decaying chemical dynamics. We perform more carefully the analytical calculations of the former Chapter and we generalize the results when open flows are also considered. These are characterized by unbounded trajectories of fluid particles. On the contrary, closed flows, the ones used in the numerical simulations of the second Chapter, have all the trajectories of the fluid particles bounded. Moreover, we focuss in the multifractal character of the spatial patterns of the active substance, i.e., in the spatial dependence of the Hölder exponent of the chemical field. We study how this dependence affects the scaling exponents of the structure functions, and relate these to the distribution of local Lyapunov exponents of the chaotic flow.

Next in Chapter 4, *Chaotic advection of reacting substances: Plankton dynamics on a meandering jet*, the results of the former Chapters are applied to a more oriented oceanic problem. We use as flow a mathematical model for a meandering jet. That is, a flow of fluid in a direction and showing meanders in the perpendicular one. In addition, the reacting dynamics is that of a plankton model. Specifically, we consider a model with three trophic levels including nutrients (of chemical origin), phytoplankton and zooplankton.

Chapter 5, *Population dynamics advected by chaotic flows: a discrete-time map approach*, is a first tentative to describe the dynamics of reacting substances advected by chaotic flows in terms of discrete-in-time maps. This allows a more accurate numerical treatment of the problem. In particular, we study how a localized distribution of preys or nutrients may affect the spatial structure of the predators. This is carried out by considering the analogies of the advection plus reaction system with a random map. In addition, some attempts to study the case of positive chemical Lyapunov exponet are presented.

In the sixth Chapter, *Low dimensional dynamical system for an oceanic eddy observed in satellite data*, we try to study the dynamics of coherent structures present in real data, in particular, in altimetry data of the oceanic surface. We analyse satellite data of the Western Mediterranean basin with the Proper Orthogonal Decomposition, which allows to identify a moving eddy in the data. Then, the POD is used to obtain a low dimensional approximation to the full dynamics of this eddy. This is done by projecting the POD modes over a hydrodynamical model of the oceanic region under study. Finally, nonlinear dynamics tools are used to study this low dimensional model.

In Chapter 7, entitled *Forecasting confined spatiotemporal chaos with genetic algorithms*, we present a new technique for predicting spatiotemporal series of data. The technique consists in the successive application of the POD and genetic algorithms (GA). With the POD we reduce the full spatiotemporal dynamics to a small number of time series. After this, and differently to the former Chapter where a physical model of the system was assumed, we make predictions of these time series by applying a genetic algorithm to each of these time series. We check this method with data obtained from a numerical simulation of a mathematical model displaying spatiotemporal chaos, the *Complex Ginzburg-Landau equation*.

In Chapter 8, *Forecasting the sea surface temperature space-time variability of the Alboran Sea with genetic algorithms*, we apply the technique developed in the former Chapter to real satellite data of the sea surface. These correspond to monthly averaged data of the sea surface temperature of the Alboran Sea, an area of the Mediterranean Sea. The only modification with respect to the method applied to numerical data of Chapter 7, is a kind of cleaning of the data again with a POD of every obtained time series.

Finally, in Chapter 9 we present a summary of the Thesis.

The contents of this thesis correspond to the following articles:

- 1) Z. Neufeld, C. López and P.H. Haynes, Physical Review Letters **82**, 2602 (1999).
- 2) Z. Neufeld, C. López, E. Hernández-García and T. Tél, Physical Review E **61**, 3857 (2000).
- 3) C. López, Z. Neufeld, E. Hernández-García and P.H. Haynes, Physics and Chemistry of the Earth, in press (2000).
- 4) E. Hernández-García, C. López, O. Piro, A. Vulpiani and E. Zambianchi, CHAOS, submitted (2000).
- 5) C. López and E. Hernández-García, Physica D, submitted (2000).
- 6) C. López, A. Álvarez and E. Hernández-García, Physical Review Letters **85**, 2300 (2000).
- 7) A. Álvarez, C. López, M. Riera, E. Hernández-García and J. Tintoré, Geophysical Research Letters **27**, 2709 (2000).

Chapter 2

Smooth-filamental transition of active tracer fields stirred by chaotic advection

The spatial distribution of interacting chemical fields is investigated in the non-diffusive limit. The evolution of fluid parcels is described by independent dynamical systems driven by chaotic advection. The distribution can be filamental or smooth depending on the relative strength of the dispersion due to chaotic advection and the stability of the chemical dynamics. We give the condition for the smooth-filamental transition and relate the Hölder exponent of the filamental structure to the Lyapunov exponents. Theoretical findings are illustrated by numerical experiments.

2.1 Introduction

The Lagrangian description of fluid flows, considered in the framework of chaotic dynamical systems, has given important insight into mixing and transport [6]. In many situations of practical interest scalar fields describing some property of the fluid are not just simply advected by the flow, but are *active* in the sense that they have their own dynamics, in general coupled to the transport and mixing process. (In the following we will refer to this as the 'chemical' dynamics of the system.) Typical examples of active fields in mixing flows are concentrations of reacting chemicals [16, 17] (in industrial processes or the atmosphere) and interacting biological populations of microorganisms in a fluid (e.g. plankton populations stirred by oceanic currents [18]). The spatial structure of such fields often has complex filamental character [19]. Previous work has investigated the temporal evolution of reactions such as $A + B \to C$ or $A + B \to 2B$ in closed flows [17, 20, 21] as an initial value problem. The absence of chemical sources in these cases necessarily implies a homogeneous final state of the system. The same reactions were also studied in open chaotic flows [22] where a stationary fractal distribution arises due to the properties of the underlying (chaotic scattering-like) advection dynamics [23]. Here we show that in the case of stable chemical dynamics (in a sense defined below) and in the presence of chemical sources persistent filamental fractal patterns can also arise in closed flows.

2.2 Eulerian and Lagrangian description of the problem.

The governing equations for a set of N interacting 'chemical' fields C_i mixed by a incompressible flow $\mathbf{v}(\mathbf{r}, t)$, independent of the chemical dynamics, can be written as

$$\frac{\partial C_i}{\partial t} + \mathbf{v}(\mathbf{r}, t) \cdot \nabla C_i = \mathcal{F}_i[C_1(\mathbf{r}), .., C_N(\mathbf{r}), \mathbf{r}], \tag{2.1}$$

where $i = 1, .., N$. The operators $\mathcal{F}_i$ in general contain spatial derivatives of the fields C_i, e.g. a Laplacian term representing diffusion.

Let us assume that the advective transport dominates and diffusion is weak. If we neglect non-local processes like diffusion on the right hand side of (2.1) F_i becomes a simple function of the local concentrations and coordinates. In this case the Lagrangian representation leads to a considerable simplification of the equations, leading to a low-dimensional dynamical system

$$\frac{d\mathbf{r}}{dt} = \mathbf{v}(\mathbf{r}, t), \quad \frac{dC_i}{dt} = F_i(C_1, C_2, .., C_N, \mathbf{r}), \; i = 1, ., N, \tag{2.2}$$

where the second set of equations describes the chemical dynamics inside a fluid parcel that is advected by the flow according to the first equation. The coupling between the flow and chemical evolution is non-trivial if some of the functions F_i depend explicitly on the coordinate $\mathbf{r}$. In applications this dependence of F_i can appear as a consequence of spatially varying sources, spatially varying (e.g. temperature dependent) reaction rates or reproduction rates of biological species. It is therefore natural to include this dependence in the model to be considered.

Although we use a Lagrangian representation, our aim is to follow not the chemical evolution along individual trajectories, but the spatiotemporal dynamics of the chemical fields $C_i(\mathbf{r},t)$ that is equivalent to the evolution of the ensemble of fluid parcels under the dynamics (2.2). Thus the original problem defined in an infinite dimensional phase space is reduced to an ensemble problem in a low-dimensional dynamical system.

By neglecting diffusion, we may miss certain classes of behaviour such as propagating waves, typical for reaction-diffusion systems [24]. However, as we shall see later, we capture a non-trivial behaviour that we believe to be characteristic of the full advection-reaction-diffusion problem when diffusion is weak.

We assume that the flow $\mathbf{v}(\mathbf{r},t)$ is two-dimensional incompressible and periodic in time with period T. These conditions in general lead to chaotic advection even in case of simple spatially smooth (non-turbulent) velocity fields. Since the advection is independent of the chemical dynamics it can be characterised by its own Lyapunov exponents $\lambda_1^F > \lambda_2^F$. Incompressibility implies that the advection is described by a conservative dynamical system and thus $\lambda_1^F = -\lambda_2^F$.

For numerical investigations we used a simple time-periodic flow that consists of the alternation of two steady sinusoidal shear flows in the x and y direction for the first and the second half of the period, respectively. The flow is defined on the unit square with periodic boundary conditions by the velocity field

$$\begin{aligned} v_x(x,y,t) &= -\frac{U}{T}\Theta\Big(\frac{T}{2} - t \bmod T\Big)\cos(2\pi y) \\ v_y(x,y,t) &= -\frac{U}{T}\Theta\Big(t \bmod T - \frac{T}{2}\Big)\cos(2\pi x) \end{aligned} \tag{2.3}$$

where $\Theta(x)$ is the Heavyside step function. $U \to 0$ corresponds to an integrable limit of the advection problem. We will consider the case $U = 1.0$ producing a flow that consists of one connected chaotic region. The parameter T controls the relative time-scale of the flow and reactions. By changing T we can vary the Lyapunov exponents of the flow without altering the shape of the trajectories and the spatial structure of the flow.

Since the trajectories $\mathbf{r}(t)$ are chaotic the chemical dynamics (2.2) correspond to a chaotically driven dynamical system. This subsystem can be characterised by the set of chemical Lyapunov exponents $\lambda_1^C > \lambda_2^C > ... > \lambda_N^C$, that depend on the driving by the chaotic advection. Here we will only consider the simplest situation, when the largest chemical Lyapunov exponent is negative and, for a fixed trajectory $\mathbf{r}(t)$, the chemical evolutions converge to the same globally attracting chaotic orbit for any initial condition in the chemical subspace. In the case of no explicit space dependence in the functions F_i (i.e. no driving) this would correspond to a globally attracting fixed point of the chemical subsystem.

A simple example of such a system (relevant for atmospheric photochemistry) is the decay of a chemical species ($N = 1$) produced by a non-homogeneous source, with chemical dynamics

$$\dot{C} = a(\mathbf{r}) - bC, \tag{2.4}$$

for which $\lambda^C = -b$ independently of the driving.

2.3 Spatial structure of the chemical fields: smooth and filamental patterns.

First we investigate the temporal evolution of the chemical fields. Although the Lagrangian variables $C_i(t)$ have a chaotic time-dependence according to the positivity of the largest Lyapunov exponent for the full dynamical system (2.2), it can be shown that the Eulerian chemical field $C_i(\mathbf{r},t)$ is asymptotically periodic in time with the period of the flow. In order to obtain the values of the fields at point $\mathbf{r}$ at time t one can $i)$ integrate the advection backward in time and use the obtained trajectory $\mathbf{r}(t')$ ($0 < t' < t$) and the initial values of the chemical fields at the point $\mathbf{r}(0)$ to $ii)$ integrate the chemical dynamics forward in time from 0 to t. The value of the field at the same point at time $t+nT$ can be obtained similarly. The resulting backward trajectory will be the same (due to the periodicity of the flow) but longer. By integrating the chemical evolution forward in time for nT we obtain a problem equivalent to the previous one with a different set of initial concentrations, that according to the assumptions made above ($\lambda_1^C < 0$) converge to the same orbit. Consequently the chemical fields are asymptotically periodic in time

$$\lim_{m\to\infty} C_i(\mathbf{r},(m+n)T+\tau) = \lim_{m\to\infty} C_i(\mathbf{r},mT+\tau), \tag{2.5}$$

where $\tau = t \bmod T$, defining an asymptotic chemical field $C^\infty(\mathbf{r},\tau)$.

In the following we investigate the spatial structure of the chemical fields. For this we calculate the difference

$$\delta C_i = C_i(\mathbf{r}+\delta\mathbf{r},t) - C_i(\mathbf{r},t), \qquad |\delta\mathbf{r}| \ll 1, \tag{2.6}$$

that can be obtained by integrating (2.2) along two trajectories ending at the preselected points $\mathbf{r}$ and $\mathbf{r}+\delta\mathbf{r}$ at time t. The time evolution of the distance $|\delta\mathbf{r}(t')|$ (for $t-t' \gg 1$) can be estimated from the time reversed advection dynamics as

$$|\delta\mathbf{r}(t')| \sim |\delta\mathbf{r}(t)|e^{\lambda^F(t-t')} \tag{2.7}$$

where $\lambda^F = \lambda_1^F > 0$ for almost all final orientations $\mathbf{n}(t) \equiv \delta\mathbf{r}(t)/|\delta\mathbf{r}(t)|$. The only exception is the unstable contracting direction of the time reversed flow corresponding to $\lambda^F = \lambda_2^F < 0$.

By expanding (2.2) around the chaotic orbit $C_i(\mathbf{r}(t))$ we obtain a set of linear equations

$$\delta\dot{C}_i = \sum_{j=1}^{N} \frac{\partial F_i}{\partial C_j}\delta C_j + \nabla_r F_i \cdot \delta\mathbf{r} \tag{2.8}$$

with initial condition

$$\delta C_i(0) = C_i^0(\mathbf{r}(0)+\delta\mathbf{r}(0)) - C_i^0(\mathbf{r}(0)), \tag{2.9}$$

where $C_i^0(\mathbf{r})$ are the initial chemical fields.

In the simplest case $N=1$ the solution of (2.8) can be written explicitly as

$$\delta C(t) = \nabla_r C^0 \cdot \delta\mathbf{r}(0)e^{\lambda t} + \int_0^t \nabla_r F \cdot \delta\mathbf{r}(t')e^{\lambda(t-t')}dt' \tag{2.10}$$

where

$$\lambda = \frac{1}{t}\int_0^t \frac{\partial F}{\partial C}(C(\mathbf{r}(t')), \mathbf{r}(t'))dt' \tag{2.11}$$

that becomes equal to the chemical Lyapunov exponent λ^C in the $t \to \infty$ limit. The first term in (2.10) represents a deviation due to non-homogeneous initial conditions and the second one describes the effect of different histories of the two trajectories appearing via the space dependence of F.

Using (2.7) we obtain from (2.10) for the projection of the gradient of C to a direction $\mathbf{n}$

$$\begin{aligned} \frac{\delta C(t)}{|\delta\mathbf{r}(t)|} &= \nabla C^0 \mathbf{n}(0) e^{(\lambda^F+\lambda^C)t} + \\ &+ \int_0^t \nabla F(\mathbf{r}(t'))\mathbf{n}(t') e^{(\lambda^F+\lambda^C)(t-t')} dt'. \end{aligned} \tag{2.12}$$

The convergence of the right hand side of the above equation for $t \to \infty$ depends on the sign of the exponent $\lambda^F + \lambda^C$. If $\lambda^F < |\lambda^C|$ the convergence of the chemical dynamics is stronger than the dispersion of the trajectories in the physical space and results in a smooth field $C^\infty(\mathbf{r}, \tau)$. On the contrary, if $\lambda^F > |\lambda^C|$ the memory of the chemical dynamics decays too slowly to forget the different spatial histories (or initial conditions). In this case the limit does not exist and the field $C^\infty(\mathbf{r}, \tau)$ has an irregular structure that is almost nowhere differentiable. There exists, however, at each point one special direction in which the derivative is finite. This direction is the contracting direction in the time-reversed advection dynamics corresponding to the negative Lyapunov exponent of the flow λ_2^F. Thus we suggest a precise definition of a *filamental* structure, being a non-differentiable field, that is still smooth in one direction at each point (with that direction itself varying smoothly).

The irregular chemical field can be characterised by its Hölder exponent α defined as $\delta C(\delta\mathbf{r}) \sim |\delta\mathbf{r}|^\alpha$, where $0 < \alpha < 1$ and $\alpha = 1$ for a differentiable function. In our case if $\lambda^F + \lambda^C > 0$

$$\delta C(t) \sim |\delta\mathbf{r}(t)| e^{(\lambda^F+\lambda^C)t}. \tag{2.13}$$

Expressing time from (2.7) as

$$t = \frac{1}{\lambda^F} \ln \frac{|\delta\mathbf{r}(0)|}{|\delta\mathbf{r}(t)|} \tag{2.14}$$

and inserting it in (2.13) we obtain

$$\delta C(t) \sim |\delta\mathbf{r}(0)|^{(1+\lambda^C/\lambda^F)} |\delta\mathbf{r}(t)|^{-\lambda^C/\lambda^F}. \tag{2.15}$$

For very long times and in a closed flow $|\delta\mathbf{r}(0)|$ will saturate at a finite value in the backward advection dynamics. Thus the Hölder exponent is $\alpha = |\lambda^C|/\lambda^F$. Certainly, diffusion would smooth out the small scale filamental structures below a certain diffusive scale (approaching zero for smaller and smaller diffusivities), setting a cut-off for the scaling relation (2.15). Nevertheless, above the diffusive scale filamental structures will persist for arbitrarily long time since, in the presence of chemical sources, the effect of diffusion is balanced by the continuous generation of small scale structures by the chaotic advection.

As an example we consider the system (2.4), which is the simplest possible system that exhibits the smooth-filamental transition, using a source term of the form $a(x, y) =$

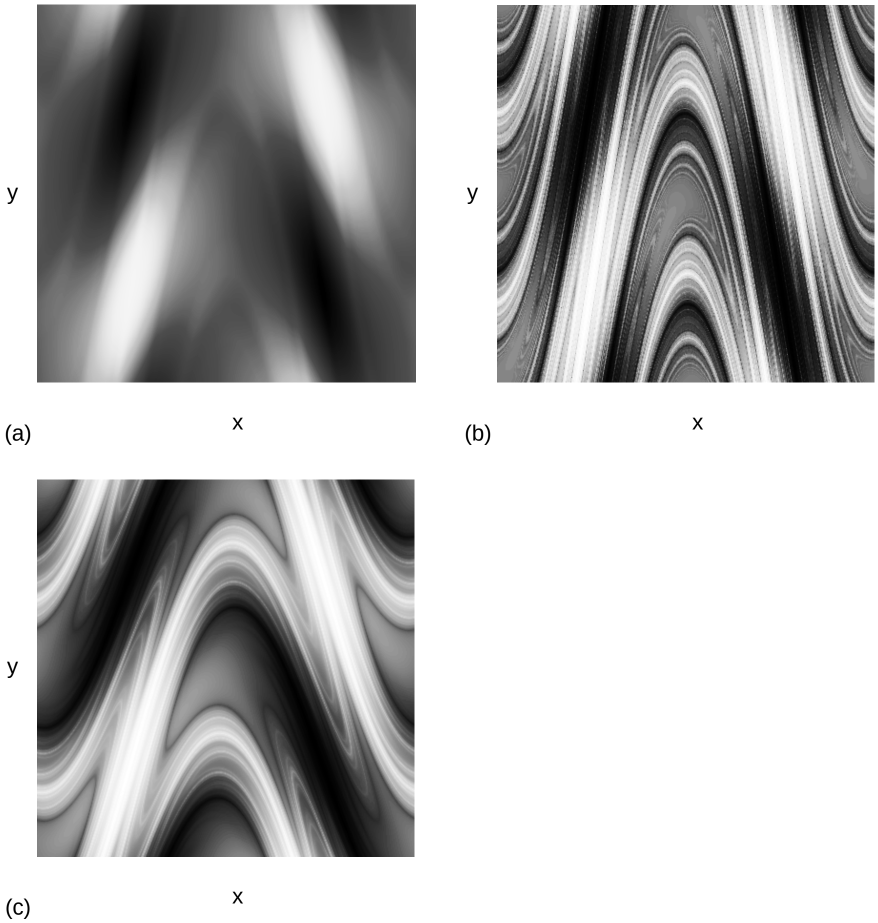

Figure 2.1: Smooth (a) and filamental (b) distributions of the decaying substance (eq.2.4) mixed by the flow (eq. 2.3) after 20 periods using $a_1 = 0.1$,$b = 1.0$,$U = 1.0$ and initial condition $C(\mathbf{r}, t = 0) = 0.0$. The integration has been done for 200×200 points with final positions on a rectangular grid. For $U = 1.0$ the numerically calculated Lyapunov exponent of the flow is $\lambda^F \approx 2.35/T$. The period of the flow is $T = 5.0$ ($\lambda^F < b$) in (a) and $T = 1.0$ ($\lambda^F > b$) in (b), respectively. (c) coexistence of smooth and filamental structures for $U = 0.5$ and $T = 1.0$.

$1+a_1 \sin(2\pi x) \sin(2\pi y)$. Numerically calculated chemical fields (obtained by a backward integration of the advection problem and forward integration of the chemical dynamics [25]) of both types are shown in Fig.1a and b. Figure 2 shows a section of the smooth and filamental fields of Fig.1 along the line $y = 0.25$. We also measured the box counting fractal dimension of the function $C(\mathbf{r})$ along a cut in the x direction, which is related to the Hölder exponent by $D = 2 - \alpha$ [26]. Numerically computed values agree well with the theoretical prediction as shown in Fig. 3. If the flow does not consist of only one connected chaotic region, but is composed by chaotic regions separated by KAM tori, the Lyapunov exponents of the flow are different in each chaotic region and the structure of the chemical field can be smooth in certain regions but filamentary in others (Fig 1c.).

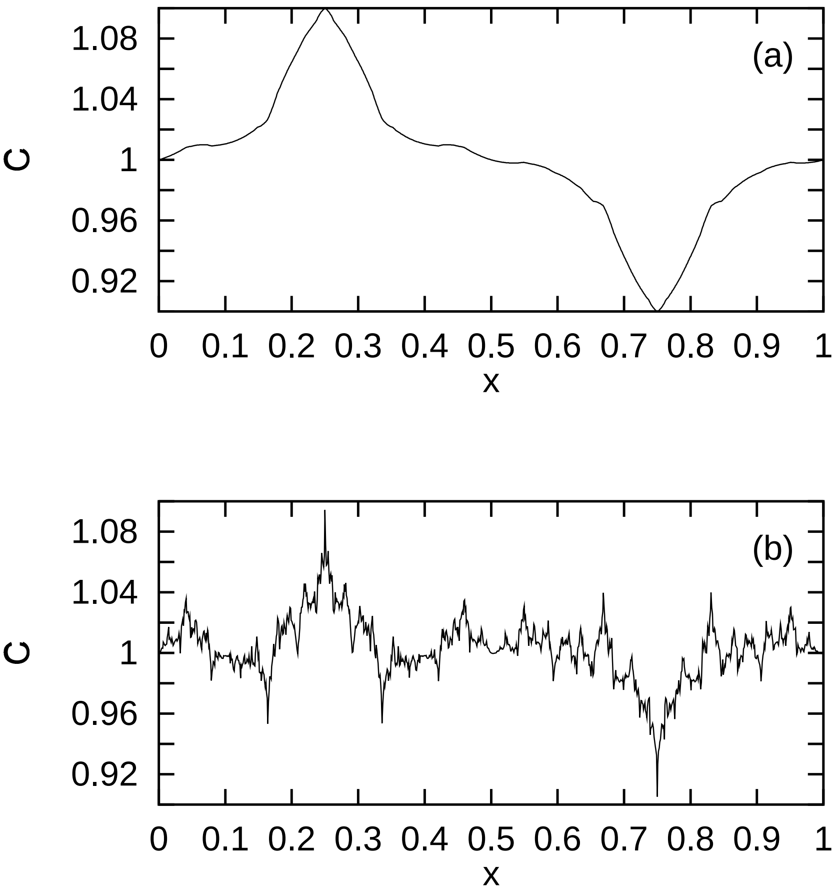

Figure 2.2: Sections of the smooth (a) and filamental (b) fields shown in Fig.1 along the line $y = 0.25$.

In the more general case $N > 1$ the same smooth-filamental transition can be obtained. Let us once again consider at a particular time t the difference $\delta C_i(t)$ in the chemical fields over a small preselected displacement $\delta\mathbf{r}$. The time dependence of a set of initial deviations $\delta C_i(0)$ and $\delta\mathbf{r}(0)$, for the dynamical system (2.2) has the asymptotic form

$$\Big(\sum_{i=1}^{N} \delta C_i^2(t) + \delta\mathbf{r}^2(t)\Big)^{1/2} \sim \Big(\sum_{i=1}^{N} \delta C_i^2(0) + \delta\mathbf{r}^2(0)\Big)^{1/2} e^{\lambda t} \tag{2.16}$$

where λ is one of the Lyapunov exponents of the system. For a typical choice of the final deviation $\delta\mathbf{r}(t)$, $\delta\mathbf{r}$ will be divergent in the time reversed dynamics, and consequently contracting in the forward direction. Thus, the contribution of $\delta\mathbf{r}$ decays in the left hand side of (2.16) and λ cannot be the positive Lyapunov exponent λ_1^F so the typical value of λ will be the second largest Lyapunov exponent. There are thus two possibilities $\lambda = \lambda_2^F = -\lambda_1^F$ (if $\lambda_2^F > \lambda_1^C$) or $\lambda = \lambda_1^C$ (otherwise). We can now divide both sides of (2.16) by $\delta\mathbf{r}(t)$ using (2.7)

$$\Big(\sum_{i=1}^{N} \frac{\delta C_i^2(t)}{\delta\mathbf{r}^2(t)} + 1\Big)^{1/2} \sim \Big(\sum_{i=1}^{N} \frac{\delta C_i^2(0)}{\delta\mathbf{r}^2(0)} + 1\Big)^{1/2} e^{(\lambda_1^F + \lambda)t}. \tag{2.17}$$

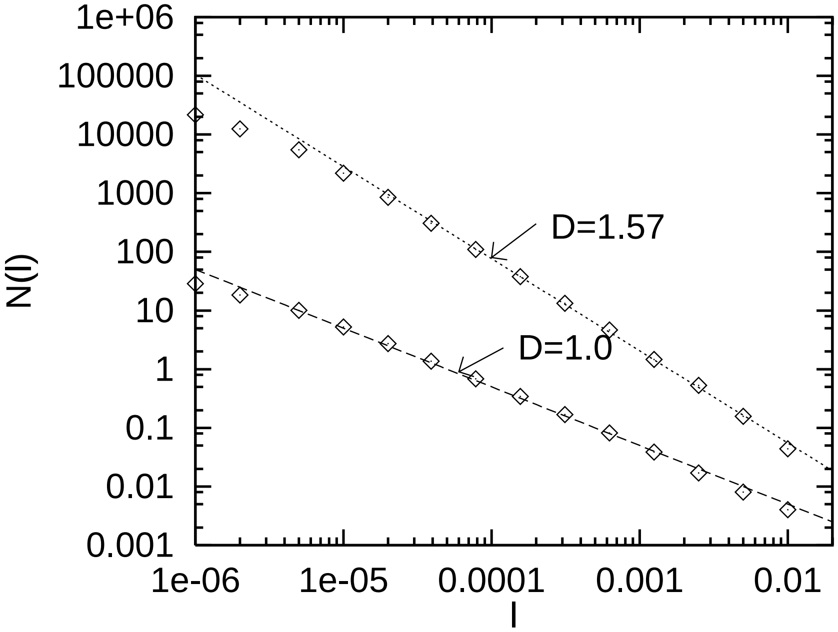

Figure 2.3: Box counting fractal dimensions of the functions $C(x)$ shown in Fig.2. Number of boxes needed to cover the graph of the function $C(x)$ vs. the box size l (squares) and slopes corresponding to the relation $D = 2 - b/\lambda^F$.

Thus, the chemical fields $C_i(\mathbf{r})$ become non-differentiable in the $t \to \infty$ limit if $\lambda_1^F > |\lambda_1^C|$.

2.4 Summary

Just to summarize and very briefly, we have studied the spatial distribution of active tracer fields, such as plankton populations or reacting chemicals, stirred by chaotic advection. This has been done in the non-diffusive limit which has allowed us to debscribe the advection-reaction-diffusion system as a set of independent dynamical systems. Depending on the relative strength of the flow and the chemical dynamics the spatial distribution of the tracers can be smooth or filamental. Also, in the case of the filamental pattern, we have related the Hölder exponent (or the fractal dimension) of this with the dynamical magnitudes of the system, i.e., the Lyapunov exponents of the flow dynamics and the one of the chemical dynamics. It is important to note that all along this Chapter a spatially uniform chemical Lyapunov exponent has been considered. The case of spatial dependence is treated in the next Chapter.

Chapter 3

The multifractal structure of chaotically advected chemical fields

The structure of the concentration field of a decaying substance produced by chemical sources and advected by a smooth incompressible two-dimensional flow is investigated. We focus our attention on the non-uniformities of the Hölder exponent of the resulting filamental chemical field. They appear most evidently in the case of open flows where irregularities of the field exhibit strong spatial intermittency as they are restricted to a fractal manifold. Non-uniformities of the Hölder exponent of the chemical field in closed flows appears as a consequence of the non-uniform stretching of the fluid elements. We study how this affects the scaling exponents of the structure functions, displaying anomalous scaling, and relate the scaling exponents to the distribution of local Lyapunov exponents of the advection dynamics. Theoretical predictions are compared with numerical experiments.

3.1 Introduction

Mixing in fluids plays an important role in nature and technology with implications in areas ranging from geophysics to chemical engineering [6]. The phenomenon of chaotic advection – intensively investigated during the last decade – provides a basic mechanism for mixing in laminar flows [5]. Briefly stated, chaotic advection refers to the situation in which fluid elements in a non-turbulent flow follow chaotic trajectories. Advection by simple time-dependent two-dimensional flows falls generically under this category. Stirring by chaotic motion, with its characteristic stretching and folding of material elements, is able to bring distant parts of the fluid into intimate contact and thus greatly enhances mixing by molecular diffusion acting at small scales.

Mixing efficiency becomes specially important when the substances advected by the flow are not inert but have some kind of activity. By 'activity' we mean that some time-evolution is occurring to the concentrations inside advected fluid elements (produced by chemical reactions, for example). For definiteness we will use terms such as chemical fields and chemical reactions, but biological processes, occurring for example when the advected substance is living plankton, can be described formally in the same way. The interaction between the stirring process and the chemical activity can result in complex patterns for the spatial distribution of the chemical fields, which in turn greatly affect the chemical processes [16, 19]. In addition to the impact on its own chemical dynamics, the spatial inhomogeneities may have important effect on other dynamical processes occurring in the fluid (for example in the behavior of predators seeking for the advected plankton [29]). An understanding of the structure of these spatial patterns is thus valuable.

Previous theoretical work concentrated on the temporal evolution of the total amount of chemical products in specific reactions such as $A + B \to 2B$ [20]. In [22] the same autocatalytic reaction and the collisional rection $A + B \to 2C$ were studied in open flows. In the previous Chapter we considered a class of chemical dynamics characterized by a negative Lyapunov exponent in the presence of (non-homogeneous) chemical sources. Under such chemical processes, reactant concentrations present a tendency to relax towards a local-equilibrium concentration (the fixed point of the local chemical dynamics). This tendency is disrupted by the advection process, which forces fluid elements to visit places with different local-equilibrium states. Depending on the relative strength of chaotic advection and relaxation the resulting concentration distribution can be smooth (differentiable) or exhibits characteristic filamental patterns that are nowhere differentiable except in the direction of filaments aligned with the unstable foliation induced in the fluid by the chaotic dynamics. The mechanism for the appearance of these singular filaments is similar to the one producing singular invariant measures in dynamical systems [31], although here it is affected by the presence of the chemical dynamics: stretching by the flow homogeneizes the pattern along unstable directions, whereas small-scale variance, cascading down from larger scales, accumulates along the stable directions, producing diverging gradients.

The strength of the singularities of the concentration field $C(\mathbf{r})$ can be characterized by a Hölder exponent α

$$|\delta C(\mathbf{r_0}; \delta\mathbf{r})| \equiv |C(\mathbf{r_0} + \delta\mathbf{r}) - C(\mathbf{r_0})| \sim |\delta\mathbf{r}|^{\alpha}, \quad |\delta\mathbf{r}| \to 0 \, . \tag{3.1}$$

If the field is smooth (differentiable) at $\mathbf{r_0}$, $\alpha = 1$, while for an irregular rough (e.g. filamental) structure $0 < \alpha < 1$. In Chapter 2 we focused on the existence of a smooth-filamental transition as time-scales of the system are varied, and also obtained the most probable (bulk) value of the Hölder exponent. Note, however, that the Hölder exponent defined by (3.1) is a local characteristic of the field, whose value may depend on the position $\mathbf{r_0}$. In this Chapter we concentrate on such non-uniformities of the filamental chemical field and study how this affects scaling properties of quantities involving spatial averages, which are the more convenient quantities to be observed in experiments.

In Section 3.2 we review and detail the deductions of the results presented in Chapter 2, namely the smooth-filamental transition and the dominant value of the Hölder exponent in closed flows. Then we consider the same problem for the case of mixing by open flows (Sect. 3.3). In this case the necessity of a multifractal description becomes manifest, and this motivates the development of a quantitative characterization of the filamental structures in terms of structure functions. This is presented in Sect. 3.4. Scaling exponents appear to be related to the distribution of local Lyapunov exponents. We conclude this Chapter with a summary and discussion.

3.2 Local properties of the chemical field and the smooth-filamental transition

We consider the flow as externally prescribed, thus neglecting any back influence of the chemical dynamics into the hydrodynamics (the advected substances are chemically active but hydrodynamically passive). In this context, the general continuum description of chemical reactions in hydrodynamic flows is given by sets of reaction-advection-diffusion equations. They involve in general multiple components and nonlinear reaction terms. In Chapter 2 we considered the situation in which the chemical kinetics is stable, i.e. there is a local-equilibrium state at each spatial position, determined by the sources and the reaction terms, so that concentrations of fluid particles visiting that position tend to relax to the local-equilibrium value. Mathematically this corresponds to the negativity of the Lyapunov exponents associated to the chemical dynamical subsystem. It was shown in the preciding chapter that arbitrary chemical dynamics in this class can be substituted by linear relaxation towards local equilibrium at a rate given by the largest (least negative) chemical Lyapunov exponent. Within this restriction, the multiplicity of components is not essential since, except for special types of coupling, linearization leads to simple relations between the different fields.

Because of the above remarks, and with the aim of keeping the mathematics as simple as possible, we will restrict our considerations in this Chapter to the simplest chemical evolution: linear decay, at a rate b, of a single advected substance. A space-dependent source of the substance will also be included, to maintain a non-trivial concentration field at long times. This chemical dynamics can be considered either as an approximation to more complex chemical or biological evolutions, with maximum chemical Lyapunov exponent $-b$, or as a description of simple specific processes such as spontaneous decomposition of unstable radicals, decay of a radioactive substance, or relaxation of sea-surface temperature towards atmospheric values [32]. The validity of our ideas for nonlinear multicomponent situations has been checked for a plankton model and will be presentend in the next Chapter.

The concentration field $C(\mathbf{r},t)$, when advected by a incompressible velocity field $\mathbf{v}(\mathbf{r},t)$ is governed by the equation

$$\frac{\partial C}{\partial t} + \mathbf{v}(\mathbf{r},t)\cdot\nabla C = S(\mathbf{r}) - bC + \kappa\nabla^2 C, \tag{3.2}$$

where κ is the diffusion coefficient, b is the decay rate introduced above and $S(\mathbf{r})$ is the concentration input from chemical sources (negative values representing sinks). We restrict our study to the case in which the incompressible velocity field is two-dimensional, smooth, and non-turbulent. Chaotic advection is obtained generically if a simple time-dependence, for example periodic, is included in $\mathbf{v}(\mathbf{r},t)$. We assume that diffusion is weak and transport is dominated by advection. Thus one expects that the distribution on scales larger than a certain diffusive scale is not affected by diffusion. Therefore we consider the limiting non-diffusive case $\kappa = 0$. In this limit the above problem can be described in a Lagrangian picture by an ensemble of ordinary differential equations

$$\frac{d\hat{\mathbf{r}}}{dt} = \mathbf{v}(\hat{\mathbf{r}},t), \tag{3.3}$$

$$\frac{d\hat{C}}{dt} = S[\hat{\mathbf{r}}(t)] - b\hat{C}, \tag{3.4}$$

where the solution of the first equation gives the trajectory of a fluid parcel, $\hat{\mathbf{r}}(t)$, while the second one describes the Lagrangian chemical dynamics in this fluid element: $\hat{C}(t) \equiv C[\mathbf{r} = \hat{\mathbf{r}}(t), t]$.

To obtain the value of the chemical field at a selected point $\bar{\mathbf{r}}$ at time $\bar{t}$ one needs to know the previous history of this fluid element, that is the trajectory $\hat{\mathbf{r}}(t)$ $(0 \le t \le \bar{t})$ with the property $\hat{\mathbf{r}}(\bar{t}) = \bar{\mathbf{r}}$. This can be obtained by the integration of (3.3) backwards in time. Once $\hat{\mathbf{r}}(t)$ has been obtained, the solution of (3.4) is

$$C(\bar{\mathbf{r}},\bar{t}) = C[\hat{\mathbf{r}}(0),0]e^{-b\bar{t}} + \int_0^{\bar{t}} S[\hat{\mathbf{r}}(t)]e^{-b(\bar{t}-t)}dt. \tag{3.5}$$

One can obtain the difference at time $\bar{t}$ of the values of the chemical field at two different points $\bar{\mathbf{r}}$ and $\bar{\mathbf{r}} + \overline{\delta\mathbf{r}}$ separated by a small distance $\overline{\delta\mathbf{r}}$ in terms of the difference $C[\hat{\mathbf{r}}(t) + \widehat{\delta\mathbf{r}}(t), t] - C[\hat{\mathbf{r}}(t), t] \equiv \delta C[\hat{\mathbf{r}}(t), t; \widehat{\delta\mathbf{r}}(t)]$ for $0 \le t \le \bar{t}$, namely:

$$\begin{aligned}\delta C(\bar{\mathbf{r}},\bar{t};\overline{\delta\mathbf{r}}) &= \delta C[\hat{\mathbf{r}}(0),0;\widehat{\delta\mathbf{r}}(0)]e^{-b\bar{t}} \\ &+ \int_0^{\bar{t}} \delta S[\hat{\mathbf{r}}(t);\widehat{\delta\mathbf{r}}(t)]e^{-b(\bar{t}-t)}dt\end{aligned} \tag{3.6}$$

where $\widehat{\delta\mathbf{r}}(t)$ $(0 \le t \le \bar{t})$ is the time-dependent distance between the two trajectories that end at $\bar{\mathbf{r}}$ and $\bar{\mathbf{r}} + \overline{\delta\mathbf{r}}$ at time $\bar{t}$, and δS, in analogy with δC, is the difference of the source term at points $\hat{\mathbf{r}}(t)$ and $\hat{\mathbf{r}}(t) + \widehat{\delta\mathbf{r}}(t)$.

Thus we have expressed the behavior of an Eulerian quantity $\delta C(\bar{\mathbf{r}},\bar{t};\overline{\delta\mathbf{r}})$ in terms of Lagrangian quantities, in particular of $\widehat{\delta\mathbf{r}}(t)$. Further analysis of Eq. (3.6) requires specification of the behavior of $\widehat{\delta\mathbf{r}}$. The signature of chaotic advection is the exponentially growing behavior of this quantity at long times. More precise statements need additional assumptions on the character of the flow. The simplest framework is obtained if we restrict our attention to initial conditions $\hat{\mathbf{r}}(0)$ in an invariant *hyperbolic* set [31]. In this case one can identify at each point two directions, the one in which the flow is *contracting* $\mathbf{c}(\mathbf{r})$ and the *expanding* direction $\mathbf{e}(\mathbf{r})$. They depend continuously on position (for time-dependent flows there is an additional explicit time-dependence that we do not write down to simplify the notation). Since $\mathbf{c}$ and $\mathbf{e}$ form at each point a vector basis which is not orthonormal, it is convenient to introduce also the dual basis ($\mathbf{c}^\dagger, \mathbf{e}^\dagger$) at each point. Chaotic advection manifests itself in the fact that for any initial separations $\hat{\delta\mathbf{r}}(0)$ the long-time behavior of $\hat{\delta\mathbf{r}}$ is $|\hat{\delta\mathbf{r}}(t)| \sim \left|\mathbf{e}[\hat{\mathbf{r}}(0)]^\dagger \cdot \hat{\delta\mathbf{r}}(0)\right| e^{\lambda t}$ (for $t > 0$), where λ is the positive Lyapunov exponent along the trajectory and $\mathbf{e}[\hat{\mathbf{r}}(0)]^\dagger \cdot \hat{\delta\mathbf{r}}(0)$ gives the component of the initial separation along the expanding direction. At long times, the direction of $\hat{\delta\mathbf{r}}(t)$ tends to become aligned with the expanding direction of the flow at $\hat{\mathbf{r}}(t)$, $\mathbf{e}[\hat{\mathbf{r}}(t)]$. However, if the initial separation is aligned with the contracting direction at the initial point, λ should be substituted by λ', the contractive Lyapunov exponent, and $\mathbf{e}^\dagger$ by $\mathbf{c}^\dagger$. For incompressible flows one has $\lambda' = -\lambda$. The Lyapunov exponent λ of the trajectory depends in principle both on the initial position and on the duration of the trajectory, $\lambda = \lambda((\hat{\mathbf{r}}(0), t)$. For clarity of the formulas, we suppress in our notation these dependencies. In the limit of infinitely long times, an asymptotic value $\lambda(\hat{\mathbf{r}}(0), \infty) \equiv \lambda((\hat{\mathbf{r}}(0))$ is attained. In the rest of this Section we assume that this limit is reached fast enough so that we can neglect the time-dependence on λ. The space (initial condition) dependence of the infinite-time Lyapunov exponent λ (for hyperbolic systems) is such that almost all initial conditions lead to the same value λ_0, the most probable Lyapunov exponent, whereas deviations may possibly occur in sets of zero measure [36].

In order to analyze (3.6) one has to consider the backwards evolution. In this case typical solutions behave, for $t < 0$ and large, as $|\hat{\delta\mathbf{r}}(t)| \sim \left|\mathbf{c}[\hat{\mathbf{r}}(0)]^\dagger \cdot \hat{\delta\mathbf{r}}(0)\right| e^{\lambda' t} = \left|\mathbf{c}[\hat{\mathbf{r}}(0)]^\dagger \cdot \hat{\delta\mathbf{r}}(0)\right| e^{-\lambda t}$ so that, also in this backwards dynamics, close initial conditions diverge, and the difference will tend to become aligned with the most expanding direction of the backwards flow (the contracting of the forward flow, $\mathbf{c}[\hat{\mathbf{r}}(t)]$). Again, there is a particular direction for the orientation of the initial condition (the contracting one in the backwards flow which is the expanding one in the forward dynamics) for which $-\lambda$ should be replaced by λ. In (3.6), $\hat{\delta\mathbf{r}}$ is obtained backwards starting from $\bar{\delta\mathbf{r}}$ at $t = \bar{t}$. In this case:

$$\hat{\delta\mathbf{r}}(t) \approx \mathbf{c}(\bar{\mathbf{r}})^\dagger \cdot \bar{\delta\mathbf{r}}\, e^{\lambda(\bar{t}-t)}\mathbf{c}[\hat{\mathbf{r}}(t)]\ , \quad t_s \leq t \leq \bar{t}\ . \tag{3.7}$$

The exponential separation (3.7) holds only while the distance $\hat{\delta\mathbf{r}}(t)$ is not too large, and saturates when approaching the size of the system or some characteristic coherence length of the velocity field. The time at which this happens defines t_s, a saturation time. We assume that both the velocity field and the source $S(\mathbf{r})$ have only large-scale structures such that their corresponding coherence lengths are comparable to the system size, *that we take as the unit of length-scales.* Thus, the saturation time is given by $t_s = \bar{t} + \lambda^{-1} \ln |\bar{\delta\mathbf{r}}|$.

For small $\bar{\delta\mathbf{r}}$, Eq. (3.6) can be written as

$$\begin{aligned}\delta C(\bar{\mathbf{r}}, \bar{t}; \bar{\delta\mathbf{r}}) &\approx \delta C[\hat{\mathbf{r}}(0), 0; \hat{\delta\mathbf{r}}(0)]e^{-b\bar{t}} \\ &+ \int_0^{t_s} \delta S[\hat{\mathbf{r}}(t); \hat{\delta\mathbf{r}}(t)]e^{-b(\bar{t}-t)}dt\end{aligned}$$

$$+\int_{t_s}^{\bar{t}} \hat{\delta\mathbf{r}}(t)\cdot\nabla S[\hat{\mathbf{r}}(t)]e^{-b(\bar{t}-t)}dt \tag{3.8}$$

(if $t_s > 0$). We will not need to specify the dependence of δS on $\hat{\delta\mathbf{r}}$ for times previous to t_s, as long as δS remains bounded. Substitution of (3.7) in the second integral leads to

$$\begin{aligned}\delta C(\bar{\mathbf{r}},\bar{t};\bar{\delta\mathbf{r}}) &\approx \delta C[\hat{\mathbf{r}}(0),0;\hat{\delta\mathbf{r}}(0)]e^{-b\bar{t}}\\ &+\int_0^{t_s}\delta S[\hat{\mathbf{r}}(t);\hat{\delta\mathbf{r}}(t)]e^{-b(\bar{t}-t)}dt\\ +\bar{\delta\mathbf{r}}\cdot\mathbf{c}(\bar{\mathbf{r}})^{\dagger}&\int_{t_s}^{\bar{t}}\mathbf{c}[\hat{\mathbf{r}}(t)]\cdot\nabla S[\hat{\mathbf{r}}(t)]e^{(\lambda-b)(\bar{t}-t)}dt\end{aligned} \tag{3.9}$$

Taking the limit $\bar{\delta\mathbf{r}}\to 0$ (for a finite $\bar{t}$) leads to $t_s < 0$. Thus the first integral disappears and the first term can be linearized. By writing $\bar{\delta\mathbf{r}} = \bar{\mathbf{n}}|\bar{\delta\mathbf{r}}|$ so that $\bar{\mathbf{n}}$ is a unit vector, one finds the directional derivative along the direction of $\bar{\mathbf{n}}$ as

$$\begin{aligned}\bar{\mathbf{n}}\cdot\nabla C(\bar{\mathbf{r}},\bar{t}) &\approx \bar{\mathbf{n}}\cdot\mathbf{c}(\bar{\mathbf{r}})^{\dagger}\mathbf{c}[\hat{\mathbf{r}}(0)]\cdot\nabla C[\hat{\mathbf{r}}(0),0]e^{(\lambda-b)\bar{t}}\\ &+\bar{\mathbf{n}}\cdot\mathbf{c}(\bar{\mathbf{r}})^{\dagger}\int_0^{\bar{t}}\mathbf{c}[\hat{\mathbf{r}}(t)]\cdot\nabla S[\hat{\mathbf{r}}(t)]e^{(\lambda-b)(\bar{t}-t)}dt\ .\end{aligned} \tag{3.10}$$

If $\lambda < b$ this derivative remains finite in the $\bar{t}\to\infty$ limit and the asymptotic field $C_\infty(\bar{\mathbf{r}}) \equiv C(\mathbf{r},\bar{t}\to\infty)$ is smooth (differentiable). Otherwise the derivatives of C diverge as $\sim e^{(\lambda-b)\bar{t}}$ leading to a nowhere-differentiable irregular asymptotic field. The exception again is the expanding direction of the forward flow: when $\bar{\delta\mathbf{r}}$ points along that direction one should substitute in Eq. (3.10) λ and $\mathbf{c}$ by $-\lambda$ and $\mathbf{e}$, respectively. This directional derivative is always finite. Thus, there is at each point a direction along which C_∞ is smooth. It should be noted that, because the explicit time-dependence of the vectors $\mathbf{c}$ and $\mathbf{e}$ referred to before, the limiting distribution C_∞ will not be a steady field, but one following the time dependence of the stable and unstable directions. For time-periodic flows $\mathbf{v}(\mathbf{r},t)$, C_∞ will also be time periodic. Its singular characteristics however do not change in time.

In order to characterize the singular asymptotic field we take the limit $\bar{t}\to\infty$ for fixed finite $\bar{\delta\mathbf{r}}$ in (3.9)

$$\begin{aligned}\delta C_\infty(\bar{\mathbf{r}};\bar{\delta\mathbf{r}}) &\approx \int_{|\bar{\delta\mathbf{r}}|^{-1/\lambda}}^{\infty}\delta S[\hat{\mathbf{r}}(x);\hat{\delta\mathbf{r}}(x)]x^{-b-1}dx\\ +|\bar{\delta\mathbf{r}}|\bar{\mathbf{n}}\cdot\mathbf{c}(\bar{\mathbf{r}})^{\dagger}&\int_1^{|\bar{\delta\mathbf{r}}|^{-1/\lambda}}\mathbf{c}[\hat{\mathbf{r}}(x)]\cdot\nabla S[\hat{\mathbf{r}}(x)]x^{\lambda-b-1}dx\end{aligned} \tag{3.11}$$

where we used the change of variables $e^{\bar{t}-t}\to x$. If $b>\lambda$ one finds for the dominant term in the $|\bar{\delta\mathbf{r}}|\to 0$ limit the simple scaling $\delta C_\infty \sim |\bar{\delta\mathbf{r}}|$, but when $b<\lambda$:

$$\delta C_\infty(\bar{\mathbf{r}};\bar{\delta\mathbf{r}}) \sim |\bar{\delta\mathbf{r}}|^{\frac{b}{\lambda}}\ . \tag{3.12}$$

According to (3.1) the value of the Hölder exponent is

$$\alpha = \min\left\{\frac{b}{\lambda},1\right\}. \tag{3.13}$$

This general relation expresses the local (space-dependent) Hölder exponent in terms of the local infinite-time Lyapunov exponent and the chemical decay rate. For hyperbolic systems this Lyapunov exponent has the value λ_0 everywhere but in a set of zero measure.

The smooth-filamental transition can best be understood by neglecting the fluctuations in the Lyapunov spectrum. Hence we study first (in the remaining of this Section) the consequences of Eq. (3.13) for $\lambda = \lambda_0$. In Section 3.3 we will consider open flows. For such systems, it becomes evident that the resulting chemical field cannot be characterized by a single Hölder exponent. In Section 3.4 a structure-function formalism will be presented as a convenient way to characterize this dispersion in the values of the local Hölder exponent.

Coming back to (3.13) with $\lambda = \lambda_0$, for $b > \lambda_0$ the asymptotic chemical field is smooth ($\alpha_0 = \min\{b/\lambda_0, 1\} = 1$). But if $b < \lambda_0$, the asymptotic chemical field becomes an irregular fractal object. Since there is always an orientation of $\delta\mathbf{r}$ along which $\alpha_0 = 1$, the object has a *filamental* structure, that is, irregular in all directions but one where it is smooth. The graph of the field along a one-dimensional cut or transect, or the contours of constant concentration are also fractals, as they are two-dimensional sections of the whole $C_\infty(\mathbf{r})$ embedded in a three-dimensional space. More precisely, the one-dimensional transect (along the direction x) of the field is a self-affine function with its graph embedded in an inherently anisotropic space (C, x) with axis representing different physical quantities. Contours of constant concentrations, however, are self-similar fractal sets of the two-dimensional physical space (x, y). The fractal dimension of both the graph of the transects and of the isolines is given by $D = 2 - \alpha_0$.

In Figs. 3.1 and 3.2 we present snapshots of the asymptotic field C_∞ evolving according to (3.3)-(3.4). For the flow we take a simple time-periodic velocity field defined in the unit square with periodic boundary conditions by

$$\begin{aligned} v_x(x,y,t) &= -\frac{2U}{T}\Theta\Big(\frac{T}{2} - t \bmod T\Big)\cos(2\pi y) \\ v_y(x,y,t) &= -\frac{2U}{T}\Theta\Big(t \bmod T - \frac{T}{2}\Big)\cos(2\pi x) \end{aligned} \qquad (3.14)$$

where $\Theta(x)$ is the Heavyside step function. In our simulations $U = 1.2$, which produces a flow with a single connected chaotic region in the advection dynamics. The value of the numerically obtained Lyapunov exponent is $\lambda_0 \approx 2.67/T$.

Backward trajectories with initial coordinates on a rectangular grid were calculated and used to obtain the chemical field at each point by using (3.5) forward in time with the source term $S(x, y) = 1 + \sin(2\pi x)\sin(2\pi y)$. The values of the parameters used in Fig. 3.1 are $T = 1.0$ and $b = 4.0$, for which the Lyapunov exponent is $\lambda_0 = 2.67 < b$. A smooth pattern is seen, in agreement with our theoretical arguments. In Fig. 3.2 the parameters are $T = 1.0$ and $b = 0.1$, so that $\lambda_0 > b$ and a filamental pattern is obtained.

The smooth-fractal transition also appears in the time-dependence of the concentration measured at a fixed point in space. This can be shown by a similar analysis for the difference

$$\delta C(\mathbf{r}, t; \delta t) \equiv C(\mathbf{r}, t + \delta t) - C(\mathbf{r}, t) \qquad (3.15)$$

instead of the spatial difference discussed above. If $b < \lambda_0$ the signal $C(\mathbf{r}, t)$ becomes non-differentiable in time and can be characterized by the same Hölder exponent b/λ_0. The

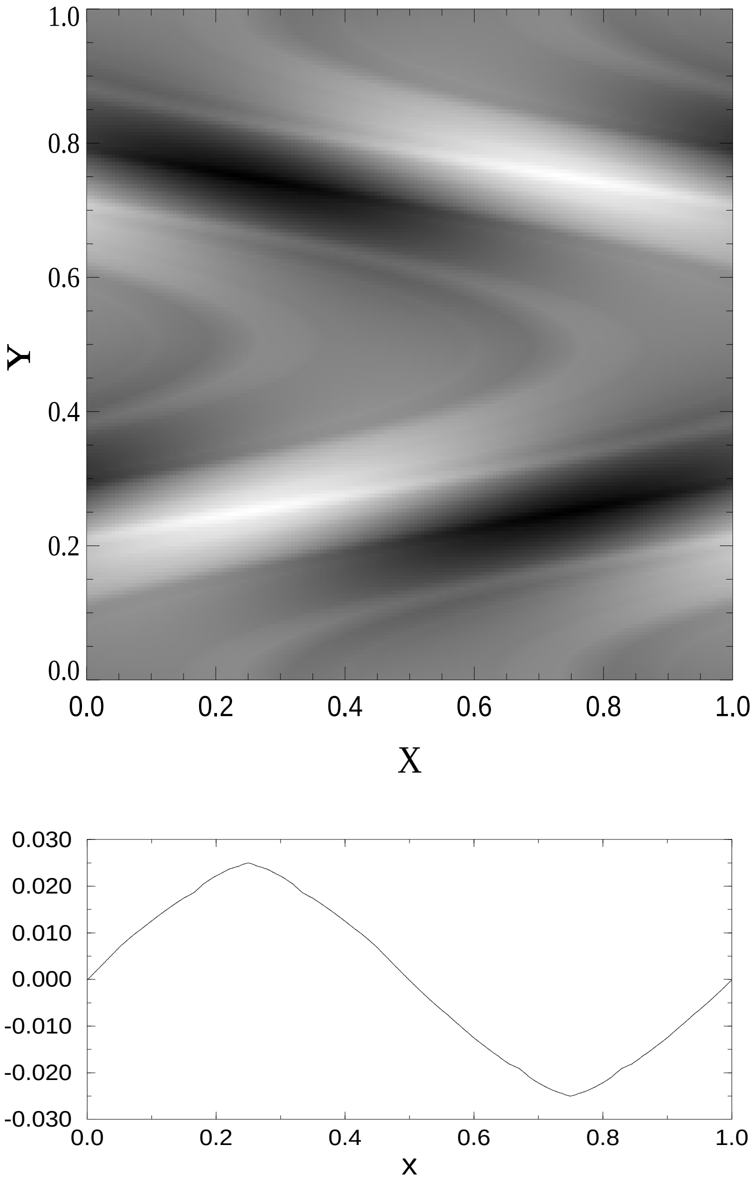

Figure 3.1: Top: a snapshot of the chemical concentration C_∞ obtained in the flow (3.14) for $b = 4.0$ and $\lambda_0 = 2.67$, so that a smooth distribution is obtained. Bottom: a horizontal cut along the line $y = 0.25$.

fact that scaling properties of the temporal signal and that of the spatial structure are the same –analogously to the so called ‘Taylor hypothesis’ in turbulence– can be exploited in

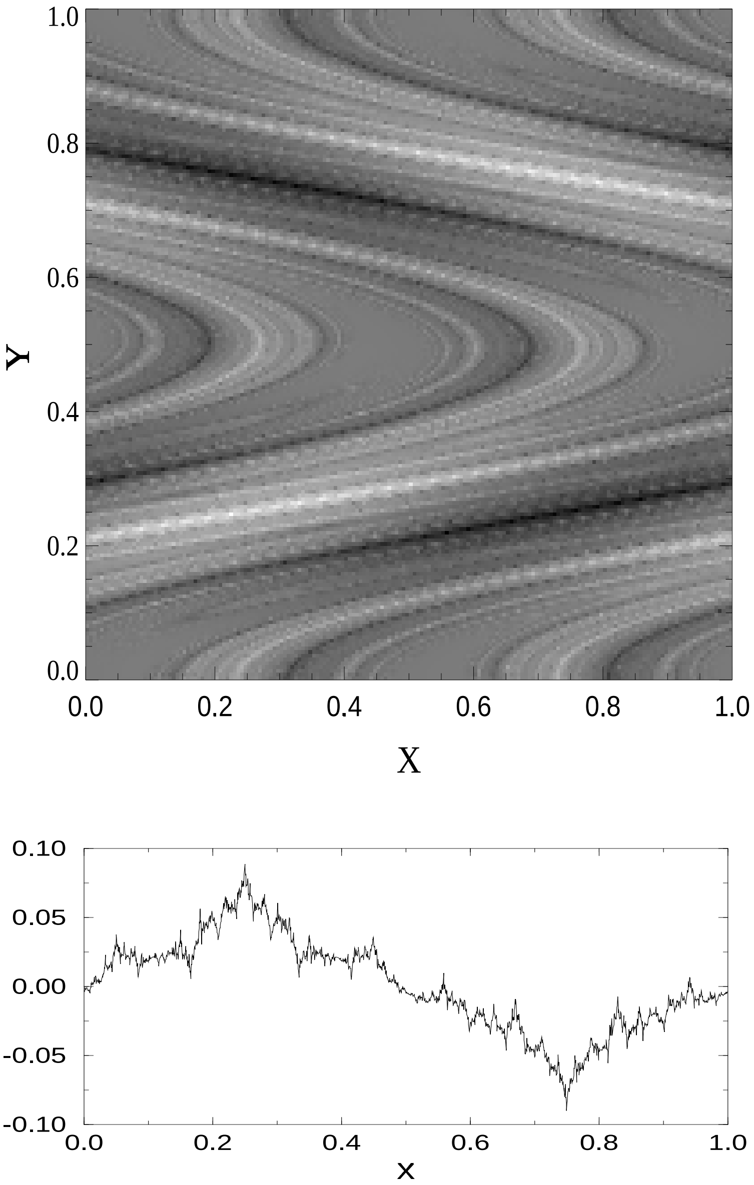

Figure 3.2: Top: a snapshot of the chemical concentration C_∞ for $b = 0.1$ and $\lambda_0 = 2.67$, so that a filamental structure is obtained. The lower panel shows a horizontal cut along the line $y = 0.25$, clearly displaying the fractal nature of the field.

experiments or in analysis of geophysical data.

We conclude with some comments on the range of validity of Eq. (3.10). The Lagrangian description (3.3)-(3.4) in which our approach is based is valid only for scales at which diffusion is negligible. Thus there is a minimum admissible value $l_{diff}(\kappa) \sim \sqrt{\kappa}$ of $\bar{\delta \mathbf{r}}$ and our calculation should be understood as giving the gradients only up to this scale, fractality being washed out at smaller scales by the presence of diffusion. Nevertheless we think that, if diffusion is weak, the fractal-filamental transition will be seen at scales larger than this diffusive scale. For fixed $\bar{\delta \mathbf{r}}$ larger than the diffusion length, (3.9) remains valid until a time $\bar{t} \sim t_s(\bar{\delta \mathbf{r}})$ that means that the divergence of the gradients will also saturate at a finite value $\sim (l_{diff})^{b/\lambda_0 - 1}$.

Another limitation to the validity of our equations arises from the fact that, for most chaotic flows of physical relevance, not all the points visited by the fluid particle will be hyperbolic. The stable and unstable directions in the previous discussion become tangent at some points and equations such as (3.9) become undefined there. More importantly, KAM tori will be present in the system, so that for values of $\bar{\mathbf{r}}$ lying on KAM trajectories the value of the Lyapunov exponent appearing in (3.7) will not be positive but zero. Another effect of the KAM tori will be to partition space into ergodic regions. Each region will be characterized by a different value of λ_0, and there is the possibility of observing different morphologies in the different regions. For the values of parameters used in Figs. 3.1 and 3.2, KAM tori occupy a very small and practically unobservable portion of space, so that the filamental pattern appears to be well described by the same Hölder exponent nearly everywhere. However, an example has been given in the preceding Chapter in which filamental and smooth regions coexist separated by KAM tori.

3.3 Open flows

Let us now consider again the problem (3.3)-(3.4) with a velocity field corresponding to an open flow whose time-dependence is restricted to a finite region (mixing region), with asymptotically steady inflow and outflow regions. A prototype of this flow structure is a stream passing around a cylindrical body. If the inflow velocity is high enough vortices formed in the wake of the cylinder make the flow time-dependent in this region, while the flow remains steady in front of the cylinder or in the far downstream region. We assume again that the flow is non-turbulent, so that the velocity field is spatially-smooth.

Passive advection in such open flows was found to be a nice example of chaotic scattering[23, 33]. Advected particles (or fluid elements) enter the unsteady region, undergo transient chaotic motion [34], and finally escape and move away downstream on simple orbits. The time spent in the mixing region, however, depends strongly on the initial coordinates, with singularities on a fractal set corresponding to particles trapped forever in the mixing region. This is due to the existence of a non-attracting chaotic saddle (although of zero measure) formed by an infinite number of bounded hyperbolic orbits in the mixing region. The stable manifold of this chaotic saddle contains orbits coming from the inflow region but never escaping from the mixing zone. These points correspond to the singularities of the residence time. If a droplet of dye is injected into the mixing region so that it overlaps with the stable manifold, most of it will be advected downstream in a short time. But part of the dye will remain close to the chaotic saddle for very long times, and continuously ejected along its unstable manifold. In this way the dye traces out the unstable manifold of the chaotic saddle, resulting in fractal patterns characteristic to open flows[23, 33, 35]. Permanent chaotic advection is restricted to a fractal set of zero Lebesgue measure, the chaotic saddle. Points close to the unstable manifold of the chaotic saddle have spent a long time in the mixing region of the flow moving near chaotic orbits with a positive Lyapunov exponent. For points precisely at this unstable manifold, the backwards trajectories (the ones from which the Lyapunov exponent in (3.13) should be computed) remain in the chaotic saddle, thus leading to $\lambda_0 > 0$. The other trajectories escape from the chaotic saddle in a short time, thus being characterized by a Lyapunov exponent equal to zero.

Thus open flows provide a rather clear example of strong space-dependence of Lyapunov exponents. According to Eq. (3.13), the Hölder exponent may be different from 1 only on the unstable manifold of the chaotic saddle, thus implying that the transition from smooth to filamental structure now only takes place in this fractal set of zero measure. The background chemical field is always smooth, independently of the value of b.

To check these ideas, we obtain numerically the distributions of chemical fields advected by an open flow. Our velocity field is taken from a kinematic model of a time-periodic flow behind a cylinder, described in [23]. This flow was found to be qualitatively similar to the solution of the Navier-Stokes equation in the range of the Reynolds number corresponding to time-periodic vortex seeding. The concentration pattern shows irregularities separated by smooth regions (Fig. 3.3, obtained with $b = 0.96$). This is more clearly observed in the longitudinal transect. The relation between the singular regions and the location of the chaotic saddle can be made patent by comparing the gradient of the field with the spatial dependence of the escape times from the scattering region. In particular, Fig. 3.4 shows the absolute value of the gradient of the concentration field $|\nabla C_\infty(\mathbf{r})|$ that is highly intermittent. It also displays the time (in the time-reversed dynamics) that fluid particles initially in a line perpendicular to the mean flow take to escape the region of chaotic motion. Most of the particles leave the region in a short time, but longer times appear for initial locations close to the stable manifold (in the time-reversed dynamics) of the chaotic saddle. Clearly, these diverging times are associated to the singularities in the gradient distribution. By increasing the value of b the flow characteristics (trajectories, manifolds, escape times, ...) remain unchanged, but the singularities in the advected field decrease and finally a smooth distribution is obtained.

A chemical field with the same structure can also be obtained in open flows whose time-dependence (and thus the chaoticity of advection) is not restricted to a finite domain, by restricting the spatial dependence of the chemical sources to a finite region. This case will be investigated in the context of plankton dynamics in the nex Chapter.

Since the irregularities now appear only on a set of measure zero, one could ask if they can have any significant effect on measurable quantities. In order to clarify this, instead of the previous characterization of the point-wise strength of the singularities by the Hölder exponent, let us investigate the scaling of the spatial average of the differences δC_∞ with distance $\delta r \equiv |\delta \mathbf{r}|$. For simplicity, let us assume that, on the saddle, there is no distribution in the local infinite-time Lyapunov exponents, i.e., that the advection on the chaotic saddle is characterized by a single Lyapunov exponent λ_0. In this case the partial fractal dimension (i.e. the dimension of intersections of the set with a line) of the manifolds of the chaotic

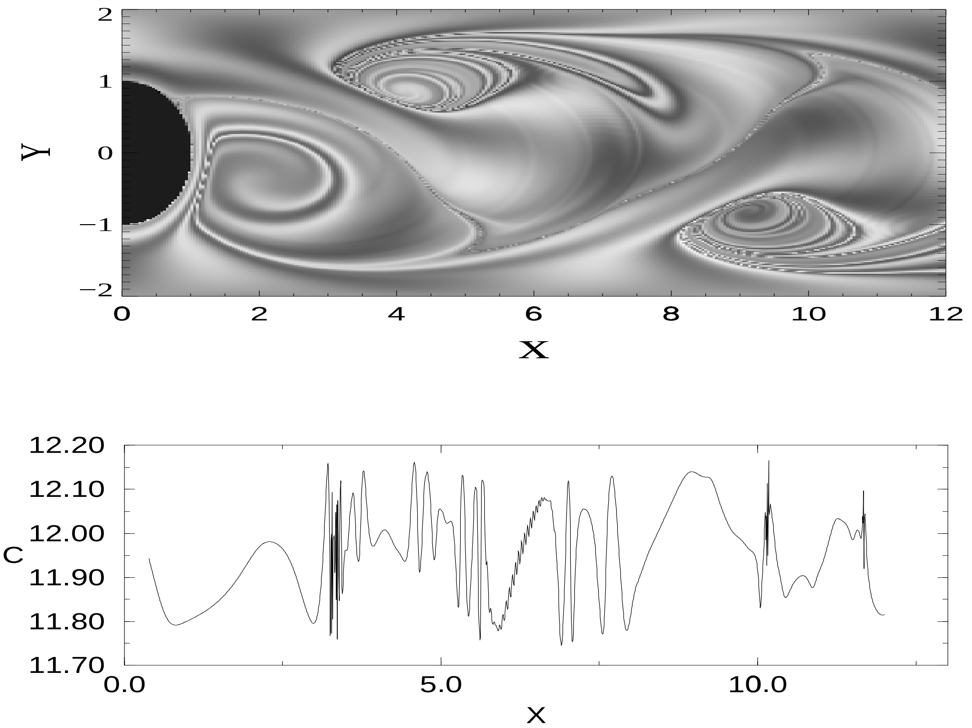

Figure 3.3: Top: a snapshot of the chemical pattern C_∞ formed in the wake of a cylinder (the black semicircle at the left is half of its section). Mean flow is from left to right. We have used the streamfunction given in reference [15]. $b = 0.96$, and all the streamfunction parameter values are the same as in [15] except the boundary-layer thickness of the cylinder which here takes the value $a = 20.0$, and the vorticity strength which is $\omega = 35.06$ in our calculations. Bottom: a horizontal cut taken along the line $y = 1.0$.

saddle is [23, 36]

$$\tilde{D} = 1 - \frac{\kappa}{\lambda_0}. \tag{3.16}$$

Here κ is the escape rate, that is the rate of the exponential decay ($\sim e^{-\kappa t}$) of the number of fluid elements spending time longer than t in the wake of the cylinder. On a one-dimensional transect of unit length the total number of segments of length δr is $(\delta r)^{-1}$ while the number of segments containing parts of the unstable manifold (with partial fractal dimension $\tilde{D}$) is $N(\delta r) \sim \delta r^{-\tilde{D}}$. Thus, according to (3.13) the spatial average of δC_∞ along this line, $\langle \delta C_\infty(\mathbf{r}; \delta r) \rangle$, can be written as

$$\begin{aligned} \langle \delta C_\infty(\mathbf{r}; \delta r) \rangle = (\delta r)(\delta r)^{-\tilde{D}}(\delta r)^{b/\lambda_0} + \\ +(\delta r)[(\delta r)^{-1} - (\delta r)^{-\tilde{D}}](\delta r) \end{aligned} \tag{3.17}$$

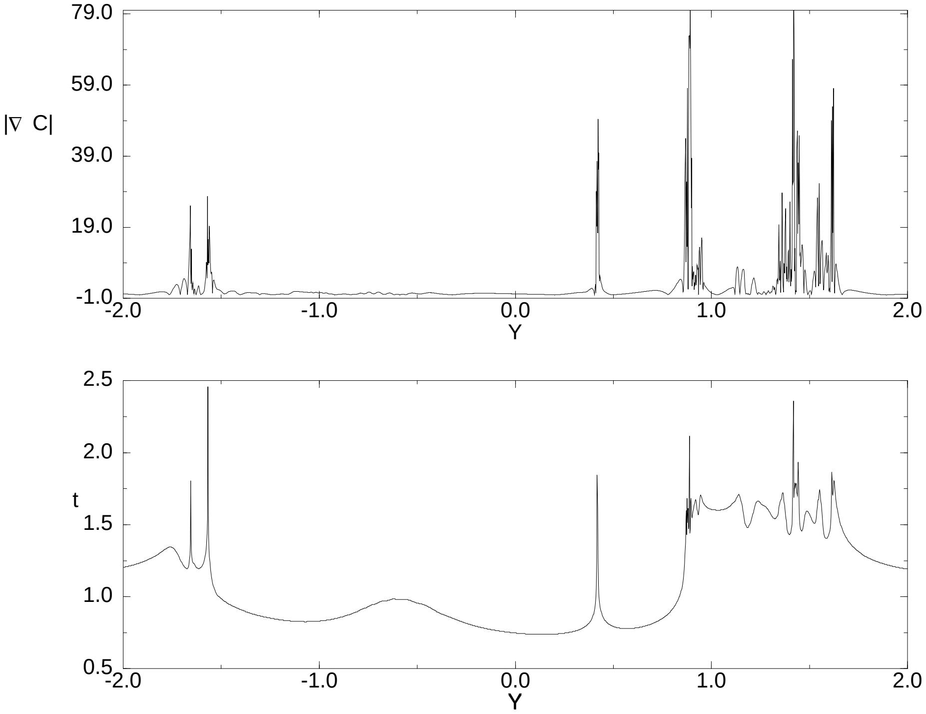

Figure 3.4: Top: The absolute value of the gradient of the chemical field in Fig. 3.3 along the line $x = 7.3$. The lower figure shows the escape time for particles along this line ($x = 7.3$). This is calculated by computing the time that every single particle takes to arrive to the line $x = -2.0$ (far from the chaotic wake region) in the backwards-in-time dynamics.

where the first term pertains to the singular, while the second one to the smooth component. In the limit $\delta r \to 0$ the dominating behavior is

$$\langle \delta C_\infty(\mathbf{r}; \delta r) \rangle \sim \delta r^\zeta \quad , \tag{3.18}$$

with

$$\zeta = \min\left\{1, 1 + b/\lambda_0 - \tilde{D}\right\} = \min\left\{1, \frac{b+\kappa}{\lambda_0}\right\} \tag{3.19}$$

showing that if $\tilde{D} < \frac{b}{\lambda_0}$ (or, $b + \kappa > \lambda_0$) the average will be dominated by the smooth component, but if the fractal dimension of the singular set is large enough they contribute to the scaling of $\langle \delta C_\infty(\mathbf{r}; \delta r) \rangle$. The average has been performed along a one-dimensional line or transect of the two-dimensional pattern. For common velocity fields and transects this will be equivalent to the complete average over the whole fluid, except in the particular case in which the transect is chosen to be completely aligned with the filaments.

3.4 Structure functions

The strongly intermittent structure of singularities in open flows is an extreme example. There are additional inhomogeneities affecting both to the open and to the closed flows: although, in the long-time limit the Lyapunov exponent is the same for almost all trajectories in an ergodic region, deviations can persist on fractal sets of measure zero, and as we saw above such sets can contribute significantly to the global scaling. The origin of these inhomogeneities can be traced back by analyzing the finite-time distribution of Lyapunov exponents. This will be done in the following. For a robust quantitative characterization of the filamental structure, accessible to measurements, we consider now the scaling properties of the structure functions associated with the chemical field.

The qth order structure function is defined as

$$S_q(\delta r) = \langle |\delta C_\infty(\mathbf{r}; \delta r)|^q \rangle \tag{3.20}$$

where $\langle\ \rangle$ represents averaging over different locations $\mathbf{r}$, and q is a parameter (we will only consider structure functions of positive order ($q > 0$)). In the absence of any characteristic length over a certain range of scales the structure functions are expected to exhibit, as $\delta r \to 0$, a power-law dependence

$$S_q(\delta r) \sim \delta r^{\zeta_q} \tag{3.21}$$

characterized by the set of scaling exponents ζ_q.

We also note that some of the scaling exponents are directly related to other characteristic exponents, such as the one characterizing the decay of the Fourier power-spectrum $\Gamma(k) \sim k^{-\gamma}$, or the box-counting fractal dimension D_G of the graph of the function $C_\infty(x, y)$ as a function of x by simple relations [36]:

$$\gamma = \zeta_2 + 1 \quad \text{and} \quad D_G = 2 - \zeta_1. \tag{3.22}$$

If the Hölder exponent of the field has the same value everywhere, given by (3.13) with $\lambda = \lambda_0$, the scaling exponents of the resulting *mono-affine* field are simply

$$\zeta_q = q\alpha_0 = q\frac{b}{\lambda_0}. \tag{3.23}$$

(we have assumed $b < \lambda_0$). In general, the singular spatial inhomogeneities of the Lyapunov exponent could be understood by realizing that the finite-time stretching rates, or local Lyapunov exponents [4], have a certain distribution around the most probable value. This distribution approaches the time-asymptotic form [4, 36]:

$$P(\lambda, t) \sim t^{1/2} e^{-G(\lambda)t} \tag{3.24}$$

where $G(\lambda)$ is a function characteristic to the advection dynamics, with the property that $G(\lambda_0) = G'(\lambda_0) = 0$ and $G(\lambda) > 0$, where λ_0 is the most probable value of the Lyapunov exponent. At infinitely-long times all the measure becomes concentrated at this single value λ_0, as stated before. The form (3.24) is valid only for hyperbolic systems. Non-hyperbolicity (i.e. the presence of KAM tori) can strongly affect the distribution at small values of λ but around λ_0 and for larger values it remains a good approximation. As we shall see later only this region contributes to the structure functions of positive order.

As time increases the distribution becomes more and more peaked around λ_0. The (Lebesgue) area of the set of initial conditions with local Lyapunov exponents in a small interval $(\lambda, \lambda + \delta\lambda)$ that excludes λ_0 decreases at long times with a dominant exponential behavior:

$$\delta A_\lambda(t) \sim e^{-G(\lambda)t}\delta\lambda \tag{3.25}$$

showing that only sets of measure zero can have Lyapunov exponent different from λ_0 in the $t \to \infty$ limit. Such sets, however, can still have nonzero fractal dimensions. At finite times, the area (3.25) encloses the final anomalous set, with a transverse thickness that, due to stretching by the chaotic advection, decreases like $l_\lambda(t) \sim e^{-\lambda t}$. The number of boxes needed to cover the set of area $\delta A_\lambda(t)$ using boxes of size $l_\lambda(t)$ is

$$N_\lambda(t) \sim \frac{\delta A_\lambda(t)}{l_\lambda^2(t)} \sim e^{[2\lambda - G(\lambda)]t} \sim l_\lambda(t)^{\frac{G(\lambda)}{\lambda}-2} \tag{3.26}$$

that gives the dimension for the set to which this area converges in the infinite-time limit:

$$D(\lambda) = 2 - \frac{G(\lambda)}{\lambda}. \tag{3.27}$$

Thus, an arbitrary line across the system will be found composed by subsets of dimension $\tilde{D}(\lambda) = D(\lambda) - 1$ each one characterized by different values λ of the Lyapunov exponents and in consequence of the Hölder exponents $\alpha(\lambda) = \min\{b/\lambda, 1\}$.

Now, the scaling exponents in (3.21) can be readily obtained. The number of segments of size δr belonging to a subset characterized by Lyapunov exponent λ scales as $N(\lambda) \sim \delta r^{-\tilde{D}(\lambda)}$, while the total number of such non-overlapping segments scales as $\sim \delta r^{-1}$. Thus, the structure function can be written as

$$\begin{aligned} S_q(\delta r) &\sim \int_{\lambda_{min}}^{\lambda_{max}} \delta r^{2-D(\lambda)} |\delta C_\infty(r(\lambda), \delta r)|^q d\lambda \sim \\ &\sim \int_{\lambda_{min}}^{b} \delta r^{2-D(\lambda)} \delta r^q d\lambda + \int_{b}^{\lambda_{max}} \delta r^{2-D(\lambda)} \delta r^{qb/\lambda} d\lambda \end{aligned} \tag{3.28}$$

In the limit $\delta r \to 0$ the integrals are dominated by a saddle point and, after some manipulations, the scaling exponents in (3.21) are obtained as

$$\zeta_q = \min_\lambda \left\{ q, \frac{qb}{\lambda} + 2 - D(\lambda) \right\} = \min_\lambda \left\{ q, \frac{qb + G(\lambda)}{\lambda} \right\} \tag{3.29}$$

The right hand side can be seen as a family of lines in the (q, ζ_q) plane labeled by the parameter λ so that the value of ζ_q is given by the lower envelope of these lines. Note that the shape of $G(\lambda)$ for λ small enough becomes irrelevant for determining ζ_q because of the minimum condition. Thus multifractality, characterized by nonlinearity in the q-depencence of ζ_q, is affected only by the largest stretching rates in the flow. Equation (3.19) is a particular case of (3.29) for $q = 1$ and in the approximation of considering a single value of λ on the chaotic saddle.

According to (3.29) the qth order structure function is dominated by a subset characterized by a Lyapunov exponent λ_q. Applying the extremum condition to (3.29) we obtain an equation for λ_q

$$\frac{d}{d\lambda}G(\lambda)|_{\lambda=\lambda_q} = \frac{qb + G(\lambda_q)}{\lambda_q} \tag{3.30}$$

that can be substituted into (3.29) to obtain the qth order scaling exponent.

The existence of a distribution of local Lyapunov exponents also affects the smooth-filamental transition. As the Hölder exponent is space-dependent, the transition does not take place at a uniquely defined value of b. Singularities exist even in a overall smooth regime for points corresponding to backwards trajectories with Lyapunov exponents larger than b. These points occupy fractal sets of dimension $D(\lambda)$ given by (3.27) with $b < \lambda < \lambda_{max}$. Thus, the fractal dimension of the singular set is $\max_{\lambda > b} D(\lambda) = D(b)$, indicating that the set becomes space-filling (see (3.27)) as b approaches $b_c = \lambda_0$. Therefore, the bulk transition, a macroscopic effect that affects the overall appearance of the chemical field, takes place in a closed flow at the same critical value $b_c = \lambda_0$ as in a flow without any spreading in the Lyapunov spectrum.

We note that (3.29) could also be obtained more directly from the averaging of (3.12) over different values of λ using the probability distribution (3.24) of the local Lyapunov exponent. In that case we would not have the geometrical interpretation in terms of fractal dimensions $D(\lambda)$.

We have analyzed numerically the chemical decay under advection by the closed flow (3.14) to check the theoretical predictions above. Numerically computed histograms of the local Lyapunov exponents are shown in Fig. 3.5 and the corresponding $G(\lambda)$ functions are represented in Fig. 3.6. The $G(\lambda)$ functions obtained from histograms corresponding to different times coalesce except in the small-λ region, thus confirming that (3.24) correctly describes the observed distribution.

Numerically calculated scaling exponents (i.e. obtained by direct application of Eq. (3.20)), and the family of lines corresponding to (3.29) based on the histogram of the local Lyapunov exponents of Fig. 3.5 are shown in Fig 3.4, where the prediction of the mono-fractal approximation ($\zeta_q = qb/\lambda_0$) is also shown. The mono-fractal approximation appears to be accurate for small q. The graph-fractal dimension or the widely used Fourier power spectrum exponent are related to ζ_1 and ζ_2 by Eqs. (3.22) so that their estimate based on the mono-fractal description that considers just the bulk value of the Hölder exponent can deviate from the actual values.

In a recent work by Nam et al. [37] the power spectrum of a decaying scalar field (with space-dependent decay rate) has been investigated and related to the distribution of local Lyapunov exponents of the advecting flow. The result for the spectral exponent obtained in [37] using an eikonal-type wave packet model [38], and taking into account finite diffusion, is consistent with our formula (3.29) (that for $q = 2$, and with (3.22) gives the value of the spectral slope) obtained in the non-diffusive limit.

The function $G(\lambda)$ is characteristic to the advecting flow. Let us now consider a special case where we approximate $G(\lambda)$ by a parabola

$$G(\lambda) = \frac{(\lambda - \lambda_0)^2}{2\Delta} \, . \tag{3.31}$$

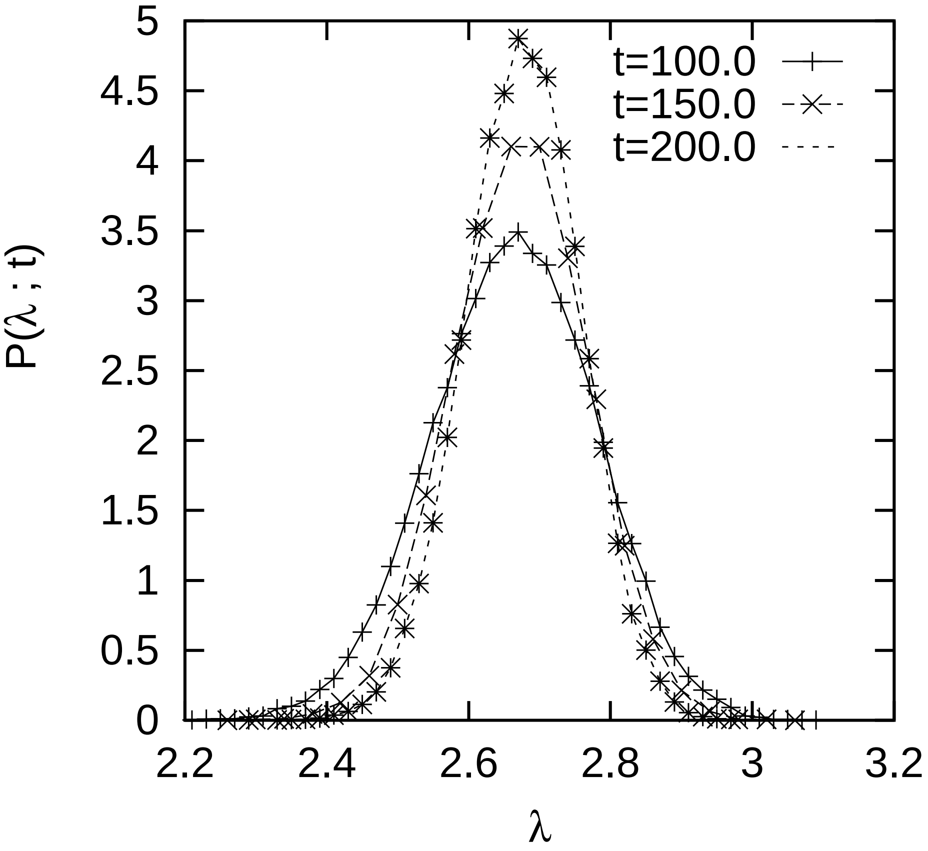

Figure 3.5: The distribution of local Lyapunov exponents at three different times, obtained for the closed flow (3.14) with $T = 1.0$ and $U = 1.2$. The long-time mean Lyapunov exponent is $\lambda_0 = 2.67$.

This can be thought as the first term in a Taylor expansion around λ_0, which is a good approximation to obtain the small-q scaling exponents. In this case (3.30) can be solved explicitly

$$\lambda_q = \sqrt{(\lambda_0)^2 + 2qb\Delta}\,. \tag{3.32}$$

This gives the scaling exponents

$$\zeta_q = \sqrt{\left(\frac{\lambda_0}{\Delta}\right)^2 + \frac{2qb}{\Delta}} - \frac{\lambda_0}{\Delta}. \tag{3.33}$$

The above relation has been obtained recently by Chertkov in [39], where the problem of advection of decaying substances was considered in a probabilistic set-up, using stochastic chemical sources and a random velocity field that is spatially smooth but delta-correlated in time. The distribution of stretching rates was assumed to be Gaussian as in (3.31). This assumption could be realistic for deterministic dynamical systems in many cases, and could give good estimates for the scaling exponents for small q. For higher-order moments, however, higher-order terms in the expansion of $G(\lambda)$ can become important. Moreover, the

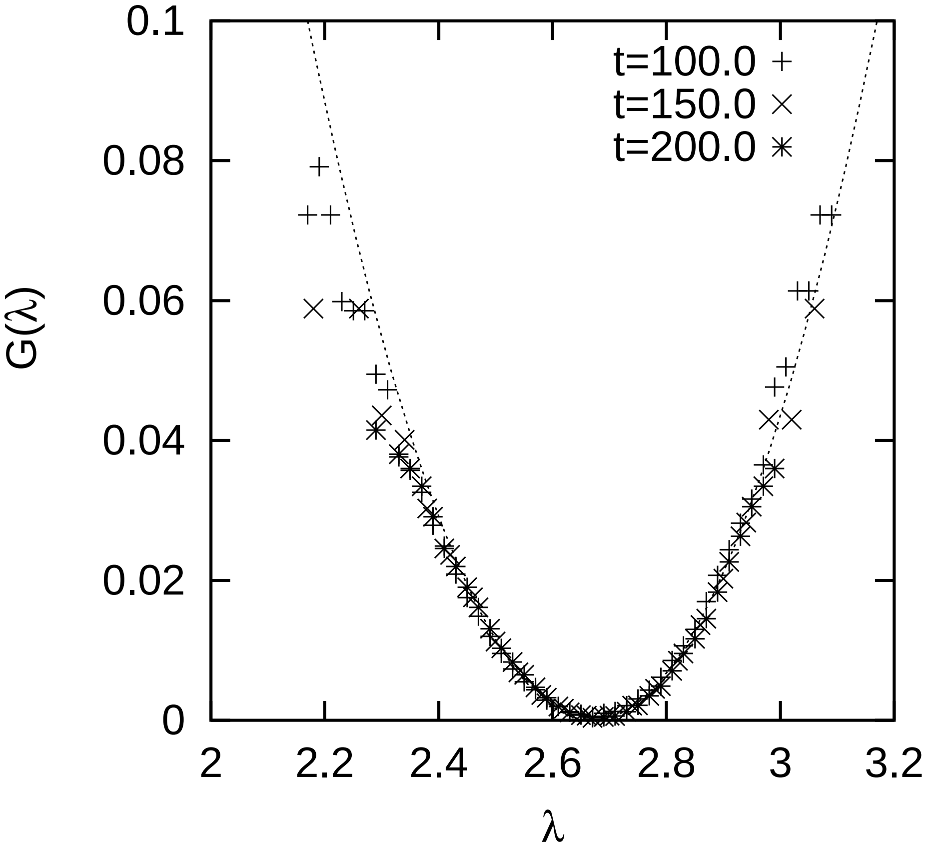

Figure 3.6: The function $G(\lambda)$, obtained from the distributions in Fig. 3.5 and Eq. (3.24). Collapse of data for the three times into the same curve confirms the validity of (3.24). The dotted line is a parabolic fit ($0.4(\lambda - 2.67)^2$) that provides a good approximation near the minimum.

possible values of λ could be limited by a finite maximum value λ_{max}, e.g. in time-periodic flows, where the finite time-Lyapunov exponents cannot have arbitrarily large values. This implies that the scaling exponents for $q > q^*$, where $\lambda_{q^*} = \lambda_{max}$, should display a simple linear dependence

$$\zeta_q = \frac{qb + G(\lambda_{max})}{\lambda_{max}} \tag{3.34}$$

that differs from the $q^{\frac{1}{2}}$ behavior of (3.33) for large q.

3.5 Summary and discussion

Multifractality of advected fields generated by chaotic advection has been observed previously in the case of passive advection with no chemical activity ($b = 0$) [40]. It was shown that the measure defined by the gradients of the advected scalar field has multifractal properties and its spectra of dimensions D_q has been related to the distribution of local

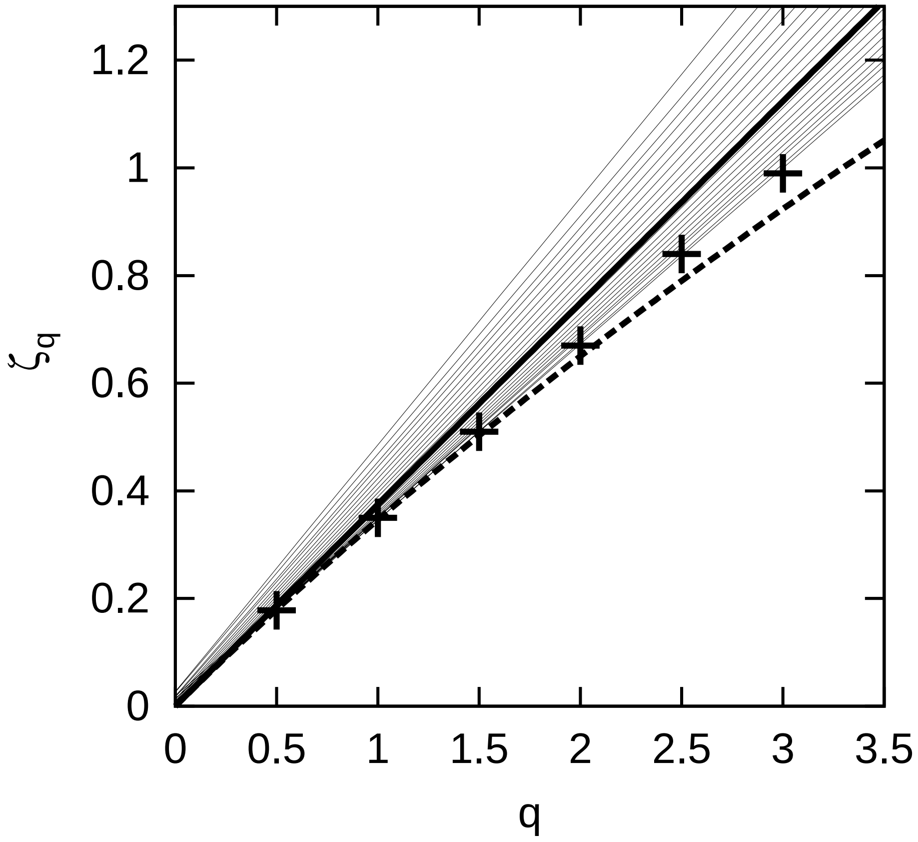

Figure 3.7: The scaling exponents ζ_q for the situation of Figs. 3.5 and 3.6 and with $b = 1.0$. Thick line: the mono-fractal approximation $\zeta_q = qb/\lambda_0$. Thin lines: the curves $\zeta_q = q$ and $\zeta_q = [qb + G(\lambda)]/\lambda$, for different values of λ; the numerical values of $G(\lambda)$ are obtained from Fig. 3.6. According to Eq. (3.29), the actual values of the scaling exponents are given by the lower envelope of this set of curves. This is confirmed by the numerically determined values of ζ_q (crosses). Dashed line: the approximation (3.33).

Lyapunov exponents [40]. This multifractality, however, does not affect the slope of the power spectrum [41, 42] (the so called Batchelor spectrum: $\Gamma(k) \sim k^{-1}$) or scaling exponents of the structure functions ($\zeta_q = 0$ for all q, as it can be seen from (3.29) by setting $b = 0$). The effect of multifractality on the power spectrum has a character transient in time, moving towards smaller and smaller scales and finally disappearing when reaching the diffusive end of the spectrum. In the stationary state only the diffusive cut-off of the power spectrum is affected [43] that can still be important for the interpretation of some experimental results. By comparing these results for the conserved case with the ones presented here for the decaying scalar we can conclude that, although the origin of the multifractality is the same in both situations –the non-uniformity of the local Lyapunov exponents– in the presence of chemical activity this has stronger consequences (non-Batchelor power spectra and anomalous scaling).

We have presented a simple mechanism that can generate multifractal (or more precisely, multi-affine) distributions of advected chemical fields. The main ingredients are chaotic advection and linear decay of the advected quantity in the presence of non-homogeneous sources. Essentially the same mechanisms were considered in [39], but with stochastic time-dependencies both in the flow as in the chemical sources, considering advection by the spatially smooth limit of a Kraichnan-like model generally intended to represent turbulent flows. Our results stress that anomalous scaling may appear in simple regular (e.g. time-periodic) laminar flows where stochasticity appears just as a consequence of the low-dimensional deterministic chaos generated by the Lagrangian advection dynamics. In addition we have provided numerical evidence for the theoretical predictions. It is interesting to mention that the extension of Chertkov's work to nonlinear chemistry [44] finds results very similar to the linear decay, simply substituting the decay rate by an average rate. This is also the result we find within our deterministic models in Chapter 2, being the rate the chemical Lyapunov exponent.

Chaotic advection is characteristic to most time-dependent flows. The linear decay of the advected substance is in fact just the simplest prototype of a family of chemical reaction schemes, where the local dynamics converges towards a fixed point of the chemical rate equations. The local dynamics can also be generated by non-chemical processes, e.g. by biological population dynamics in the case of plankton advection [48], or by the relaxation of the sea-surface temperature towards the local atmospheric value [32]. Inhomogeneities of the chemical sources or of other parameters of the local dynamics arise naturally in these contexts so that we expect our results to be of relevance in biological and geophysical settings. In fact, fractality and multifractality have been already observed in these contexts, for example in the distribution of stratospheric chemicals (e.g. ozone) [45, 46], and in sea-surface temperature and phytoplankton populations [47]. The structure of these fields has been sometimes associated with turbulence of the advecting flow. We think that the simple mechanism, able to generate complex multifractal distributions, investigated in this Chapter can be at the origin of some of the structures observed in geophysical flows. Further work in this direction could help on the interpretation of geophysical data in order to gain quantitative information about the processes involved. Laboratory experiments seem also to be feasible.

Chapter 4

Chaotic advection of reacting substances: Plankton dynamics on a meandering jet

We study the spatial patterns formed by interacting populations or reacting chemicals under the influence of chaotic flows. In particular, we have considered a three-component model of plankton dynamics advected by a meandering jet. We report general results, stressing the existence of a smooth-filamental transition in the concentration patterns depending on the relative strength of the stirring by the chaotic flow and the relaxation properties of planktonic dynamical system. Patterns obtained in open and closed flows are compared.

4.1 Introduction

The transport of biologically or chemically active substances by a fluid flow is a problem of great geophysical relevance. Important examples arise in the study of atmospheric advection of reactive pollutants or chemicals, such as ozone, N_2O [55], or in the dynamics of plankton populations in ocean currents [51]. The inhomogeneous nature of the resulting spatial distributions was recognized some time ago ([58] and references therein). More recently, satellite remote sensing and detailed numerical simulations identify filaments, irregular patches, sharp gradients, and other complex structures involving a wide range of spatial scales in the concentration patterns. In the case of atmospheric chemistry, the presence of strong concentration gradients has been shown to have profound impact on global chemical time-scales [19]. On-site measurements and data analysis of the chemical or biological fields have confirmed their fractal or multifractal character [56, 47, 45, 46].

In the case of plankton communities, *patchiness* has been variously attributed to the interplay of diffusion and biological growth, oceanic turbulence, diffusive instabilities, and nutrient or biological inhomogeneities [54]. Advection by unsteady fluid flow and predator-prey interactions (formally equivalent to chemical reaction) are emerging as two key ingredients able to reproduce the main qualitative features of plankton patchiness [18].

The ‘chaotic advection’ paradigm has been shown to be a useful approach to understand geophysical transport processes at large scales [52]. Briefly, chaotic advection (or Lagrangian chaos) [6, 5] refers to the Lagrangian complex motion of fluid parcels. Lagrangian chaotic flows are much simpler than turbulent ones, being thus more accessible to analytical characterization and understanding. They retain however many of the qualitative features relevant to transport and mixing processes in complex geophysical flows.

Though the properties of inert passive tracer fields under chaotic advection have been widely studied [40] much less is known about biologically or chemically evolving reactant distributions. Nonetheless, some results have been recently obtained, as for example in reactions of the type $A + B \to C$ in closed chaotic flows [20] and in open chaotic flows [22]. In chapters 2, 3 we have considered the general case of stable chemical dynamics in closed chaotic flows in the limit of small diffusion and in the presence of an external spatially non-homogeneous source of one of the chemical components. The main result was that the relationship between the rate at which the chemical dynamics approaches local equilibrium with the chemical source and the characteristic time scale of the stirring by the chaotic flow determines the fractal or non-fractal character of the long-time distribution. The faster the stirring is, the more irregular is the pattern.

The purpose of this chapter is to apply and verify the general results above in a concrete model of plankton dynamics in flows of geophysical relevance. In addition we compare structures appearing in closed and open flows, stressing the intermittent character of irregularities in the open flow case. We expect this result to apply also to other situations in atmospheric or oceanic chemistry.

The chapter is organized as follows: next Section summarizes the general theoretical results obtained in the former chapters. The particular plankton dynamics and the two different flows that are the subject of our study are presented in Sect. 4.3. They are variations of a kinematic model for a two-dimensional meandering jet, leading to a closed and to open flow model. Section 4.4 describes numerical results for the closed flow case, whereas

Sect. 4.5 considers the open flow. Finally, Sect. 4.6 contains our conclusions.

4.2 General results

The temporal evolution of reacting fields is determined by advection-reaction-diffusion equations. Advection because they are under the influence of a flow, reaction because we consider species interacting with themselves and/or with the carrying medium. Diffusion because turbulent or molecular random motion smoothes out the smallest scales. For the case of an incompressible velocity field $\mathbf{v}(\mathbf{r},t)$, the standard form of these equations is

$$\begin{aligned}\frac{\partial C_i(\mathbf{r},t)}{\partial t} \quad &+ \quad \mathbf{v}(\mathbf{r},t)\cdot\nabla C_i(\mathbf{r},t) = \\ & f_i(C_1,...,C_N,\mathbf{r}) + \nu\nabla^2 C_i(\mathbf{r},t), \end{aligned} \tag{4.1}$$

where $C_i(\mathbf{r},t)$, $i = 1,...N$, are interacting chemical or biological fields advected by the flow $\mathbf{v}(\mathbf{r},t)$, $f_i(C_1,...,C_N,\mathbf{r})$ are the functions accounting for the interaction of the fields (e.g. chemical reactions or predator-prey interactions). Diffusion effects are only important at small scales and we will neglect them in the following. In this limit of zero diffusion $\nu \to 0$ the above description can be recast in Lagrangian form:

$$\frac{d\hat{\mathbf{r}}}{dt} = \mathbf{v}(\hat{\mathbf{r}},t) \tag{4.2}$$

$$\frac{dC_i}{dt} = f_i\left(C_1,C_2,..,C_N,\mathbf{r}=\hat{\mathbf{r}}(t)\right),\ i=1,.,N, \tag{4.3}$$

where the second set of equations describes the chemical or population dynamics inside a fluid parcel that is being advected by the flow according to the first equation. In the absence of diffusion, a coupling between the flow and the chemical/biological evolution can only appear as a consequence of the spatial dependence of the $f_i(C_1,...,C_N,\mathbf{r})$ functions. This spatial dependence describes non-homogeneous sources or sinks for the chemical reactants or spatially non-homogeneous reaction or reproduction rates. Such inhomogeneities may arise naturally from a variety of processes such as localized upwelling, inhomogeneous solar irradiation, or river run-off, to name a few.

From now on, the incompressible flow $\mathbf{v}(\mathbf{r},t)$ will be assumed to be two-dimensional and time dependent. This situation generally leads to chaotic advection. For simplicity, our general arguments will be stated for the case in which $\mathbf{v}(\mathbf{r},t)$ satisfies the technical requirement of *hyperbolicity*, but in the examples less restrictive flows will be used. The most salient feature of advection by a chaotic flow is sensibility to initial conditions, that is, fluid particles initially close typically diverge in time at a rate given by the maximum Lyapunov exponent of the flow $\lambda_F > 0$:

$$|\delta\mathbf{r}(t)| \sim |\delta\mathbf{r}(0)|e^{\lambda_F t}\,. \tag{4.4}$$

Equation (4.4) is valid for nearly all the initial orientations of the initial particle separation $\delta\mathbf{r}(0)$. However, the incompressibility condition implies that there is a particular orientation of the initial separations $\delta\mathbf{r_c}(0)$ for which the two trajectories approach each other: $|\delta\mathbf{r}(t)| \sim |\delta\mathbf{r_c}(0)|e^{\lambda'_F t}$, with $\lambda'_F = -\lambda_F$.

The general class of chemical reactions studied in the preceding chapters was the one leading to stable local equilibrium in the absence of flow or, in terms of the chemical dynamical subsystem (4.3), the dynamics approaching a unique fixed point for each constant position $\mathbf{r}$. This means that there are not chemical instabilities nor chemical chaos, and that the concentrations tend to approach a value determined at each point by the sources in f_i. In the presence of advection by the flow $\mathbf{r} = \hat{\mathbf{r}}(t)$, the relaxation process is altered, but can be characterized by the value of the maximum Lyapunov exponent λ_C of the chemical subsystem (4.3), which we assume to remain negative.

In order to characterize the spatial structure of the C_i fields we calculate the difference

$$\delta C_i = C_i(\mathbf{r} + \delta\mathbf{r}, t) - C_i(\mathbf{r}, t) \quad . \tag{4.5}$$

Inserting this expression, for $|\delta\mathbf{r}|$ small enough, into the equation for the chemical dynamics as has been shown in the former chapters, we can obtain the evolution of the gradients of the chemical field at long times:

$$\begin{aligned} \nabla C_i(\mathbf{r}, t) \quad &\approx \quad \sum_{j=1}^{N} \nabla(C_j^0 \cdot \mathbf{V}_j^0)\mathbf{V}_i^0 e^{(\lambda_F + \lambda_C)t} \\ + \int_0^t ds \quad &\textstyle\sum_{j=1}^{N} \quad (\nabla f_j(\hat{\mathbf{r}}(s)) \cdot \mathbf{V}_j^s)\mathbf{V}_i^s e^{(\lambda_F + \lambda_C)(t-s)} \ , \end{aligned} \tag{4.6}$$

where the vectors $\mathbf{V}_i^t \equiv \mathbf{n}\left(\hat{\mathbf{r}}(t)\right) v_i$ are combinations of the vectors $\mathbf{n}(\mathbf{r})$ pointing at each point along the most contracting direction of the flow and of the vector $\{v_i, i = 1, ..., N\}$ associated to the contracting direction in the chemical subspace. $\hat{\mathbf{r}}(s)$ is the trajectory ending at $\mathbf{r}$ at time t. It is important to realize that Eq. (4.6) gives the long time behavior of ∇C_i correctly in all but in one direction. The directional derivative of C_i in the most expanding direction should be obtained with (4.6) but replacing λ_F by $\lambda'_F = -\lambda_F$, and the vectors $\mathbf{n}$ by the ones associated to the expanding direction.

The convergence of the gradients for $t \to \infty$ depends on the sign of the exponent $\lambda_F + \lambda_C$. There are two possibilities:

- If $\lambda_F + \lambda_C < 0$ then the convergence of the chemical dynamics towards local equilibrium is stronger than the effect of the chaotic flow on the fluid particles. Gradients are finite so that a smooth asymptotic distribution is attained by the chemical fields.

- If $\lambda_F + \lambda_C > 0$ then in the $t \to \infty$ limit the chemical pattern becomes *nowhere differentiable*. An irregular structure with fractal properties is developed. Remember however that at each point there is a direction for which $\lambda_F + \lambda_C$ should be substituted by $-\lambda_F + \lambda_C$, always negative, in (4.6). In this direction derivatives are finite and the field is smooth.

  Thus the resulting structure is *filamental*, i.e., irregular in all directions except in one along which it is smooth. This one corresponds to the direction of the filaments lying along the unstable foliation of the chaotic advection.

4.3 The plankton and the jet models

In the numerical investigations below we will consider a simple model of plankton dynamics immersed in a meandering jet flow.

This plankton model, used by [18] and related to the one used by [53], considers explicitly three trophic levels: the nutrient content of a water parcel, described in terms of its carrying capacity C (defined as the maximum phytoplankton content it can support in the absence of grazing), the phytoplankton biomass P, and the zooplankton Z. The Lagrangian 'chemical' subsystem (4.3) reads:

$$\frac{dC}{dt} = \alpha\left(C_0(\mathbf{r}) - C\right) \tag{4.7}$$

$$\frac{dP}{dt} = P\left(1 - \frac{P}{C}\right) - PZ \tag{4.8}$$

$$\frac{dZ}{dt} = PZ - \delta Z^2 \,. \tag{4.9}$$

All terms have been non dimensionalized to keep a minimal number of parameters. Equation (4.7) describes the relaxation of the carrying capacity, at a rate α, towards an inhomogeneous shape $C_0(\mathbf{r})$. This will be the only explicitly inhomogeneous term in the model, and describes a spatially dependent nutrient input, arising from some topography-determined upwelling distribution or latitude dependent illumination, for example. The first terms in Eq. (4.8) describe phytoplankton logistic growth, whereas the last one models predation by zooplankton. This effect gives also rise to the first term in (4.9). The term containing δ, the zooplankton mortality, describes zooplankton death produced by higher trophic levels. The only stable fixed point of model (4.7)-(4.9) is given by $C^* = C_0(\mathbf{r})$, $P^* = C_0\delta/(\delta + C_0)$, and $Z^* = P^*/\delta$.

The model flow will be given by the following streamfunction [49]:

$$\phi(x,y) = 1 - \tanh\left(\frac{y - B(t)\cos\left[k(x-ct)\right]}{\left(1 + k^2 B(t)^2 \sin^2\left[k(x-ct)\right]\right)^{\frac{1}{2}}}\right). \tag{4.10}$$

It describes a jet flowing eastwards, with meanders in the North-South direction. These meanders are also advected by the jet at a phase velocity c. $B(t)$ and k are the (properly adimensionalized) amplitude and wavenumber of the undulation in the streamfunction.

The motion of the tracer particles (the dynamical system (4.2)) is given by

$$\begin{aligned} \frac{dx}{dt} &= -\frac{\partial\phi}{\partial y} \\ \frac{dy}{dt} &= \frac{\partial\phi}{\partial x}. \end{aligned} \tag{4.11}$$

If the amplitude B of the meanders is time-independent, a simple change in the frame of reference renders the flow time-independent and Eq. (4.11) defines a non-chaotic integrable dynamical system. Chaotic advection appears in this model if B is made to vary in time, for example periodically:

$$B(t) = B_0 + \epsilon \cos(\omega t + \theta) \; . \tag{4.12}$$

Following [50], we use the parameter values $B_0 = 1.2, c = 0.12, k = 2\pi/L_x, L_x = 7.5, \omega = 0.4, \epsilon = 0.3$ and $\theta = \frac{\pi}{2}$. These values guarantee the existence of 'large scale chaos', i.e, the possibility that a test particle crosses the jet passing from North to South or viceversa. This is weaker than the requirement of hyperbolicity, but is enough to illustrate the general aspects of our theory.

The natural interpretation of the jet-flow just introduced is as an open flow: it advects most of the fluid particles from $x = -\infty$ towards $x = \infty$. We will localize the source term near the origin of coordinates (and for any value of the y coordinate):

$$C_0(x,y) = \begin{cases} 1 + A\sin(2\pi x/L_x)\sin(2\pi y/L_y) \\ \qquad \text{if} - L_x \leq x \leq L_x \\ \\ 0 \quad \text{elsewhere} \end{cases} \tag{4.13}$$

In this way, there is inhomogeneous nutrient input just near the origin, and capacity and plankton concentration in the fluid particles will decay as they are advected downstream.

A quite different class of natural flows are closed ones, e.g. recirculating flows in closed basins. Our jet model flow can be made closed simply by imposing periodic boundary conditions at the ends of the interval $-L_x < x < L_x$. Particles leaving the region through the right boundary are reinjected from the left. In this way nutrients are injected and extracted continuously from fluid elements as they traverse the different regions of the source

$$C_0(x,y) = 1 + A\sin(2\pi x/L_x)\sin(2\pi y/L_y). \tag{4.14}$$

This was the situation considered in chapters 2 and 3. We will see that different structures develop in the open and in the closed situation.

4.4 Closed flows

Numerically we proceed by integrating backwards in time Eq. (4.2) with initial coordinates on a rectangular grid (300×150) and then the chemical field for each point is obtained by integrating (4.3) forward in time along the fluid trajectories so generated.

Figure 4.1 shows a snapshot of the long-time phytoplankton distribution in the closed flow case for parameter values $\alpha = 0.25, \delta = 2.0, L_y = 4.$ and $A = 0.2$. In this case $\lambda_F + \lambda_C < 0$, therefore the distribution is smooth. A transect along the line $y = 0.8$ is also shown. Taking $\alpha = 0.025$, so that now $\lambda_F + \lambda_C > 0$ we obtain the distribution in Fig. 4.2. A complex filamental structure is clearly seen, in agreement with our theoretical arguments. The fractal nature of the pattern is also seen in the horizontal cut presented also in Fig. 4.2. A Hölder exponent of $|\lambda_C|/\lambda_F$ was predicted for these kind of transects. This implies plankton-variance power spectrum decaying as $k^{-\beta}$, with $\beta = 1 + 2|\lambda_C|/\lambda_F$. Thus β is in the range $]1,3]$ which agrees with field observations of plankton distributions [47].

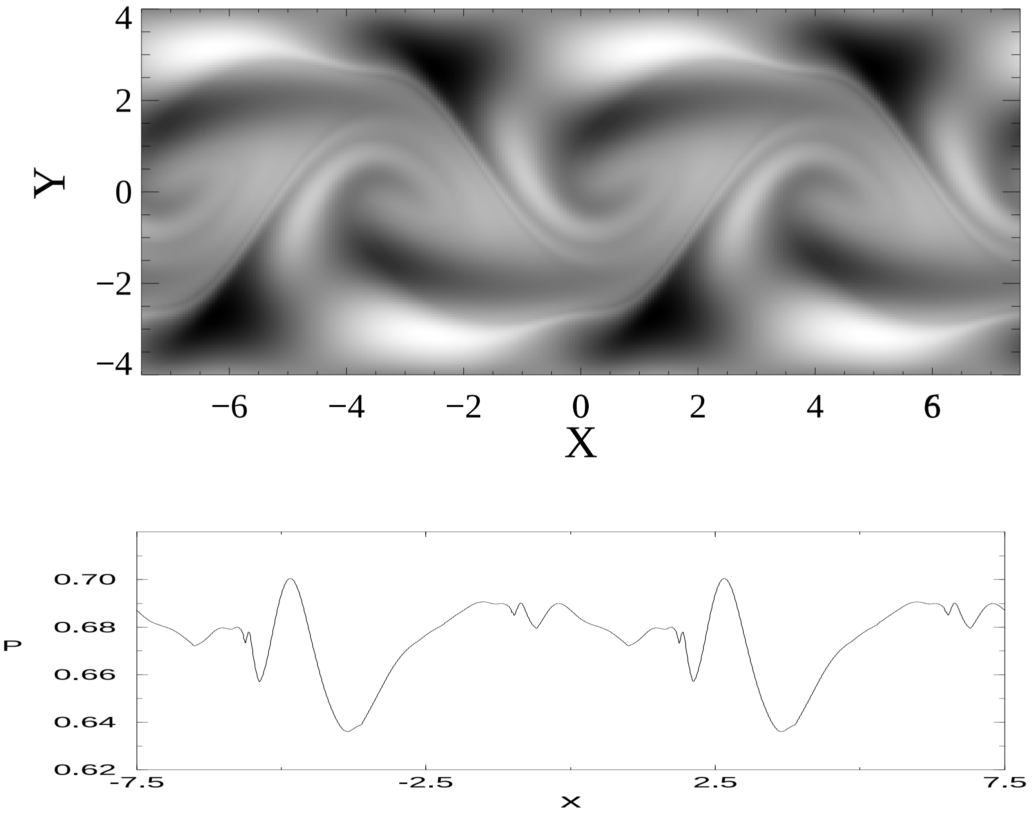

Figure 4.1: Phytoplankton smooth pattern in the closed flow, with an horizontal transect taken along $y = 0.8$

4.5 Open flows

Contrarily to closed flows, open flows are characterized by unbounded trajectories of fluid particles. Typical fluid particles enter and, after some time, leave the region of the nutrient source ($C_0(\mathbf{r}) > 0$). Thus, most fluid elements have only spent the most recent part of their trajectories inside the active region, with the rest of their evolution spent in regions with no spatial dependence of the nutrient input. For this part of the trajectory the gradient ∇f_j in Eq. (4.6) vanishes, implying that there would not be divergence of the gradients in the long-time limit.

It is well known from the study of chaotic advection in open flows [57], that while most of the particles spend only a finite amount of time in selected bounded regions of the flow, typically these regions contain also bounded orbits in which some of the particles can stay forever. Although the chaotic set formed by the bounded orbits is a fractal set of measure zero, particles visiting the vicinity of the stable manifold of this set can still spend arbitrarily

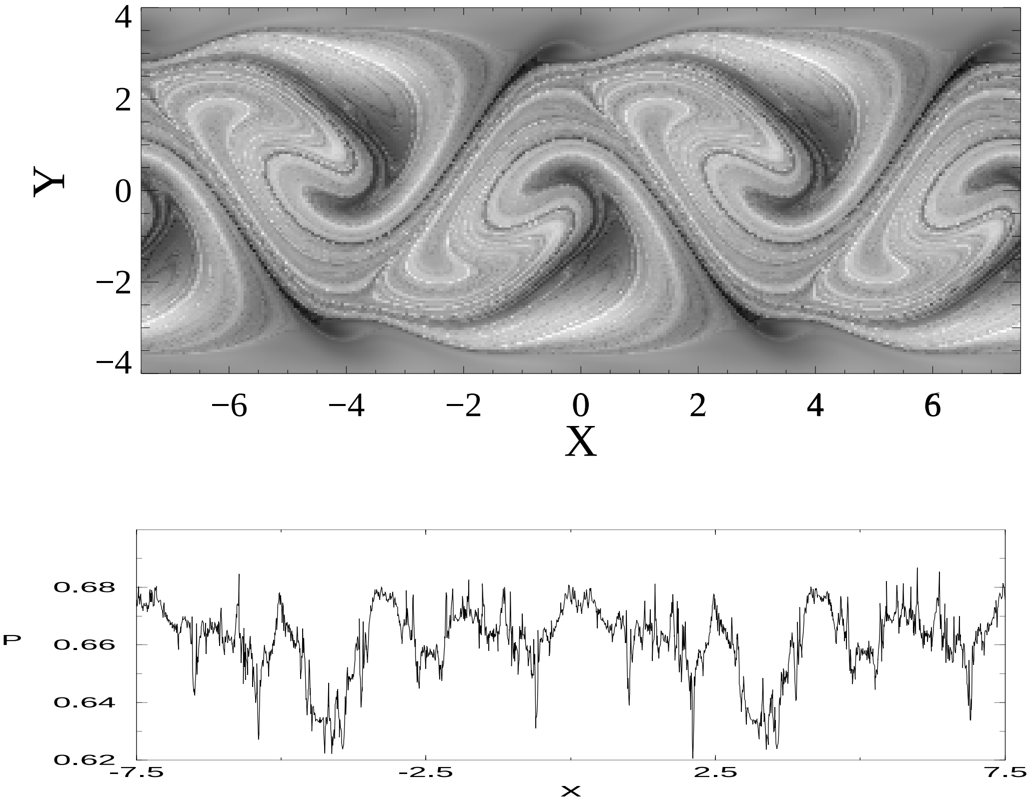

Figure 4.2: Phytoplankton filamental pattern in the closed flow, with a transect along $y = 0.8$

long time in the selected bounded region. This leads to the formation of characteristic fractal patterns in the advection dynamics even in the case of passive particles, as it was shown in numerical studies [23] and laboratory experiments of open flows [35].

For the particles that have spent infinitely long time in the source region, their chemical/biological evolution is equivalent to the one in a closed flow with the possibility of diverging gradients. The only difference is that now the values of λ_F and λ_C are those corresponding to the chaotic set of bounded orbits that never leave the biologically active region. The smooth-filamental transition observed in the previous Section for the closed flow will occur here only on this fractal set, which will always be surrounded by a smooth distribution. This results in a strongly intermittent character of the filamental field. Figure 4.3 shows a phytoplankton pattern for parameter values $\alpha = 0.025, \delta = 2.0$ and $A = 0.2$, and a transect crossing it, in the open-flow case. The inhomogeneity in the filamental structure is obvious, with singularities in a set recognized as the unstable manifold of the chaotic set formed by bounded orbits in the source region. Smooth structures are also obtained when $\lambda_F + \lambda_C < 0$. The proper description of the resulting structures should use the concept of multifractality, that is, inhomogeneous distribution of fractal properties. In fact, even in the closed flow case, at finite times the flow Lyapunov exponent λ_F would have space-dependent finite-time corrections, that will need to be taken into account in a proper generalization of (4.6). A quantitative description of these multifractal filamental structures has already been presented in the preceding chapters.

4.6 Conclusions

The spatial patterns formed by interacting populations under the influence of chaotic flows have been studied. In particular, we have considered a coupled model of ‘nutrient’, phytoplankton and zooplankton concentrations advected by two (open and closed) jet-like flows. General results have been reported for arbitrary chaotic flows, stressing the existence of a smooth-filamental transition depending on the relative strength of the maximum Lyapunov exponent of the flow and the one corresponding to the planktonic dynamical system. Patterns obtained for open and closed chaotic flows are different because of the transient or permanent character of the biological activity.

The models considered here are extreme simplifications of real biological and geophysical situations. We expect however that the main qualitative features found here, namely the possibility of finding smooth or filamental patterns depending on stirring and relaxation rates, and the increased inhomogeneities in open flows, to be present in more realistic chemical or biological transport situations.

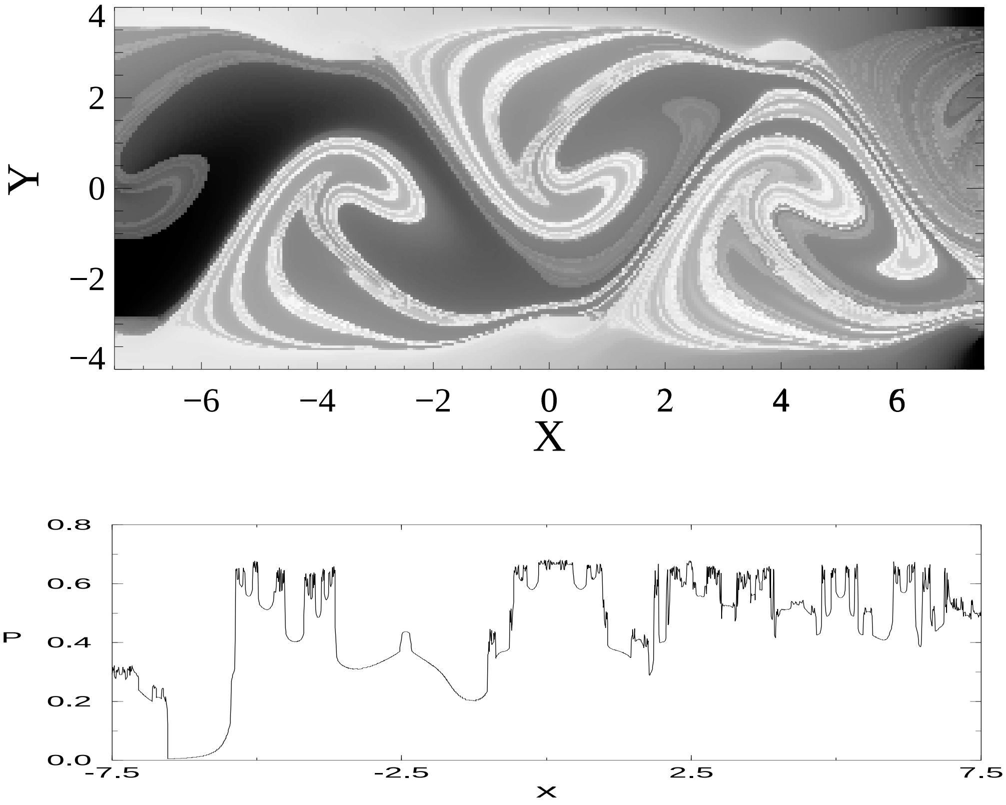

Figure 4.3: Phytoplankton filamental pattern in the open flow, with a transect along $y = 0.8$.

Chapter 5

Population dynamics advected by chaotic flows: a discrete-time map approach.

A discrete-time model of reacting evolving fields, transported by a bidimensional chaotic fluid flow, is studied. Our approach is based on the use of a Lagrangian scheme where fluid particles are advected by a $2d$ *symplectic map possibly yielding Lagrangian chaos. Each fluid particle carries concentrations of active substances which evolve according to its own reaction dynamics. This evolution is also modeled in terms of maps. Motivated by the question, of relevance in marine ecology, of how a localized distribution of nutrients or preys affects the spatial structure of predators transported by a fluid flow, we study a specific model in which the population dynamics is given by a logistic map with space-dependent coefficient, and advection is given by the standard map. Fractal and random patterns in the Eulerian spatial concentration of predators are obtained under different conditions. Exploiting the analogies of this coupled-map (advection plus reaction) system with a random map, some features of these patterns are discussed.*

5.1 Introduction

Patchiness, or the uneven distribution of substances of organisms, is ubiquitously observed in the ocean [18, 59, 58, 60]. In complex situations such as the marine ecosystems, characterized by the interplay of population dynamics and an ambient fluid motion which may differently affect individual populations, the question of how a localized availability of nutrients (or preys, or, in chemical terms, activators) may affect the distribution of primary producers (or predators, or inhibitors, respectively; in the following we refer to preys and predators) is a crucial and challenging problem.

According to [59], the possible causes originating patchiness in marine ecosystems may be grouped in different categories: fluid motion, biological growth coupled with dispersive processes, less ubiquitous mechanisms like swarming, vertical migration, and others. In addition to patchiness, localized availability of *food* may occur in correspondence of localized sub-ecosystems, such as Posidonia Oceanica beds (for a review see [61]): they display a quite complex structure in which the most important features arise from direct consumption of the plant and epiphyte-herbivore interactions, although a portion of the trophic chain is based on suspended matter [61].

A comprehensive description of such processes leads to the study of the so called advection-reaction-diffusion equations. These are partial differential equations of the type:

$$\frac{\partial C_i(\mathbf{x},t)}{\partial t} + (\mathbf{v}(\mathbf{x},t)\cdot\nabla)C_i = R_i(C_1,...,C_N,\mathbf{x},t) + D_i\triangle C_i. \tag{5.1}$$

Where $C_i(\mathbf{x},t)$ $(i = 1,...,N)$ is the concentration of the i-th reactive (in biological or chemical terms) species or substance, and the functions R_i describe the reaction, or the population, intrinsic dynamics. The possible explicit spatial and temporal dependence may model the influence of temporal and spatial inhomogeneities in food, temperature, etc. The term $(\mathbf{v}(\mathbf{x},t)\cdot\nabla)C_i$ represents advection by a given solenoidal (i.e. incompressible $\nabla\cdot\mathbf{v} = 0$) velocity field $\mathbf{v}(\mathbf{x},t)$. Finally, the term $D_i\triangle C_i$ describes diffusion of the i-th species or substance with diffusivity D_i. In writing (5.1) we are assuming that the evolution of the advected concentrations does not affect that of the underlying flow $\mathbf{v}(\mathbf{x},t)$. This is definitely reasonable at the scales we are interested in, even though it is worth mentioning that at much smaller scales the presence of organisms may affect the rheological properties of seawater [62, 63].

In some situations it would be necessary to consider a different velocity field for each of the N concentrations C_i. This may happen, for instance, if different organisms live at different mean depths, leading to differences in the experienced flow. In such cases one has to replace Eq. (5.1) by

$$\frac{\partial C_i(\mathbf{x},t)}{\partial t} + (\mathbf{v}_i(\mathbf{x},t)\cdot\nabla)C_i = R_i(C_1,...,C_N,\mathbf{x},t) + D_i\triangle C_i. \tag{5.2}$$

In this Chapter and in the rest of this Thesis, however, we will only consider the case given by Eq. (5.1) in which the same velocity field advects all the substances.

Introducing the Lagrangian time derivative $\frac{d}{dt} = \frac{\partial}{\partial t} + \mathbf{v}\cdot\nabla$, Eq. (5.1) can be written in the form

$$\frac{dC_i(\mathbf{x},t)}{dt} = R_i(C_1,...,C_N,t) + D_i\triangle C_i. \tag{5.3}$$

If diffusion is neglected, it is simple to write the $C_i(\mathbf{x},t)$ in terms of the solutions of the Lagrangian evolution equation

$$\frac{d\mathbf{x}(t)}{dt} = \mathbf{v}(\mathbf{x}(t),t), \tag{5.4}$$

and the reactive evolution equation

$$\frac{dC_i(t)}{dt} = R_i(C_1,...,C_N,\mathbf{x}(t),t). \tag{5.5}$$

This set of coupled ordinary differential equations describe the advection-reaction process in a Lagrangian frame: fluid particles move according to (5.4), and reactions among the C_i's occur inside each fluid particle, as expressed by (5.5), where $C_i(t)$ are the concentrations at a particular fluid particle (the one at $x(t)$ at time t, i.e. $C_i(t) \equiv C_i(\mathbf{x}(t),t)$). Denoting by S^t and L^t the formal solutions of (5.4) and (5.5) respectively (i.e., $\mathbf{x}(t) = S^t\mathbf{x}(0)$ and $\mathbf{C}(t) = L^t\mathbf{C}(0)$, with $\mathbf{C} = (C_1, C_2, ..., C_N)$) we can write the solution of Eq. (5.1) in the form (with $D_i = 0$)

$$\mathbf{C}(\mathbf{x},t) = L^t\mathbf{C}(S^{-t}\mathbf{x},0). \tag{5.6}$$

The case $D_i \neq 0$ needs a more elaborated treatment. In addition to the time dependence, L^t will have also an explicit space dependence if the R_i's have it.

Obviously, the detailed understanding of the above class of partial differential equations constitute a formidable task. However, at this stage of development, we are just interested in the search for generic behaviors expected when few typical characteristics of the flow and of the population dynamics are considered. Thus, if, for example, we concentrate on flows of geophysical nature, horizontal motion turns out to be much more intense than vertical one as soon as one considers scales larger than a few kilometers. This justifies restricting in the following to incompressible twodimensional flows. A turbulent bidimensional flow would be a way to model the irregular advection process to which suspended matter is subjected in real oceans. There are however simpler classes of flows which share some basic characteristics with turbulence, but are much more accessible to analysis: Lagrangian chaotic flows [6, 5]. These are smooth velocity fields, with some simple time dependence in the Eulerian description, but which lead to chaotic trajectories of fluid elements, with the associated stretching and folding, in the Lagrangian description. In this restricted framework, it is well known that even periodic time-dependence in two-dimensional incompressible flows leads generically to chaotic motion of fluid particles.

Rather than integrating the full equations describing the continuous in time dynamics, and since our interest lies mainly in a qualitative characterization of the population system, we will resort in this Chapter to a discrete in time mapping-approach in terms of discrete-time dynamical systems. This approach is numerically very efficient, and has proven to be extremely productive to study the impact of chaotic advection on mixing [6, 5, 64]. The main idea is to mimic the advection and reaction processes in terms of maps that capture the main features of each aspect. Thus, since we will be looking at processes taking place in 2d incompressible flows, the advective part of our model is naturally described by a twodimensional symplectic map. It is well known that Lagrangian motion in such systems is typically chaotic and with a rather rich behavior. In addition, the transported fluid parcel contains concentrations of active chemical substances or biological specimens subjected to a specific dynamics that will be also modeled in terms of a map. Also, it is worth noticing that even though this is not done in this work, diffusion can be easily reincorporated into the model by averaging, after each iteration of the maps, the concentration of the different species contained in the fluid elements over a region of size $l \sim \sqrt{D_i \tau}$, where D_i is the corresponding diffusivity and τ is a characteristic time scale of the system.

The general ideas and formalism sketched above will be made more concrete in the following, and applied to tackle our main problem: the *influence of inhomogeneities of the distribution of preys on that of predators*. We will make use of some known results for random maps, and compare our discrete-time approach with results obtained in the continuous-time description of the problem presented in the Chapters 2 and 3 of this Thesis. In Section II we will discuss the approach to population dynamics in terms of maps; in Section III our particular model is presented and compared with results for a random logistic map; the analogy helps in the interpretation of the resulting spatial structure of predators, which is described in Section IV, and discussed in Section V.

5.2 A discrete-time approach

Let us now present the general idea of our approach for the analysis of the population dynamics in terms of maps.

It is easy to understand that for time-periodic velocity fields, i.e. $\mathbf{v}(\mathbf{x}, t) = \mathbf{v}(\mathbf{x}, t+T)$ where T is the period, Eq (5.4) can be described by a discrete-time dynamical system. The position $\mathbf{x}(t+T)$ is univocally determined by $\mathbf{x}(t)$. In addition (because of the periodic velocity field) the map $\mathbf{x}(t) \to \mathbf{x}(t+T)$ cannot depend on t. Since a periodic time dependence is enough to induce Lagrangian chaos, and because of the above mathematical simplifications, we particularize our study to time-periodic velocity fields, for which we can write

$$\mathbf{x}(t+1) = \mathbf{F}(\mathbf{x}(t)), \tag{5.7}$$

Now, time is measured in units of the period T. If $\mathbf{v}$ is incompressible, the map (5.7) is volume (area in $2d$) preserving, i.e., $\left|\det(\frac{\partial F_i}{\partial x_j})\right| = 1$. In $2d$ the map (5.7) is symplectic, i.e. the discrete-time version of a Hamiltonian system. Usually, it is not simple at all to obtain $\mathbf{F}(\mathbf{x}(t))$ for a given $\mathbf{v}(\mathbf{x}, t)$. However, one can directly write models for $\mathbf{F}$ which contain the qualitative features of the flow one is trying to model.

In addition, the transported fluid parcel contains species subjected to their own population dynamics. Denoting the solution of (5.5) after one period of the flow (L^T) by $\mathbf{G}$, the evolution rule for the interacting concentrations $\mathbf{C} = (C_1, C_2, ...C_n)$ is expressed in terms of a map:

$$\mathbf{C}(t+1) = \mathbf{G}(\mathbf{C}(t)) \tag{5.8}$$

As before, $\mathbf{G}$ will carry additional explicit time and space dependencies if (5.5) is not autonomous in space or time. The discrete-time version of Eq. (5.6) is:

$$\mathbf{C}(\mathbf{F}(\mathbf{x}), t+1) = \mathbf{G}(\mathbf{C}(\mathbf{x}, t)). \tag{5.9}$$

In the following we particularize this general approach to a particular model.

5.3 A particular model and its relationship with a random logistic map

The main interest of our study is to consider the problem of how the spatial structure of the prey spatial distribution may affect the one of the predators. In this section we study a particular model and present its analogies with the random map. This will enable us to use the already known properties of this random map to get a further insight into the influence of the distribution of preys on the predator patterns. We will consider a single-species population dynamics, i.e. the predator evolves for fixed prey distribution, and under the influence of the flow, but the distribution of the prey is a non-dynamic variable, in the sense that it is not transported by the flow and is maintained at fixed values undisturbed by the predator action. This is the simplest setting in which the effects of a localized source of nutrients on an advected predator will show up.

The model is the following: the positions of the *fluid parcels* are advected by a standard map [8], i.e. a 2d symplectic map defined in the square of side 2π by

$$x(t+1) = (x(t) + K \sin y(t+1)) \bmod 2\pi \tag{5.10}$$

$$y(t+1) = (y(t) + x(t)) \bmod 2\pi. \tag{5.11}$$

It is not integrable for $K \neq 0$. As K increases chaotic regions occupy larger areas, and the original KAM tori (regular non-chaotic orbits) are successively destroyed (see Fig. 1.1 in the first Chapter). For K large enough the KAM tori occupy a very small region and practically the whole phase space is a unique chaotic region.

The model is completed by stating the evolution rules for the predator-prey interactions. We denote with $n(\mathbf{x})$ the stationary spatially inhomogenous distribution of preys, and with $C(\mathbf{x}, t)$ the concentration of predators in point $\mathbf{x}$ at time t. We take it to evolve in each fluid parcel according to the well known logistic map: $C(t+1) = G(C) = rC(t)(1 - C(t))$, but with a growth rate parameter r determined by the presence of preys, i.e., $r = \mu n$. The complete evolution equation (5.9) is

$$C(\mathbf{F}(\mathbf{x}), t+1) = \mu n(\mathbf{x}) C(\mathbf{x}, t)(1 - C(\mathbf{x}, t)). \tag{5.12}$$

The standard map has been written in the compact form (5.7) with $\mathbf{x} = (x, y)$.

We now introduce the particular form of the localized prey distribution $n(\mathbf{x})$:

$$r = \mu n(\mathbf{x}) = \begin{cases} r_1 & if\ x \in [\pi(1-p), \pi(1+p)],\ \forall y \\ r_0 & otherwise. \end{cases} \tag{5.13}$$

with $0 \leq p \leq 1$. We are suggesting a striped spatial distribution of the preys (with strip width $2\pi p$), which basically represents (due to the 2π-periodicity of the flow) the simplest, space-periodic fashion to mimic a patchy distribution. A fraction p of system area has the value $r = r_1$, and fraction $1 - p$, the $r = r_0$. The heuristic idea that will guide our analysis is that, if mixing provided by the advection map is strong enough, fluid parcels will visit regions with the different values of r in a stochastic way, so that the Lagrangian evolution of the concentrations will be well described by a random logistic map, i.e. a map of the form

$$C(t+1) = a_t C(t) \left(1 - C(t)\right), \tag{5.14}$$

where the random variable a_t can take only two values

$$a_t = \begin{cases} r_0 & with\, probability\; 1-p, \\ r_1 & with\, probability\; p, \end{cases} \tag{5.15}$$

and a_{t+1} is independent of any previous a_t.

The random map (5.14) has been studied in [65] for $r_0 = 1/2$ and $r_1 = 4$. This corresponds to the situation in which for a value of $r = r_0$ the population dynamics is attracted by a fixed point, whereas chaotic population dynamics occurs for $r = r_1$. The alternancy in time of these two tendencies gives rise to nontrivial behavior. Numerical (and some analytical) computations [65] give the following results for (5.14) with $r_0 = 1/2$ and $r_1 = 4$, for different values of p:

i) If $p \leq p_1 = 1/3$ the Lyapunov exponent $\lambda = \lim_{N\to\infty} \frac{1}{N} \sum_{i=0}^{N-1} \ln |a_t\,(1-2C(t))|$ is negative, i.e. there is exponential convergence of two initially close sequences $C(t)$ generated with the same sequence a_t but slightly different initial conditions $C(0)$. In this case, the sequences are attracted by $C = 0$.

ii) If $p_1 \leq p \leq p_2 \simeq 0.5$ the Lyapunov exponent is negative again, but now the sequences do not converge to any fixed point. They wander in an irregular and seemingly chaotic manner (of the *on-off intermittency* type). The meaning of the negative value of λ is that close initial values of C evolve, under the same sequence a_t, towards the same irregular trajectory. This is a case of chaotic synchronization related to the phenomenon of synchronization by noise [66, 67].

iii) If $p \geq p_2$ the Lyapunov exponent is positive, i.e. there is exponential divergence of two initially close sequences $C(t)$, behaving both chaotically.

As a first check confirming that our advection-population dynamics model is close to the random map when mixing is strong, we fix $r_0 = 1/2$ and $r_1 = 4$, as in [65]. This describes a system in which predators are advected over regions in which not enough food is available ($r_0 = 1/2$ leads to population extinction) and over the strip-like regions in which preys are abundant (leading to chaotic population dynamics of the predators). We iterate (5.12) to obtain $C(i) \equiv C(\mathbf{x}(i), i)$, and then calculate the reaction Lyapunov exponent λ^R for our system:

$$\lambda^R = \lim_{N\to\infty} \frac{1}{N} \sum_{i=0}^{N-1} \ln |G'\,(C(i))| = \lim_{N\to\infty} \frac{1}{N} \sum_{i=0}^{N-1} \ln |\mu n\,(\mathbf{x}(i))\,(1-2C(i))|\,, \tag{5.16}$$

The initial condition $C(\mathbf{x}, 0)$ was a smooth function proportional to $\sin(x)\sin(y)$. λ^R measures the rate of convergence or divergence of two initially similar concentration values C at the same fluid particle. In Fig. 5.1 we show λ^R as a function of p for different values of K. When K is increased above a high enough value (e.g. $K \approx 9$, for which the standard map shows a unique ergodic chaotic region [8]), λ^R approaches the Lyapunov exponent λ of the random map [65]. On the other side, when K is small, this correspondence is lost.

Therefore, exploiting this equivalence we can study different regimes of our system depending on the value of the parameter p. In particular, the spatial patterns of the advected field are strongly dependent of the value of λ^R. Next section is dedicated to the study of these structures.

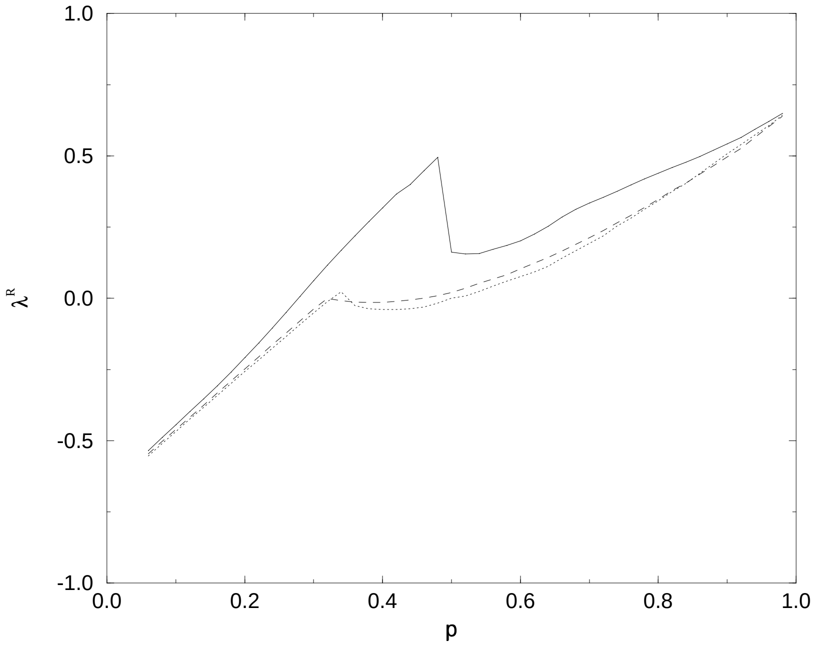

Figure 5.1: Reaction Lyapunov exponent, λ^R, calculated for different values of K. Solid line corresponds to $K = 1.5$, dotted line to $K = 9$ and dashed line to $K = 19$.

5.4 Predator spatial structures

The three regimes described above for the random map are also found for the behavior of the Lyapunov exponent λ^R as a function of p in our advection model, with just some minor quantitative differences, e.g. in the values of p_1 and p_2 (in particular, in most of our calculations we take $K = 9$, which gives $p_1 \simeq 0.34$ and $p_2 \simeq 0.48$). These three regimes give rise to the following different predator spatial structures:

i) For $p \leq p_1$, the concentration of predators vanishes in all the space. The nutrient area is too small to support a stable population.

ii) If $p_1 \leq p \leq p_2$, a typical spatial pattern appears. A relatively high, but very intermittent, concentration of predators appears in the area occupied by preys. Moreover, the concentration pattern displays fractal features.

iii) If $p \geq p_2$, the spatial concentration of predators shows a random pattern. No typical structure seems to emerge.

Whereas the result for case i) is self-evident, cases ii) and iii) need a more elaborated study. We proceed in the following subsections.

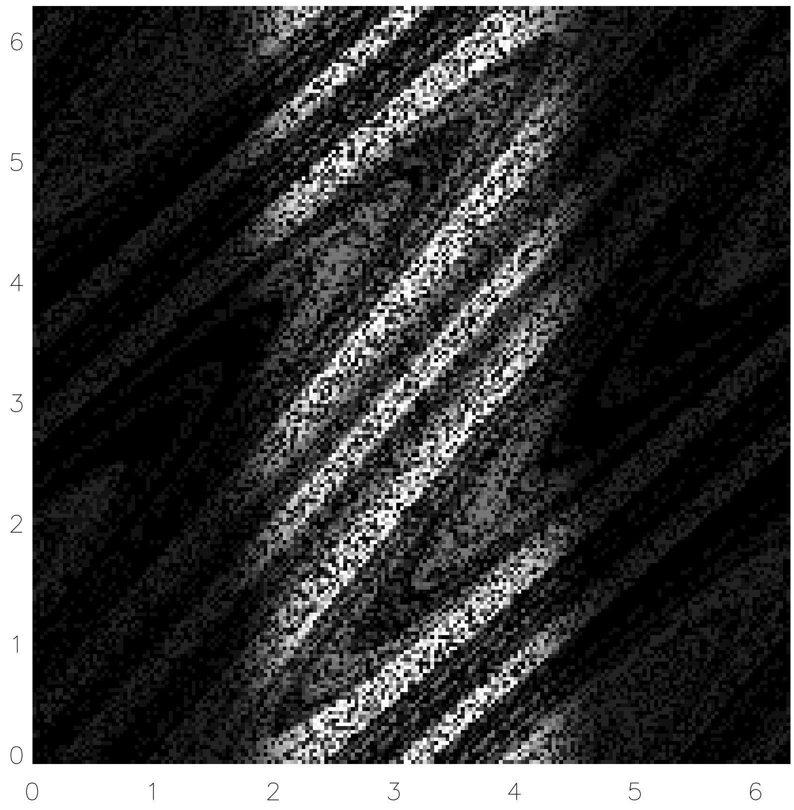

Figure 5.2: Predator 2d pattern obtained for $p = 0.37$. The distribution of nutrients is continuous. The lighter the colour the higher the concentration.

5.4.1 Case $p_1 \leq p \leq p_2$

The regime which we have labeled above with ii) is characterized by a negative reaction Lyapunov exponent λ^R. In this case, we observe numerically (see Fig. 5.2) the existence of a typical structure of the reactive field, which follows the strip-like structure of the preys. Moreover, a fractal pattern seems to be displayed by the distribution. Let us proceed to a quantitative characterization of these features.

In Chapters 2 and 3 of this Thesis we have studied the general continuous-time case of a chemically or biologically decaying field (thus with a negative reaction Lyapunov exponent) advected by a chaotic 2d flow. Since periodic velocity fields are used, it is straightforward to apply the results in these Chapters to the present case with discrete time. Nevertheless, a fundamental assumption in these studies is that a source term in the equations, analogous to our prey distribution, is a smooth function of space. The quantitative results of Chapters 2 and 3 would fail (see e.g. Eq. (2.10) in Chapter 2) when discontinuities are present in the source, as in the localized prey distribution of this present Chapter (5.13). Therefore, in our calculations, and with the view on characterizing the spatial patterns, we will use a continuous approximation to the previous step function describing the distribution of nutrients, which would allow us to compare our results (in the regime of

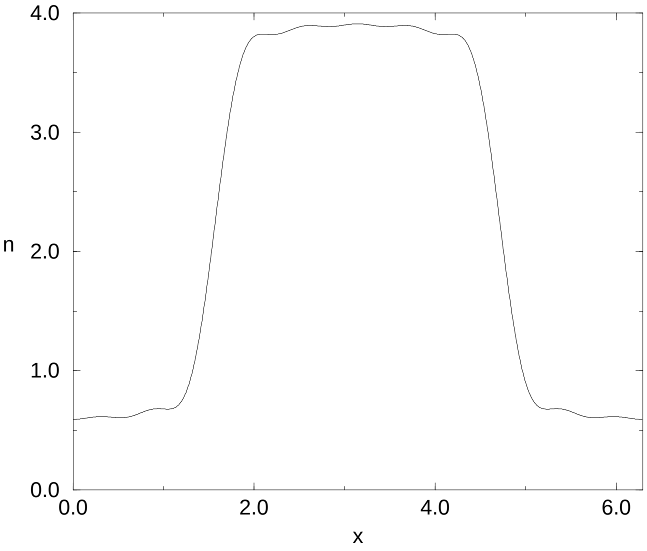

Figure 5.3: Onedimensional cut of the continuous distribution of nutrients.

$\lambda^R < 0$) with those in Chapters 2 and 3. The approximation is performed by truncating the Fourier transform of the step function of width p (Eq. (5.13)) and smoothing properly the coefficients [68]. The final expression we use is:

$$n(x,y) = \frac{1}{2\pi}\left(\pi + \frac{7p}{2}\right) + \sum_{k=-N,k\neq 0}^{N}\left(1 - \frac{|k|}{N+1}\right)(-1)^k \frac{7}{2\pi k}\sin\left(\frac{kp}{2}\right)\cos(kx), \quad (5.17)$$

for any $0 \leq x, y \leq 2\pi$ and $N = 10$. Fig. (5.3) shows a $1d$ cut of this smoothed distribution of nutrients.

A quantitative characterization of the observed structures can be performed in terms of structure functions. In particular, the structure function of order one, S_1, is defined by:

$$S_1(\delta\mathbf{x}) = \langle |C(\mathbf{x}+\delta\mathbf{x}) - C(\mathbf{x})| \rangle\,, \quad (5.18)$$

where $< ... >$ indicates an average taken over the different spatial points $\mathbf{x}$ along a line in the system. In Chapter 3 the scaling of S_1 is calculated with the result $S_1(\delta\mathbf{x}) \sim |\delta\mathbf{x}|^\alpha$ when $\delta\mathbf{x} \to 0$, with $\alpha \approx \frac{|\lambda^R|}{\lambda^F}$ when $\lambda^R < 0$ and $\lambda^F > |\lambda^R|$, being λ^F the Lyapunov exponent of the Lagrangian motion (5.4). The above expression for α is just an approximation to which multifractal corrections should be in principle added, but we are not going to consider them here.

The Lyapunov exponent of the standard map, for K high enough, is given [8] by: $\lambda^F \simeq \ln(K/2)$. In our calculations for $K = 9$ we are in the above mentioned conditions, that is, $\lambda^F > |\lambda^R|$ for all the values of p.

Fig. (5.4) shows $|\lambda^R|$ as a function of p for $K = 9$ (the smooth approximation to the spatial distribution of preys is used). In addition, we have numerically calculated the

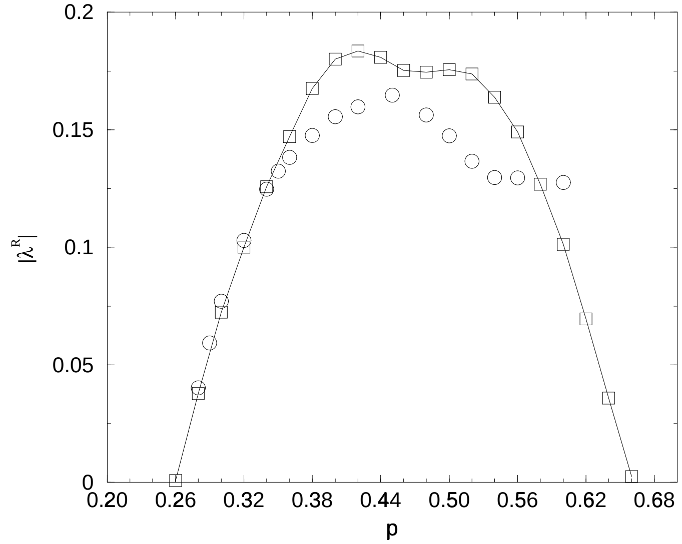

Figure 5.4: $|\lambda^R|$ for a continuous distribution of nutrients, calculated in two different ways against p. Values labeled with squares come from a direct calculation using expression (5.16) in the text. Circles are calculated from $|\lambda^R| \approx \alpha\lambda^F$, being α the numerically calculated scaling exponent of the first order structure function.

scaling exponent α of S_1 in lines across the central strip of nutrients, and multiplied it by $\ln(9/2) \approx \lambda^F$ for different values of p. The agreement between both quantities is quite good for p near p_1, confirming the expression $\alpha \approx \frac{|\lambda^R|}{\lambda^F}$, although it gets worse as $p \to p_2$. The reason for this are the already mentioned multifractal corrections to the scaling exponent of the structure function, but a deeper discussion about this needs a subsequent work. The agreement allows us to understand the pattern displayed in Fig. (5.2) in terms of the filamental fractal patterns discussed in the Chapters 2 and 3 for continuous-time dynamics. The observed fractal structures are revealing the stable and unstable manifolds (local contracting and expanding directions) attached to each point of the phase space of the standard map. It should be noted however that there is here a much larger amount of irregularities at small scales than in the patterns analyzed in Chapters 2 and 3. The reason is the much more irregular dynamics associated to the logistic map considered here. The Lagrangian evolution of $C(t) \equiv C(\mathbf{x}(t), t)$ is related to the one of the logistic random map, which is of the *on-off intermittency* type. Models considered in Chapters 2 and 3 displayed simple local relaxation behavior. The small-scale structure seen in Fig. 5.2 will introduce stronger multifractal corrections in higher order structure functions. We finally remark that when a discontinuous distribution of preys such as (5.13) is considered, the relationship $\alpha \approx \frac{|\lambda^R|}{\lambda^F}$ is not satisfied at all.

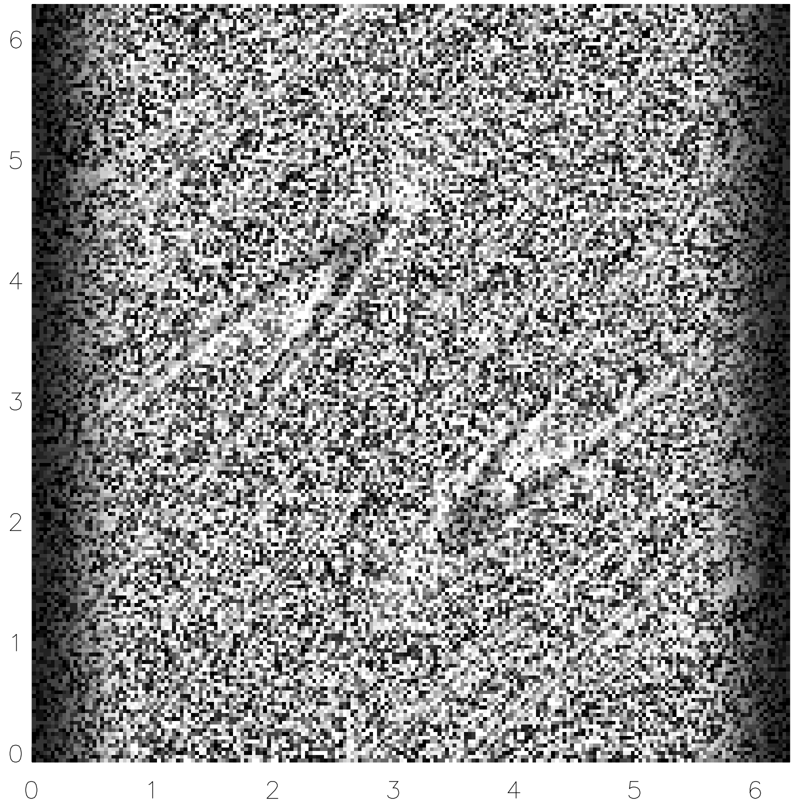

Figure 5.5: Predator 2d pattern obtained for $p = 0.87$. The distribution of nutrients is continuous.

5.4.2 Case $p > p_2$

Now we proceed to study the case $p > p_2$. In this regime, the reaction Lyapunov exponent λ^R is positive, i.e. the chemical or biological part of our system is also chaotic.

The patterns calculated in this regime have random appearance, being dominated by strong small-scale irregularity with very small amount of structure (see Fig. 5.5). In fact, the scaling exponents of the first-order structure function are close to zero, as corresponding to a random discontinuous field.

This random structure is easy to understand once one has realized that $\lambda^R > 0$ in this range of p: neighboring sites, even if they have initially nearly similar concentration values, and even when they remain close for long time so that they experience close values of the sequence $\mathbf{x}(t)$, will unavoidably develop growing differences in concentration values, thus leading to the observed discontinuities at small scales.

5.5 Discussion

Summing up, spatial structures with fractal features (of filamental type) appear for the predator field in a range of values of the size of the nutrient patch p. An increasing amount of small-scale randomness appears when p is increased, until structure is finally lost. The analogy with the random map model has allowed us to understand this behavior as being originated by the change in the value of the reaction Lyapunov exponent λ^R when p is varied. In particular, structure is lost when λ^R becomes positive. For p small enough, global extinction occurs, since most of the system has a parameter value for which $C = 0$ is the only attractor.

Our results have been obtained for a particular set of coupled maps, and for a specific nutrient distribution. We do not expect major qualitative changes in the above findings if the standard map is replaced by a different advecting flow, as long as the Lyapunov exponent λ^F takes the same value. This belief is supported by the more detailed arguments of Chapters 2 and 3 for the time-continuous case. It should be said however that the quantitative strength of multifractal corrections to simple expression such as $\alpha \approx \frac{|\lambda^R|}{\lambda^F}$ will depend on the particular flow chosen.

Our choice of the logistic map as the population dynamics to study is certainly important for the results obtained. Our results should describe the behavior under other population models as long as their parameters take values favoring chaotic oscillations in a localized portion of space, and favoring relaxation to a fixed point in the rest. The election of the logistic map has allowed the use of results known for random logistic maps, thus helping to interpret the different patterns in terms of the value of λ^R and its relationship with λ^F. Those quantities would be the right tool for the interpretation of advection-reaction patterns in other population or chemical models.

Diffusion has been discarded in the present work. We expect that its only effect would be to smooth out any small-scale fractal or random structure below a size of the order of $\sqrt{D/\lambda^F}$. In fact, our numerical calculations have an *effective diffusion* which comes from our minimal spatial resolution. As mentioned above, a more controlled way to introduce diffusion is to perform explicitly, after each map operation, an average of the concentrations of fluid particles closer than the diffusion length.

We finally mention that the map approach turns out to be an extremely efficient method from the numerical point of view, as compared to direct solution of partial differential equations such as (5.1) or other continuous approaches.

Chapter 6

Low-dimensional dynamical system model for observed coherent structures in ocean satellite data

The dynamics of coherent structures present in real-world environmental data is analyzed. The method developed in this Chapter combines the power of the Proper Orthogonal Decomposition (POD) technique to identify these coherent structures in experimental data sets, and its optimality in providing Galerkin basis for projecting and reducing complex dynamical models. The POD basis used is the one obtained from the experimental data. We apply the procedure to analyze coherent structures in an oceanic setting, the ones arising from instabilities of the Algerian current, in the western Mediterranean Sea. Data are from satellite altimetry providing Sea Surface Height, and the dynamical model is a two-layer quasigeostrophic system. A four-dimensional dynamical system is obtained that correctly describe the observed coherent structures (moving eddies). Finally, a bifurcation analysis is performed on the reduced model.

6.1 Introduction

In the last decades the study of turbulent or extended chaotic systems has enjoyed important advances. Two of them are, first, the recognition of the existence and high relevance of coherent structures (defined as strongly *persistent* spatiotemporal structures in the dynamical evolution of the system) in weakly and even strongly chaotic systems, and, second, the borrowing of mathematical methods coming from the studies of nonlinear dynamical systems (see [10] and references therein).

In both subjects, the introduction of the statistical technique known as the Proper Orthogonal Decomposition (POD, also known under a variety of other names, such as Karhunen-Loève decomposition, method of Empirical Orthogonal Eigenfunctions, etc.) has played an important rôle. It was introduced in the context of turbulence by Lumley [69] and has revealed itself as an efficient technique for finding, describing and modeling coherent structures in turbulent fluids or extended chaotic systems. The purpose of POD is to separate a given data set into orthogonal spatial and temporal modes which most efficiently absorb the variability of the data set.

The power of POD has been implemented following two different paths [10]: On the one hand the POD is used as a standard technique to extract coherent structures from empirical data sets [70, 71]. Contrasting to Fourier Decomposition, the eigenfunctions obtained from the POD may display spatial localization, and thus provide a more efficient way to represent coherent structures. The use of empirical information can be pushed further and methodologies from dynamical systems theory and other fields have been used in the POD framework, to provide useful algorithms for control [72] and prediction (see the last two Chapters of this Thesis). On the other hand, the POD eigenfunctions provide a set of basis functions which is optimum (at least in a well defined linear sense) for obtaining low-dimensional ordinary differential equation (ODE) approximations starting from models based on partial differential equations (PDEs). The approximation is performed by obtaining long runs of the PDEs, performing the POD onto this synthetic data set, and using the Galerkin method to project the PDE model into the so obtained POD eigenfunctions [100, 73, 74].

These two potentialities, i.e. the ability to extract empirical information from experimental data, and the efficiency in building low-dimensional projections from models, are not frequently used together in the literature. A remarkable exception is the use of empirical eigenfunctions obtained from the POD of experimental data from a turbulent boundary layer to build a low-dimensional approximation to the Navier-Stokes equations [75, 76]. We believe that, in some circumstances, the projection of theoretical models into experimentally obtained empirical functions could improve both the model and the data. This will occur in situations such as in the modeling of natural phenomena (ocean or atmospheric dynamics, for example) where even very complex models may be not accurate enough, and data are unvoidably noisy and difficult to calibrate. Projecting the model onto the experimental eigenfunctions will force it to stay into the 'right' subspace, providing a kind of data assimilation [77] that may compensate the loss of details inherent to low-dimensional projections. On the other hand, the truncation involved in the POD method implies a kind of filtering providing noise reduction to the data set.

Our aim in this Chapter is to explore the synergy between experimental observation and low-dimensional reduction via POD, in the complex setting of environmental fluid dynamics. In particular, a model for coherent structures arising from instabilities of the Algerian current in the Mediterranean Sea will be set up and analyzed.

In the ocean dynamics context, the kind of spatiotemporal data sets we need for our purposes can only be obtained from satellite observations. The recent availability of satellite data of the sea surface is allowing a deeper understanding of the ocean. Satellites continuously measure sea temperature, sea level, chlorophyll concentration, etc., which increase our knowledge of ocean currents, mean sea level changes, tides, or plankton dynamics, to name a few. In particular, in the last decade the ERS and the TOPEX/POSEIDON (T/P) satellite missions have provided the scientific community with high-accuracy altimetry data, which determines the sea surface level, this is, the height of the sea surface over a reference level on Earth. Among other relevant scientific applications, these type of data are specially useful for a better understanding of the dynamics of mesoscale phenomena in the ocean. Mesoscale refers to typical spatial scales of 30 to 300 kilometers and time scales of less than one year, and it is associated with movements of oceanic currents and short-time flow variations, and also with the formation and propagation of ocean eddies. These eddies are generated by interactions with the oceanic topography and/or mean flow instabilities and their importance is enormous: for example they play a fundamental role in the heat transport from low to high latitudes.

Some details of the results we present here are determined by the peculiarities of the data set we are going to use. In particular we mainly focus in the motion of a vortex which is present in the data, but is only described by subdominant eigenfunctions in the POD results. This lead us to a model for this coherent structure, but we do not try to model the full dynamics of whole data set. We expect however that our general methodology will be useful in other problems in which real-world noisy observations and complex but imperfect PDE models are available. Generalizations of the POD method which take into account in a more consistent way dynamic constraints have been developed [78, 79, 12] and even applied to geophysical contexts [81, 78, 80]. We will use however, and just for simplicity, the standard formulation of the POD technique.

The Chapter is organized as follows: in the next section, we describe the data set. In section III, these data are analyzed with the Proper Orthogonal Decomposition (POD). The study of the most relevant of the eigenfunctions allows the identification of a coherent structure, that is, a moving vortex or eddy. Then, in the following section, the associated temporal modes of the POD eigenfunctions defining the eddy are projected over a hydrodynamic model which, finally, provides a deterministic dynamical system depending on the parameters of the model. In section V, the reconstruction of the moving vortex from the dynamical system model is performed. Next, in section VI the bifurcation analysis of the dynamical system is shown. Section VII concludes this work.

6.2 Satellite altimetry data

We analyze altimetry data from the T/P and ERS-1 satellite missions [82]. Altimetry data of the ocean provide the Sea Surface Height (SSH) over a reference substrate. The data obtained in both missions have been merged (to obtain a better spatiotemporal resolution)

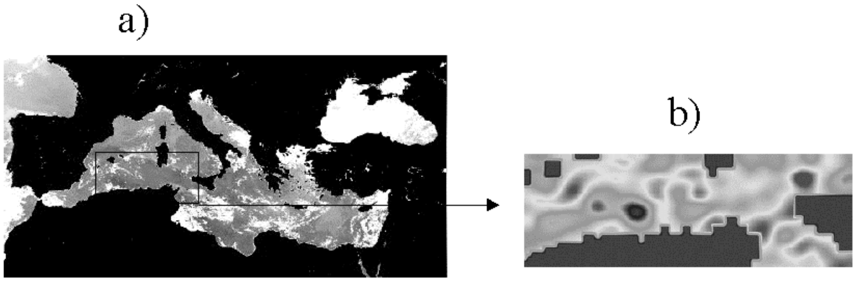

Figure 6.1: a) A map of the Mediterranean Sea. In the small box we show the area under study. b) Shows one of the altimetry images obtained from the satellite.

on a common time period, from October 1992 to December 1993 and, finally, 44 maps taken every 10 days on a 0.2^o regular grid are obtained for the Western Mediterranean Sea [83]. We restrict our analysis to the area known as the Algerian Current, localized between $0 - 15^oE$ and $35 - 40^oN$, where a strong mesoscale activity is observed [85]. A mean flow moving eastwards and parallel to the coast of Algeria is the main feature in this area. It undergoes instabilities that shed vortices into the western Mediterranean basin, greatly influencing the physical and biological processes in this area of the Sea [84]. In Figure 1 a) we show a map of the Mediterranean Sea, and in the small box the area under study. Figure 1 b) shows one of the 44 maps that we are going to analyse.

The SSH fields allow the identification of coherent structures (structures approximately maintained in the flow over long time periods) in geophysical flows. In particular, areas of higher altimetric values may correspond to anticyclonic (clock-wise) vortices and lower ones may indicate the existence of cyclonic (anticlock-wise) vortices. Actually, the data we have used are referred to a mean level, i.e., we analyze Sea Level Anomalies (SLA) where the reference height is the temporal mean of the data. This may give rise to some minor problems because to obtaining the SSH data (the one we are going to need in our modeling approach) is not as simple as adding the mean sea level. This is because of the different resolution in the data and will be explained in detail in section IV.

6.3 POD analysis of the satellite data

As it has already been mentioned, the POD technique is generally used to analyze experimental or numerical data with the view in extracting their dominant features, which will typically be patterns in space and time. On output, it provides a set of orthogonal functions which are the eigenfunctions of the covariance matrix of the data. Generally, this set is ordered in decreasing size of the corresponding eigenvalue, the larger the eigenvalue meaning the larger percentage of the data variance is contained in the dynamics of corresponding eigenfunction. Thus, if $u(x, y, t)$ is our data field ($(x, y) \in A \subset R^2$ is the spatial point and t is time) to which the temporal average has been subtracted, the POD basis $\{\phi_i(x, y), i = 1, ..., \infty\}$ is obtained after solving

$$\int_A < u(x,y,t)u(x',y',t) > \phi_i(x',y')dx'dy' = \lambda_i\phi_i(x,y), \tag{6.1}$$

being $< \cdot >= \frac{1}{T}\int_0^T \cdot\, dt$, i.e., the time average, and λ_i the corresponding eigenvalues, which are ordered in decreasing size $\lambda_1 \geq \lambda_2 \geq ... \geq 0$. Therefore, we have the modal decomposition

$$u(x,y,t) = \sum_{i=1}^{\infty} a_i(t)\phi_i(x,y), \tag{6.2}$$

where the $a_i(t)$ are the so-called temporal modes. In addition, the following orthogonality conditions are fulfilled

$$\int_A \phi_k(x,y)\phi_l(x,y)dxdy = \delta_{kl}, \tag{6.3}$$

$$\langle a_k(t)a_l(t)\rangle = \frac{1}{T}\int_0^T a_k(t)a_l(t)dt = \lambda_k\delta_{kl}, \tag{6.4}$$

where δ_{kl} is the Kronecker delta.

The optimality of the POD basis functions means that [10], among all linear decompositions with respect to an arbitrary basis $\{\Phi_i(x,y)\}$, for a truncation or order N, i.e., $u^N(x,y,t) = \sum_{i=1}^N a_i(t)\Phi_i(x,y)$, with $a_i(t) = \int_A u(x,y,t)\Phi_i(x,y)$, the minimum error, defining the error as $\epsilon = \left\langle \int_A (u-u^N)^2 dxdy \right\rangle$, is obtained when $\{\Phi_i\}$ is the POD basis $\{\phi_i(x,y)\}$.

We now apply the POD analysis to the altimetry satellite data. The results of this are outlined in the following. Fig. 6.2 shows (in linear-log scale) the fraction of variance $\lambda_i/(\sum_{n=1}^N \lambda_n)$, given by each eigenvalue. It is clearly seen that most of the variance is captured by the first and second eigenvalues. In Fig. 6.3 we show the temporal mode associated to the first two eigenvalues, and the power spectrum of the four dominant ones is plotted in Fig. 6.4. The annual seasonal periodicity is clearly observed in the two dominant modes. This and more detailed observations in terms of a complex version of the POD on the same data set [85] allow us to interpret the dynamics given by these dominant eigenfuntions as the seasonal response of the ocean (heating in summer and cooling in winter) along the annual cycle.

Therefore, to get a deeper insight into the data (and in particular in the mesoscale phenomena), we have to study other eigenfunctions than the first two. In Fig. 6.5 we show again the fraction of variance of the eigenvalues (linear-log plot) but in this case we have removed the first two eigenvalues. We observe that eigenvalues 3^{rd} and 4^{th} are equivalent under the error bar (for calculating error bars in POD eigenvalues see [86]). In this case, a linear superposition of them can represent a moving coherent structure [70]. In Fig. 6.6 we show the temporal modes associated with eigenvalues 3^{rd} and 4^{th}. This Figure, and the corresponding power spectra in Fig. 6.4 suggest a weak semiannual periodicity for both modes.

Visualization of the time evolution of the data filtered to keep just the eigenfuntions 3^{rd} and 4^{th}, i.e., $u_{34}(x,y,t) = a_3(t)\phi_3(x,y) + a_4(t)\phi_4(x,y)$, suggest a vortex moving northward and eastwards from the Algerian coast, in agreement with the results of [85]. The approximate periodicity of the associated temporal modes indicates that new vortices are shed from the coast roughly every six months. Describing the dynamics of this coherent structure found in the flow will be our goal in the remaining of the Chapter.

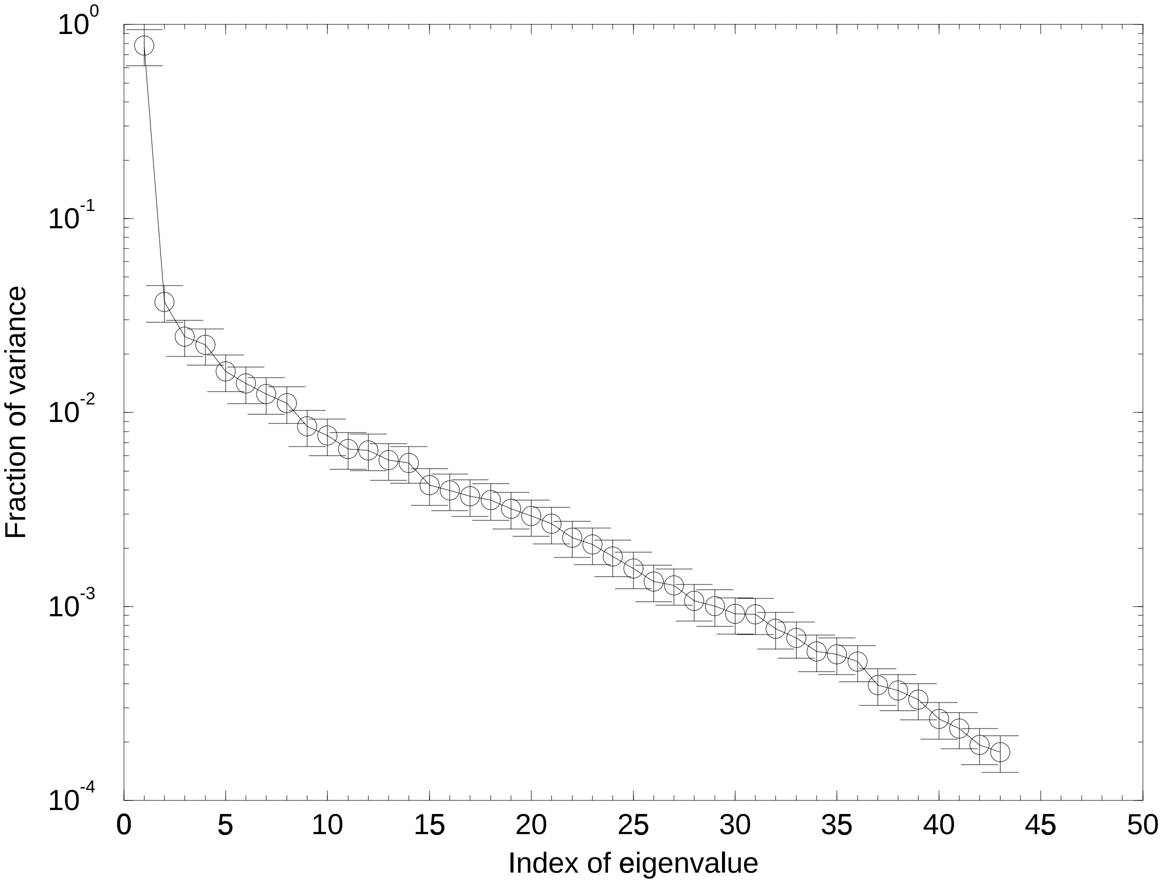

Figure 6.2: Linear-log plot of the fraction of variance of the eigenvalues in terms of their index.

6.4 Model and low-dimensional dynamical system

The classical way of using POD to obtain a low-dimensional dynamical system approximation, which takes into account the most relevant features of the physical system, consists in truncating the expansion (6.2) to a particular order [10, 100, 73, 74, 75, 76]. This order is generally chosen to contain most of the percentage of the variance of the data. Then, the equations governing the dynamics of the system (PDEs from which the data may have been generated numerically) are projected over this particular Galerkin basis and a system of ODEs for the temporal modes $a_i(t)$ can be obtained. Our approach is somewhat different, first of all, our data are from satellite observations and we need a specific mathematical model to describe approximately our data, and second, our interest focuses in the dynamics associated with the eigenfuntions 3^{rd} and 4^{th} which seem to contain the evolution of the moving mesoscale vortex, and not the more dominant eigenfunctions 1^{st} and 2^{nd}.

Proceeding with the modeling step, and supported by marine experimental campaigns [85, 87], we assume that the strong mesoscale activity in the Algerian current is mainly due

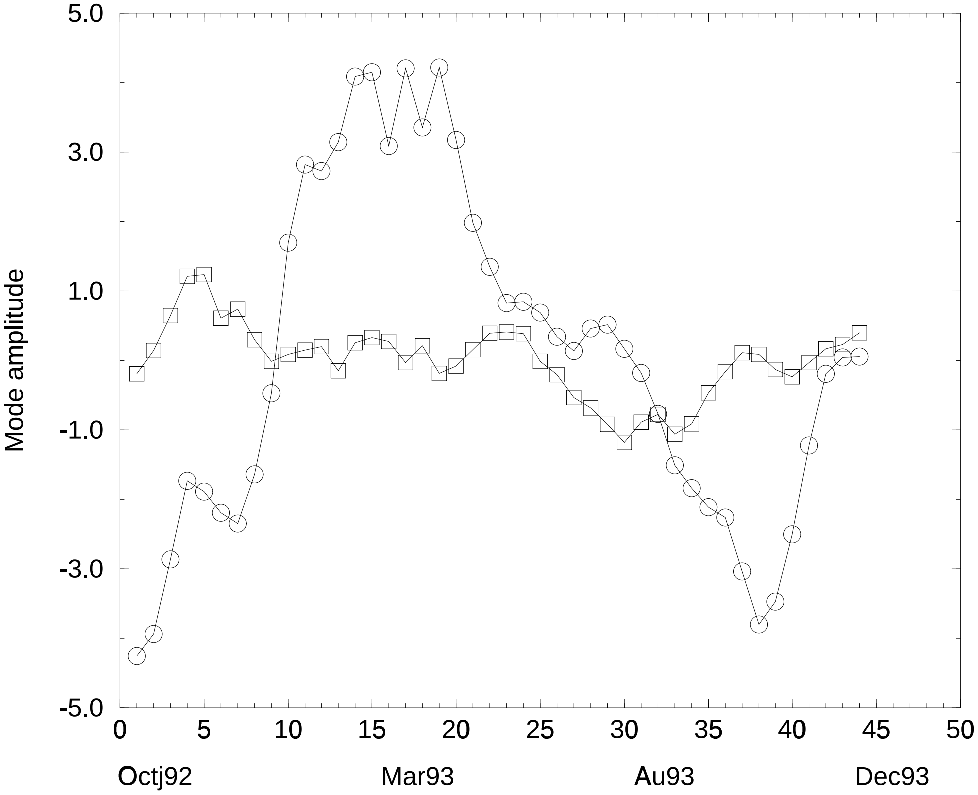

Figure 6.3: Temporal modes associated the first two eigenvalues. Circles are the data for the first and squares for the second.

to baroclinic instability phenomena. This name refers to the instabilities grown from the available potential energy associated with horizontal gradients of density [2]. Therefore, we choose a two-layer quasigeostrophic model as our basic flow description since this is the minimal model accounting for these type of instabilities. Layered quasigeostrophic models are widely used in oceanographical modeling and their main assumption is that the ocean behaves as having different layers where density is constant and, in all the different layers, geostrophic balance is maintained (i.e. Coriolis and pressure forces nearly equilibrate via a quasibidimensional flow). Actually, the spatial scales of the chosen region, and its strong topographic features, lead however to important deviations from quasigeostrophy. Thus, the postulated model should be considered at most as a crude approximation to the real dynamics. It is one of the objectives of this Chapter to show that the empirical information contained in the satellite data is incorporated into the model during the projection procedure, so that the final low-dimensional model gives a reasonable description of the dynamics.

In the framework of multilayer quasigeostrophic models, every fluid layer i of density ρ_i and thickness h_i is described by a stream function ψ_i, which is proportional to the pressure

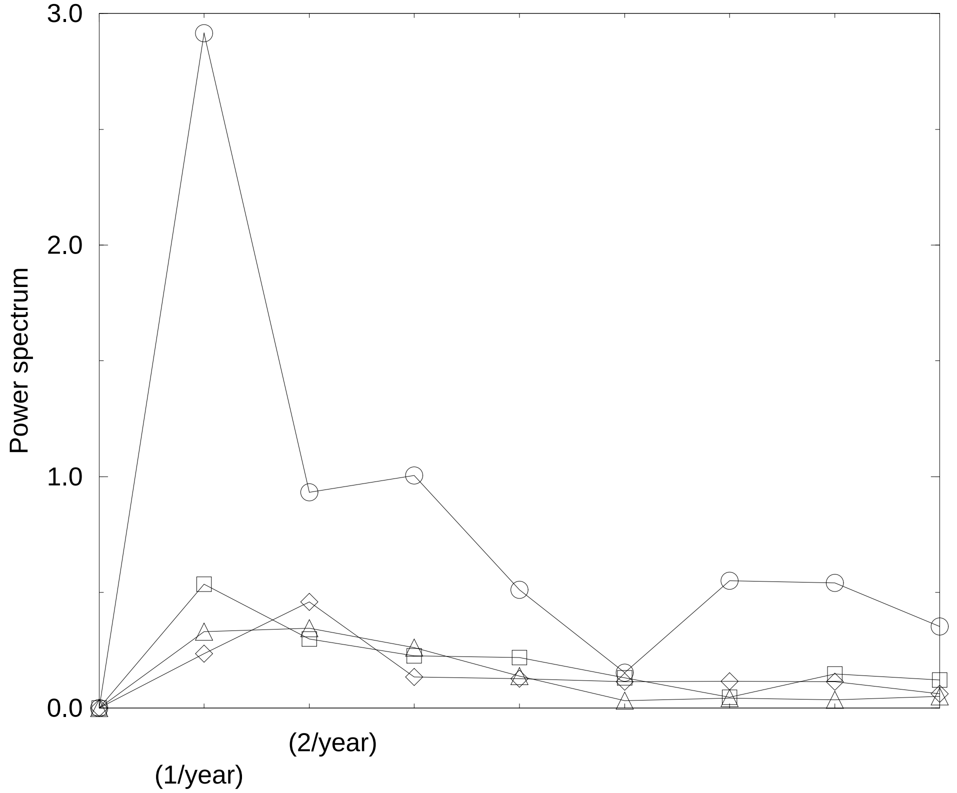

Figure 6.4: Power spectrum of the first four temporal modes. Circles, first mode; squares, second mode; triangles, third mode; and diamonds, fourth mode.

field within the layer, and such that the horizontal velocities $\mathbf{v_i} = (u_i, v_i)$ within the layer verify $u_i = -\frac{\partial \psi_i}{\partial y}$ and $v_i = \frac{\partial \psi_i}{\partial x}$. In our equations, the coordinate directions x and y will be oriented along the northward and the eastward directions, respectively.

More specifically we use a *two-layer quasigeostrophic model on a beta plane and over topography*. An *eddy-viscosity* and a *bottom friction* terms are also included. The equations defining the dynamics of the stream function of both layers are

$$\frac{D_1}{Dt}\left[\nabla^2\psi_1 + f + \frac{\psi_2 - \psi_1}{R_1^2}\right] = \nu\nabla^4\psi_1, \tag{6.5}$$

$$\frac{D_2}{Dt}\left[\nabla^2\psi_2 + f + \frac{\psi_1 - \psi_2}{R_2^2} + f_0\frac{\tau}{H_2}\right] = \nu\nabla^4\psi_2 - C_b\nabla^2\psi_2, \tag{6.6}$$

where the subscript $i = 1$ (2) refers to the upper (bottom) layer, $\frac{D_i}{Dt} = \frac{\partial}{\partial t} + J(\psi_i, \cdot)$, $\psi_i(x, y, t)$ is the layer stream function, $\tau(x, y)$ is the bottom topography, $R_1 = \frac{N_1 H_1}{f_0}$, $R_2 = \frac{N_2 H_2}{f_0}$, $N_1^2 = \frac{g\delta\rho}{H_1\rho_2}$, $N_2^2 = \frac{g\delta\rho}{H_2\rho_2}$, where $\delta\rho = \rho_2 - \rho_1$. g the gravitational acceleration, H_i is the mean thickness of the layer i, and f is the *Coriolis parameter*, which in the beta-

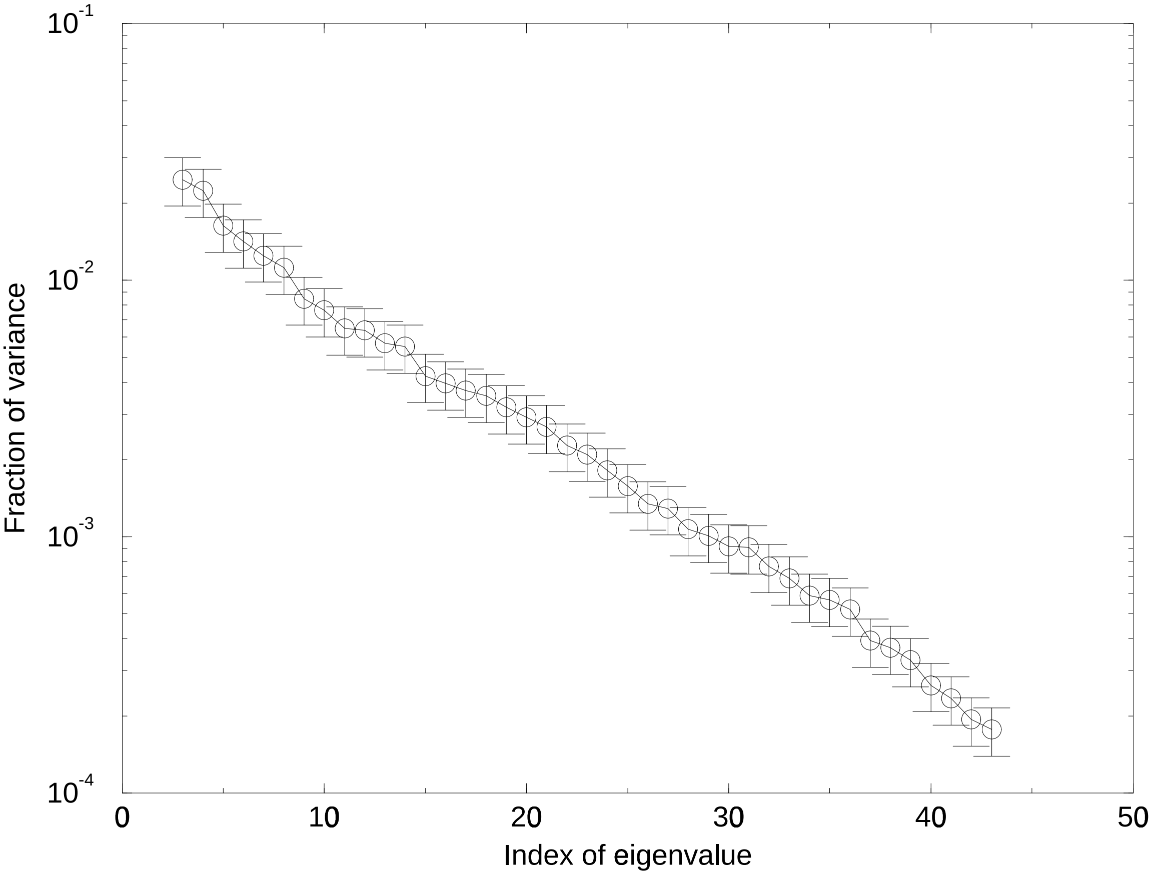

Figure 6.5: Linear-log plot showing the fraction of variance contained in the different eigenvalues starting from the third one.

plane approximation depends on the latitude as $f = f_0 + \beta y$. ν is the eddy-viscosity and C_b is the coefficient describing friction with the bottom of the sea. The Jacobian operator $J(A, B)$ is defined as:

$$J(A,B) = \frac{\partial A}{\partial x}\frac{\partial B}{\partial y} - \frac{\partial A}{\partial y}\frac{\partial B}{\partial x}. \tag{6.7}$$

More details about quasigeostrophic dynamics can found for example in Refs. [2] and [89]. A more explicit way to write our equations (6.5) and (6.6) is

$$\begin{aligned} \frac{\partial \nabla^2 \psi_1}{\partial t} + \frac{1}{R_1^2}\frac{\partial(\psi_2 - \psi_1)}{\partial t} + \quad & \frac{\partial \nabla^2 \psi_1}{\partial x}\frac{\partial \psi_1}{\partial y} - \frac{\partial \nabla^2 \psi_1}{\partial y}\frac{\partial \psi_1}{\partial x} \\ -\frac{1}{R_1^2}\left(\frac{\partial \psi_1}{\partial x}\frac{\partial \psi_2}{\partial y} + \frac{\partial \psi_1}{\partial y}\frac{\partial \psi_2}{\partial x}\right) + \quad & \beta \frac{\partial \psi_1}{\partial x} = \nu \nabla^4 \psi_1, \qquad (6.8) \\ \frac{\partial \nabla^2 \psi_2}{\partial t} + \frac{1}{R_2^2}\frac{\partial(\psi_1 - \psi_2)}{\partial t} + \quad & \frac{\partial \nabla^2 \psi_2}{\partial x}\frac{\partial \psi_2}{\partial y} - \frac{\partial \psi_2}{\partial x}\frac{\partial \nabla^2 \psi_2}{\partial y} \end{aligned}$$

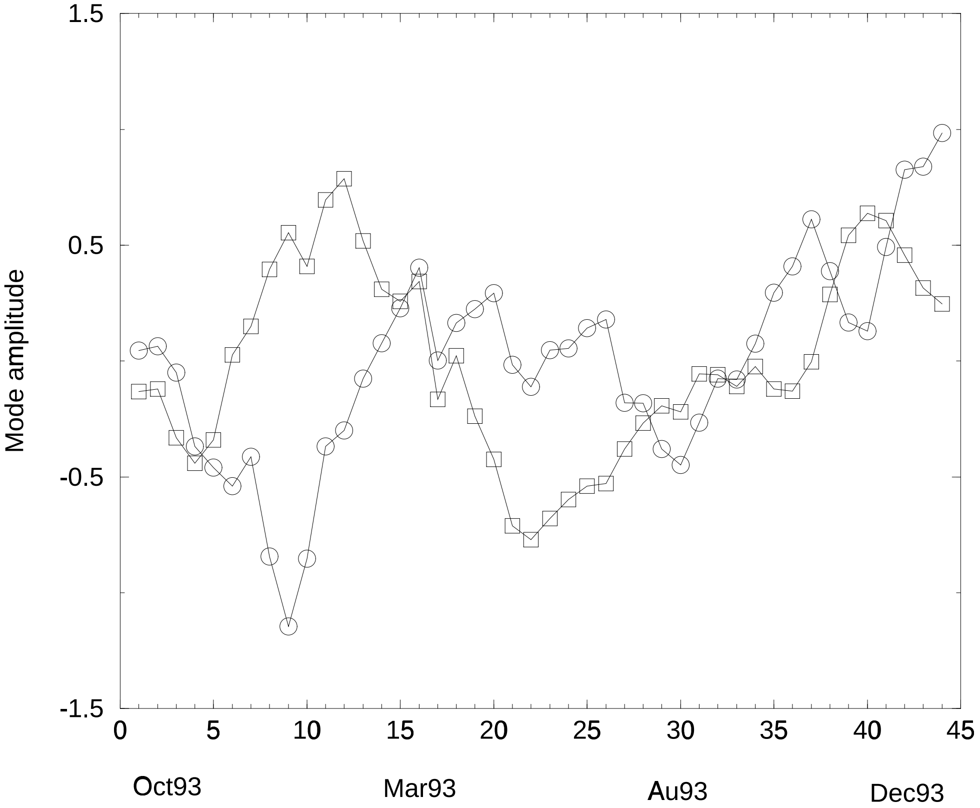

Figure 6.6: Temporal modes for the third and fourth eigenfunctions. Squares, third mode; circles, fourth mode.

$$-\frac{1}{R_2^2}\left(\frac{\partial\psi_2}{\partial x}\frac{\partial\psi_1}{\partial y}+\frac{\partial\psi_2}{\partial y}\frac{\partial\psi_1}{\partial x}\right)+\qquad\frac{f_0^2}{gH_2}\left(\frac{\partial\psi_2}{\partial x}\frac{\partial\tau}{\partial y}-\frac{\partial\psi_2}{\partial y}\frac{\partial\tau}{\partial x}\right)+\beta\frac{\partial\psi_2}{\partial x}=$$
$$\nu\nabla^4\psi_2-C_b\nabla^2\psi_2 \qquad (6.9)$$

In this model the stream function of the upper layer is $\psi_1(x,y,t)=\frac{g}{f_0}h(x,y,t)$ where $h(x,y,t)$ is the height of the sea surface over the point (x,y) at time t. This last quantity is the one linked to the satellite observations on which we have performed the POD. It is important to note that in equations (6.8) and (6.9) we have not considered an annual forcing term which accounts for the the seasonal variability of the Algerian Current. This is a very important fact for the next step in our approach, the projection onto a particular Galerkin basis determined from the observations. We assume the following ansatz:

$$\begin{aligned}\psi_1(x,y,t) &= <\psi(x,y,t)> +\psi'(x,y,t)\\ &= \frac{g}{f_0}(<h(x,y,t)> +\hat{a}_3(t)\phi_3(x,y)+\hat{a}_4(t)\phi_4(x,y)),\end{aligned}\qquad (6.10)$$

where the temporal coefficients $\hat{a}_3(t)$ and $\hat{a}_4(t)$ will be calculated in the following sections and, finally, compared with the POD temporal coefficients $a_3(t)$ and $a_4(t)$. With

(6.10) we assume that the stream function ψ_1 (which is proportional to the height) of the upper layer is decomposed in its temporal mean $<\psi(x,y,t)>=\frac{g}{f_0}<h(x,y,t)>$, accounting for the annual mean flow, and a perturbation $\psi'(x,y,t)=\frac{g}{f_0}(\hat{a}_3(t)\phi_3(x,y)+\hat{a}_4(t)\phi_4(x,y))$, which models the mesoscale processes [88]. The perturbation basis for the height $\{\phi_3(x,y),\phi_4(x,y)\}$ is what we have obtained from the POD analysis of the data, and the way to calculate the annual mean will be detailed at the end of this Section.

As we have no real measure for the bottom layer (the satellite sensors get data just from the sea surface), we need to make some additional hypothesis in our model. We propose the following ansatz for the expansion of the bottom layer's stream function

$$\psi_2(x,y,t) \;=\; -Uy+Vx+\frac{g}{f_0}(b_3(t)\phi_3(x,y)+b_4(t)\phi_4(x,y)), \tag{6.11}$$

where U and V are parameters of our model and simulate the eastward and northward velocity, respectively, of the bottom layer flow. The physical meaning of (6.11) is that the perturbations from the mean flow for the bottom layer are generated by the same basis functions as the upper one though with, obviously, different temporal coefficients. The most important feature in the former ansatz is the mean flow, parameterized with U and V. The values of these parameters not only determine the intensity of the mean flow but also, and most importantly, its direction and sense. Discussions about the rôle of the different values of U and V will be given in the next section.

Projecting expansions (6.10) and (6.11) over equations (6.8) and (6.9) and using the orthogonality relations of the POD basis $\phi_i(x,y)$, we obtain the evolution equations for the coherent structure's temporal amplitudes $\hat{a}_i$ and b_i ($i=3,4$),

$$\begin{aligned}\frac{d\hat{a}_i}{dt} &= p_{1,i}\hat{a}_3^2+p_{2,i}\hat{a}_4^2+p_{3,i}\hat{a}_3+p_{4,i}\hat{a}_4+p_{5,i}\hat{a}_3\hat{a}_4\\ &+ p_{6,i}b_3^2+p_{7,i}b_4^2+p_{8,i}b_3+p_{9,i}b_4+p_{10,i}b_3b_4+p_{11,i},\\ \frac{db_i}{dt} &= q_{1,i}\hat{a}_3^2+q_{2,i}\hat{a}_4^2+q_{3,i}\hat{a}_3+q_{4,i}d_2+q_{5,i}\hat{a}_3\hat{a}_4\\ &+ q_{6,i}b_3^2+q_{7,i}b_4^2+q_{8,i}b_3+q_{9,i}b_4+q_{10,i}b_3b_4+q_{11,i}.\end{aligned} \tag{6.12}$$

The coefficients $p_{k,i}$ and $q_{k,i}$ ($k=1,..,11$ and $i=3,4$) are real numbers that depend on the parameters of the model and on integrals containing $<\psi>$, $\phi_3(x,y)$, $\phi_4(x,y)$, the and their derivatives. Their explicit expressions are quite complex and have been obtained by computer algebraic manipulation. We do not write down here all these involved expressions. Just to give an example of them, in Appendix A we display the mathematical expression for $q_{10,2}$.

We finally proceed to explain how to obtain the mean flow $<\psi(x,y,t)>$, without which the coefficients in (6.12) remain undetermined. Some manipulations of the data are needed because of the bad spatial resolution of the available mean field. We recall that we are dealing with Sea Level Anomaly (SLA) data obtained from the two altimetric missions ERS-1 and T/P. These are conveniently treated to obtain regular maps in space and time every 10 days and on a 0.2^o regular grid. These SLA are relative to the annual mean sea level and, therefore, we need this annual mean to obtain the total height of the sea surface and thus be able to make relation between the empirical eigenfunctions ϕ_3, ϕ_4

and the dynamic variable ψ_1 of the quasigeostrophic model (see Eq. 6.10). Unfortunately, the annual mean sea level data are not manipulated to improve their resolution, and we have just the T/P data, of a very coarse resolution (around 2.8^o) to calculate this annual mean. Therefore, we need to interpolate these to a 0.2^o regular grid and then to add the resulting annual mean to the SLA data, in order to obtain a consistent SSH field. But, all these manipulations are, at the end, manifesting when we solve Eq. (6.12) in such a way that $\hat{a}_3(t)$ and $\hat{a}_4(t)$ have nonzero average, in contrast with the POD temporal modes, $a_3(t)$ and $a_4(t)$, calculated from data, i.e.,

$$\frac{1}{T}\int_0^T \hat{a}_i(t)dt \neq 0, \;\; i = 3, 4. \tag{6.13}$$

In order to heal this, we proceed with an assimilation-like approach: we modify the annual mean sea level, which has been obtained interpolating the T/P data, by adding this nonzero average, i.e.,

$$h_m(x,y) = h_m^{T/P}(x,y) + \frac{f_0}{g}\frac{1}{T}\int_0^T \hat{a}_3(t)(\phi_3(x,y,t) + \hat{a}_4(t)\phi_4(x,y,t))dt, \tag{6.14}$$

being $h_m(x,y)$ the new annual mean height and $h_m^{T/P}(x,y)$ is the interpolated T/P annual mean height. Finally, and with high numerical accuracy, the new temporal modes obtained from Eq. (6.12) have now temporal zero average.

Summing up, the data we are using along this Chapter are obtained by adding to the SLA data the above calculated $h_m(x,y)$ field. It is important to note that because in the POD analysis we substract the mean field of the data, the qualitative features of the analysis are similar if we analyse the SLA data or the SLA plus the h_m field. Nonetheless, the quantitative differences are not negligible at all at the level of the dynamical system (6.12).

The four-dimensional dynamical system (6.12), now fully defined, is the desired low-dimensional approximation aimed to describe the coherent structures in our data set. In the next Section we show that the dynamics of the observed coherent eddy is recovered from (6.12).

6.5 Numerically generated coherent structure dynamics

We now proceed to integrate the equations (6.12). First, typical values for the parameters of the quasigeostrophic model (6.8) and (6.9) are needed. At mid-latitudes, adequate values for the parameters giving the Coriolis force are $\beta = 1.0\ 10^{-11}\ m/s$ and $f_0 = 10^{-4}s^{-1}$ [2, 3]. In addition, for the Algerian Current area the values $\rho_1 = 1025\ kg/m^3$ and $\rho_2 = 1029\ kg/m^3$ are adequate for the densities of the upper and bottom layer and $H_1 = 300\ m$, $H_2 = 3500\ m$ for their mean heights. The bottom topography $\tau(x,y)$ are real data obtained from the data basis at the URL 'http://modb.oce.ulg.ac.be/Bathymetry.html'. For the friction parameter with the bottom topography we take a value of $C_b = 1.5\ 10^{-6}$. A typical value for the eddy viscosity at the scales we are working is $\nu = 200\ m^2/s$. The remaining parameters are the geostrophic velocities of the bottom layer. This is a difficult task since nobody really knows what happens in the deep waters of the Algerian Current. Anyway, recent results obtained by the PRIMO-1 experiment in the channel of Sardinia

[85] seem to indicate that typical velocities for the deep layer are rather weak (of the order of $1\ cm/s$), though it is not clear if the *deep layer flow* (dlf) is westward or eastward. Therefore we assume dlf following the upper layer, this is northeastward, with typical values of: $U = 5\ cm/s$ and $V = 5\ cm/s$. In the next Section, other values of U and V will be discussed.

Fig. 6.7 shows $\hat{a}_3(t)$ and $\hat{a}_4(t)$ obtained by integrating (6.12) with a fourth order Runge-Kutta method. The periodicity of both is evident, being the period of around 5 moths, in good agreement with the observed one. If some annual forcing would be added to our model, this period would probably lock to the semiannual harmonic, still improving the agreement. The shape of the oscillation in the calculated evolution is much more regular than the experimental one, as expected from a clean simulation versus noisy data. In Fig. 6.8 we show a temporal sequence of the coherent structure dynamics given by $\hat{a}_3(t)\phi_3(x,y) + \hat{a}_4(t)\phi_4(x,y)$ from the calculated temporal modes. An eddy appears next to the coast and moves northeastward, the process being repeated five months later. This is fully consistent with the observed data and confirms the success in our task of obtaining a low-dimensional reduced model. Sensibility of the results to variations in the values chosen for the parameters is discussed in terms of a bifurcation analysis in the next Section.

6.6 Bifurcation analysis

The value of the eddy viscosity ν is somehow arbitrary since it would depend on the scale of observation. Thus, a discussion of the variations in model behavior as ν varies is in order. We analyze numerically our system of four ODE's (6.12) with the help of the software package *Dstool* [90] which integrates the system with a fourth order Runge-Kutta. We change the eddy-viscosity parameter ν, which is proportional to the inverse of the Reynolds number, and observe the bifurcation behavior. The rest of the parameters take the same values as in the former section. It should be noted that in principle the empirical eigenfunctions would vary in a system with varying ν, but since we just have experimental data for the actual value of the eddy viscosity in the ocean at the observed scales, we keep the parameters in (6.12) as determined from the POD of the observed data. The bifurcation diagram is outlined as follows:

- For $\nu \geq 212\ m^2/s$ there are six fixed points. Two of them are stable and the rest are unstable.

- When $\nu = 212\ m^2/s$ a Hopf bifurcation occurs. One of the stable fixed points (the one localized at the origin) gets unstable by decreasing ν and a limit cycle appears surrounding it. The limit cycle persists for all the values of the viscosity smaller than $212\ m^2/s$. The system undergoes no new bifurcations by decreasing the viscosity parameter.

The main dynamical feature in our model is thus the existence of a Hopf bifurcation which gives birth to a limit cycle for a long range of ν values, including the physical ones at the scales we are working. All these limit cycle solutions give rise, after reconstruction of the coherent structure with the help of the empirical eigenfunctions, to traveling wave

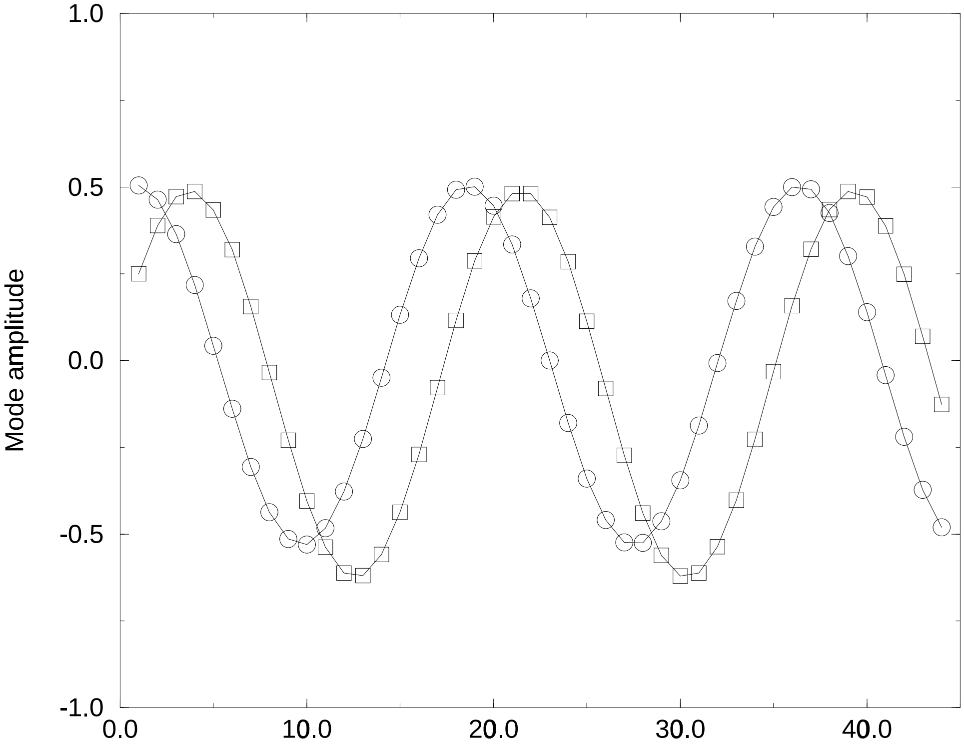

Figure 6.7: Temporal evolution of the third and fourth temporal modes obtained by numerical integration Eq. 6.12

patters with a period of around six months. In particular, the moving eddy identified in section 6.5 is just one of these solutions. Moreover, the rest of the fixed points in the second regime, i.e. when $\nu \leq 212$, seem to have no physical significance as their basins of attraction correspond to very high values of the initial condition for $\hat{a}_i(t)$ $(i = 3, 4)$, i.e., high values of the sea surface height. When the eddy-viscosity is too large, the system evolves towards a stable fixed point, with no moving coherent structures, as expected on physical grounds.

To give a stronger support to the former analysis, we have tested our ODE system with other values of the dlf velocity. We have observed numerically the following behaviour of the system:

- High values of U or V, $\sim 10\, cm/s$, produce diverging solutions, with no fixed points for any value of ν. Very low values ($\sim 10^{-2}$ cm/s) give rise also to unbounded solutions for any initial condition in some range of high viscosity values (low Reynolds number), which is not reasonable on physical grounds.

- Changing sign in U, that is, assuming a westward flow in the bottom layer, does not

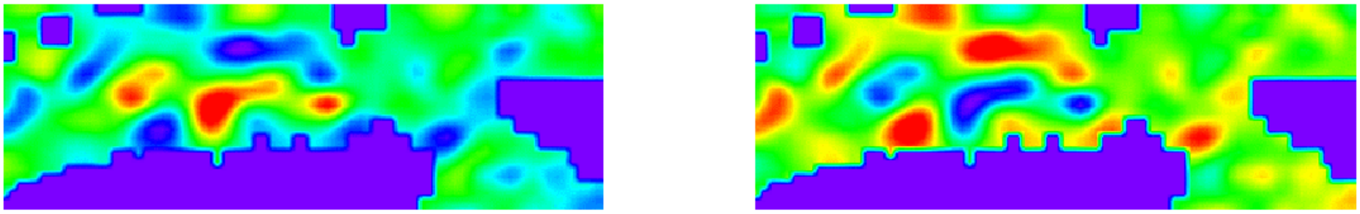

a) Dec. 1992

e) End of Marc. 1993

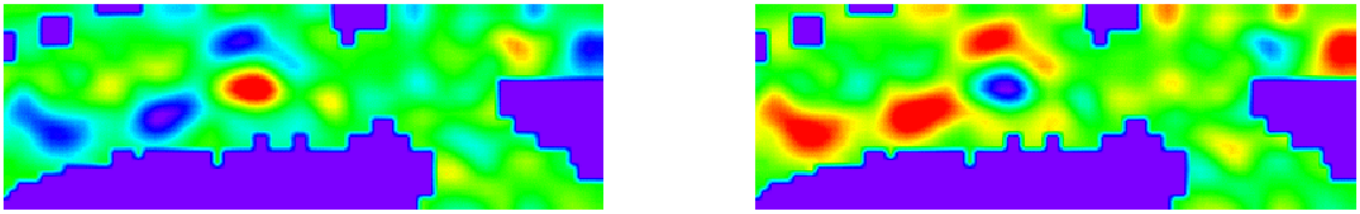

b) Jan. 1993

f) Beginning of Ap.1993

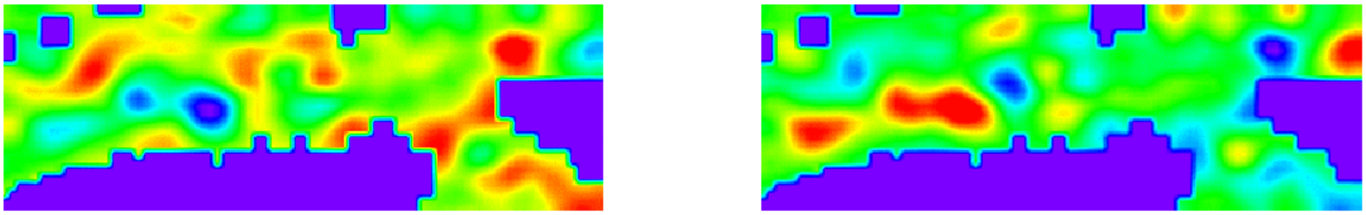

c) Feb. 1993

g) End of Ap. 1993

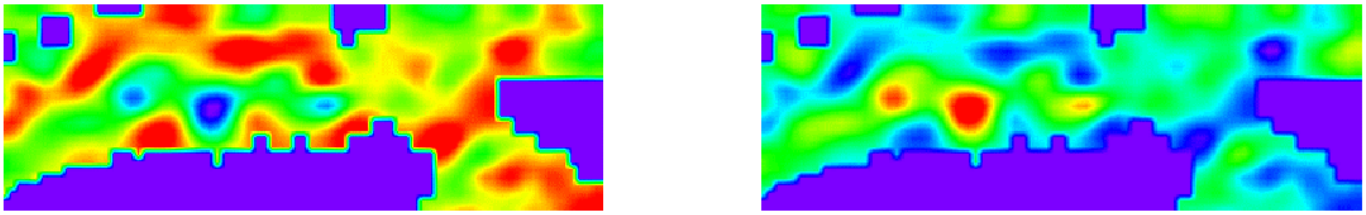

d) Beginning of Marc. 1993

h) May 1993

Figure 6.8: Numerical reconstruction of vortex shedding and motion near the Algerian coast. After h) the same sequence is repeated. The blue area (higher altimetric values) next to the coast corresponds to an anticyclonic vortex (the moving coherent structure under study). In the figure, it always appears with its corresponding cyclonic vortex (red area).

change considerably the bifurcation diagram, but the amplitude of the limit cycle is too big when reasonable values of the viscosity (around $200\ m^2/s$) are used. On the contrary, changing sign in V or in U and V simultaneously gives rise to a ODE system where all the solutions are unbounded.

We think these are enough reasons supporting the chosen direction and magnitude of the velocity of the dlf, that is, a northeastward direction and typical values for the horizontal velocites around $5\ cm/s$.

6.7 Summary

In this Chapter we have used the Proper Orthogonal Decomposition to obtain a low-dimensional dynamical description of coherent structures observed in satellite data of a region of the Mediterranean Sea. First, analysis of the altimetric satellite data via the POD allows the identification of a moving vortex in the ocean surface. Second, projection of a two-layer quasigeostrophic model onto the empirical basis, together with some physical assumptions on the unobserved part of the sea, allow the construction of a fourth-order dynamical system that gives a reasonable description of the dynamics of the coherent structure, in particular its period and amplitude. It is remarkable that a crude PDE model, and noisy data, can be merged to obtain an efficient reduced model.

Chapter 7

Forecasting confined spatiotemporal chaos with genetic algorithms

A technique to forecast spatiotemporal time series is presented. It uses a Proper Orthogonal or Karhunen-Loève Decomposition to encode large spatiotemporal data sets in a few time-series, and Genetic Algorithms to efficiently extract dynamical rules from the data. The method works very well for confined systems displaying spatiotemporal chaos, as exemplified here by forecasting the evolution of the one-dimensional complex Ginzburg-Landau equation in a finite domain.

7.1 Introduction

Nonlinear time-series analysis provides tools to identify dynamical systems from measured data [91]. The approach has been greatly developed in the last years as a powerful alternative to linear stochastic methods in the modeling of irregular time-series and provides, under the assumption of deterministic behavior, useful recipes for system control, noise reduction, and forecasting. Applications of these techniques to situations of spatiotemporal chaos, however, is still in its beginnings [92, 93]. There are two main reasons for this: a) the large attractor dimensions of spatiotemporally chaotic systems, increasing with system size, poses serious difficulties to the standard methods of delay embedding and attractor reconstruction; b) the right choice of variables is far from obvious: whereas the time evolution of an observable at a particular space point could be enough in some particular situations, decaying space correlations, and propagation phenomena would turn this to be a poorly performing choice in most cases.

A very efficient method for time-series prediction using Genetic Algorithms (GA) has been recently proposed in [94] for nonextended systems. Comparatively small data sets are enough to use this technique, which makes it competitive in facing difficulty a) i.e., prediction in the presence of attractors of large dimension. In some cases, even non-trivial functional forms of dynamical systems generating the data can be unveiled [95]. In this Chapter we extend the GA approach to the forecasting of *confined spatiotemporal chaos*. By this we mean the situation in which chaotic dynamics in an extended system is strongly affected by the presence of boundaries. Our interest in this situation, somehow intermediate between low-dimensional chaos and homogeneous extensive chaos, arises from its relevance to real experimental situations [96, 97], and from recent work [98] leading to theoretical understanding: the boundaries break translational symmetry and the resulting phase rigidity restricts the shape of the chaotic fluctuations allowed. This manifests for example in the appearance of nontrivial average patterns [96, 98] and in inhomogeneities in other statistical characteristics [97, 99]. Under these circumstances the Empirical Orthogonal Functions (EOF's) [10, 100] obtained from a Proper Ortogonal Decomposition (POD, also known as Karhunen-Loève decomposition) provide an excellent basis for describing the system dynamics. They are different from simple Fourier modes and contain information (optimal in a precise sense) on the broken translational symmetry. The amplitudes of the most important EOF's will be the variables chosen in response to difficulty b). By increasing system size, the dynamics would leave the regime of confined spatiotemporal chaos and at some point extracting and using information on local structures as in the methods of [92, 93] would become advantageous over the POD representation. The GA's however could still be used as predictors for the new representation.

7.2 Method

We now describe more in detail our method for spatiotemporal forecasting, in which the POD is used to encode the large spatiotemporal data set in a few time-series, and the GA approach is used to obtain the corresponding forecasts. Given a time series of spatial patterns $U(\mathbf{x}, n)$, where $n = 1, ..., N$ labels the temporal sequence and $\mathbf{x}$ the M spatial points in a d-dimensional mesh, the POD decomposes the fluctuations around the temporal mean $u(\mathbf{x},n) \equiv U(\mathbf{x},n) - \langle U(\mathbf{x},n)\rangle_n$ into modes ranked by their temporal variance. As a result, a set of spatial EOF's and associated temporal amplitude functions are obtained. The EOF's $\phi_i(\mathbf{x})$ ($i = 1,...,M$) are the (orthogonal) eigenfunctions of the covariance matrix of the data $C(\mathbf{x},\mathbf{x}') = \langle u(\mathbf{x},n)u(\mathbf{x}',n)\rangle_n$ and are the spatial structures statistically more representative of the fluctuations in the data set. Temporal amplitude functions $a_i(n)$, describing the dynamics of the system, are obtained from the modal decomposition $u(\mathbf{x},n) = \sum_{i=1}^{M} a_i(n)\phi_i(\mathbf{x})$. If only $K < M$ of the EOF's (the ones containing the highest temporal variance as measured by the corresponding eigenvalues) are used in the reconstruction process, the set of reconstructed patterns

$$u^K(\mathbf{x},n) = \sum_{i=1}^{K} a_i(n)\phi_i(\mathbf{x}) \tag{7.1}$$

is still the best approximation one can obtain by linearly combining K arbitrary spatial patterns multiplied by K arbitrary amplitude functions[10]. Even more, it has been shown for several chaotic and even turbulent confined systems [10, 100] that taking a few dominating modes $K << M$ provides a good approximation to the complete data set.

Forecasting of the amplitude functions is performed with a Genetic Algorithm. In general, GA's are computational methods to solve optimization problems in which the optimal solution is searched iteratively with steps inspired in the Darwinian processes of natural selection and survival of the fittest [101]. Here the optimization problem to be solved is finding the empirical model best describing the data, that is, finding the optimum function F_i that minimizes the difference $E_i^2 \equiv \sum_{n=1}^{N} (a_i(n) - \tilde{a}_i(n))^2$ between the values $a_i(n)$ of each time series and the corresponding estimator given by

$$\tilde{a}_i(n) = F_i\left[a_i(n-1), a_i(n-2), ..., a_i(n-D)\right] \quad , \tag{7.2}$$

with $D + 1 \leq n \leq N$. Finding $F_i, i = 1,...,M$ amounts to identify the dynamical system behind the data set. Once found, Eq. (7.2) can be used to predict the future evolution of the system. If D is large enough, the existence of the exact F_i's is guaranteed by Takens theorem and its extensions [91], but a smaller D can give approximate dynamics F_i with already a reasonably low error E_i. In addition, we are not looking for all the M estimators but only for the K associated to the dominant EOF's. In our approach, the time-series associated to each EOF are modeled independently. More general multivariate estimators, with each $\tilde{a}_i$ possibly dependent on different a_j's, may in principle be used, but we restrict to the choice (7.2) for algorithmic simplicity.

The power of the GA resides in that a huge functional space is explored in order to find an optimal F_i. Each possible F_i is a formula consisting in a combination of numerical constants, variables, and arithmetic operators. This combination is stored in the computer as a symbolic string. The only limitation to the allowed functional forms (besides the limitation to arithmetic operations) is the maximum allowed length of the symbolic string. The search procedure begins by randomly generating an initial population of potential estimators F_i that will be subjected to the evolutionary process. The evolution is carried out by selecting from the initial population the strongest individuals, i.e. the functions that best fit the data, giving a smaller E_i. In practice, only a temporal part of the data set is used in this step (the *training set*), whereas the rest of the data are used later for validating the efficiency of the prediction method (*validating set*). The strongest strings choose a mate for reproduction while the weaker strings disappear. 'Reproduction' consists in interchanging parts of the symbolic strings (the 'genetic material') between the two mating individuals. As a result, a new generation of individuals (which includes the original 'parent' string) is generated. The new population is then subjected to mutation processes that change, with low probability, small parts of the symbolic strings. The evolutionary steps are repeated with the new generation, and the process is iterated until an optimum individual is finally found or after a fixed number of generations. Further details about the implementation of the algorithm can be consulted in [102].

The formulae F_i are only optimized for predicting the value of $a_i(n)$ in terms of the D amplitudes immediately before in time. We call this 'one-step-ahead forecast'. One can in principle iterate the formulae to obtain successively predictions for $a_i(n+1)$, $a_i(n+2)$, etc. But this will normally lead to results rapidly diverging with respect to the correct values because of error accumulation and amplification [94].

However, GA's can be designed specifically to forecast values of the time series not necessarily in the immediate future. For example, finding the function F_i^T minimizing the error between the actual series and the estimator

$$\tilde{a_i}^T(n) = F_i^T\left[a_i(n-T), a_i(n-T-1), ..., a_i(n-D)\right], \tag{7.3}$$

with $D+1 \leq n \leq N$, allows direct prediction of $a_i(N+T)$, that is prediction T-steps ahead, without iteration.

7.3 Numerical results

To illustrate the forecasting method we generate a data set from numerical simulation of a well-studied model equation displaying spatiotemporal chaos, the one-dimensional Complex Ginzburg-Landau equation (CGLE), supplemented with Dirichlet boundary conditions at the ends of a finite interval [100]. It is convenient for our purposes to write it as

$$\partial_t A(x,t) = q^2(1+\alpha)\partial_x^2 A + A - (1+i\beta)A|A|^2, \tag{7.4}$$

where q, α, and β are real and positive and $A(x,t)$ is a complex-valued field. We solve it in the interval $[0,\pi]$ so that the boundary conditions read $A(0) = A(\pi) = 0$. By simple scaling of the spatial coordinate one sees that this is equivalent to rewriting the equation with $q = 1$, but solving it in a domain of size $L = \pi/q$. Thus the parameter q is equivalent to an inverse system size, and decreasing it is equivalent to increasing system size. Following [100] we fix $\alpha = 4$ and $\beta = -4$ [103]. For $q < 0.2$ the system displays spatiotemporal chaos for most of the initial conditions. Decreasing q one encounters the regime of confined spatiotemporal chaos we are interested in before approaching homogeneous extensive chaos at large system sizes ($q \to 0$) [104]. According to [100], the correlation dimension of the dynamical attractor for $q = 0.14$ is 9.08. We sample our simulation every $\tau = 0.1$ time units and at spatial locations separated $\Delta = \pi/100$ space units, and follow it for 80 time units (800 samples) after discarding the initial transient starting from random initial

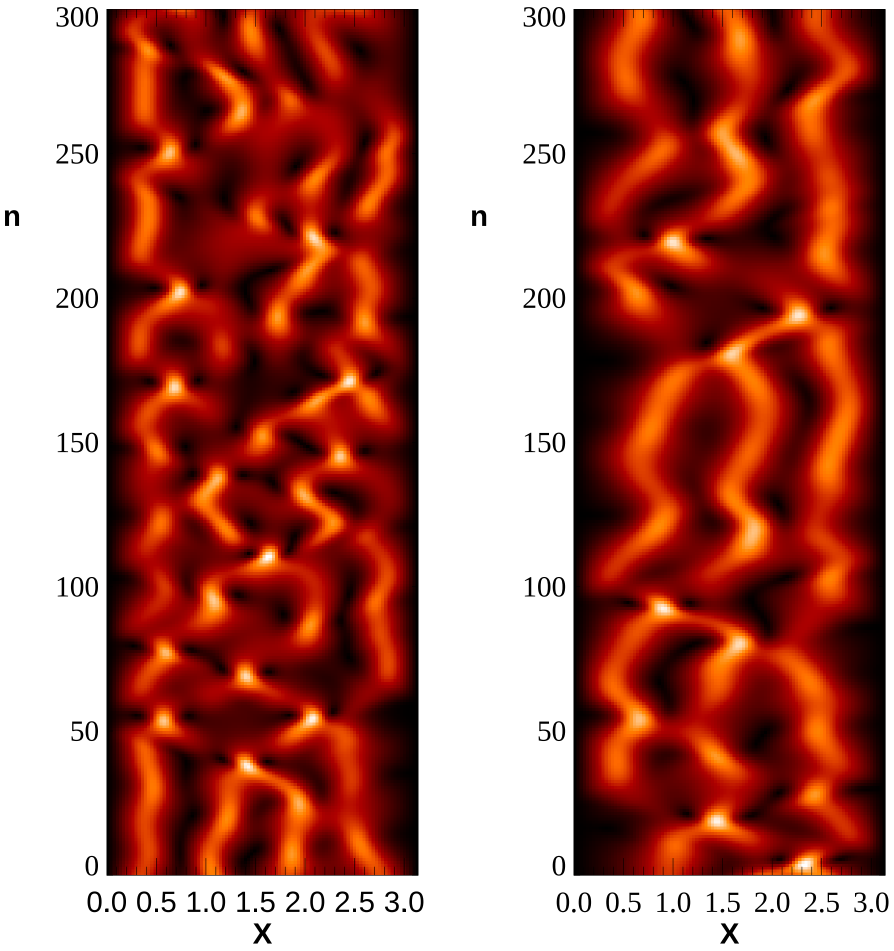

Figure 7.1: Spatiotemporal evolutions of $U(x,n)$, as given by the CGLE for $q = 0.12$ (left) and $q = 0.16$ (right). Black corresponds to $U = 0$, and lighter gray to high values of U.

conditions (this sampling leads to $N = 800$ and $M = 100$). This will be our 'training set' to be feed into the GA. The simulation is then continued for a few more time units, to provide the 'validation set' which is hidden to the GA. It is used later to check the accuracy of the predictions.

We choose as the basic field to be forecasted the *modulus* $U(x,n) = |A(x,t = n\tau)|$ of the complex field. The algorithm seems to perform slightly better in forecasting the real or the imaginary parts of A, but we use U to show that the algorithm works well with nonlinear combinations of the basic dynamical quantities. In Fig. (7.1) we show parts of typical spatiotemporal evolutions for $q = 0.12$ and $q = 0.16$. Clearly, reducing q decreases the spatial scales, as corresponding to an effectively larger system size, but also the complexity of the evolution is increased. In both cases it is clear that the motion of the dynamical structures is constrained by the presence of the walls, as corresponding to *confined* spatiotemporal chaos.

We solve Eq. (7.4) for $q = 0.18, 0.16, 0.14, 0.12$ and perform the POD on the fluctuations $u(x,n)$ of the modulus around its temporal mean value in the resulting data sets.

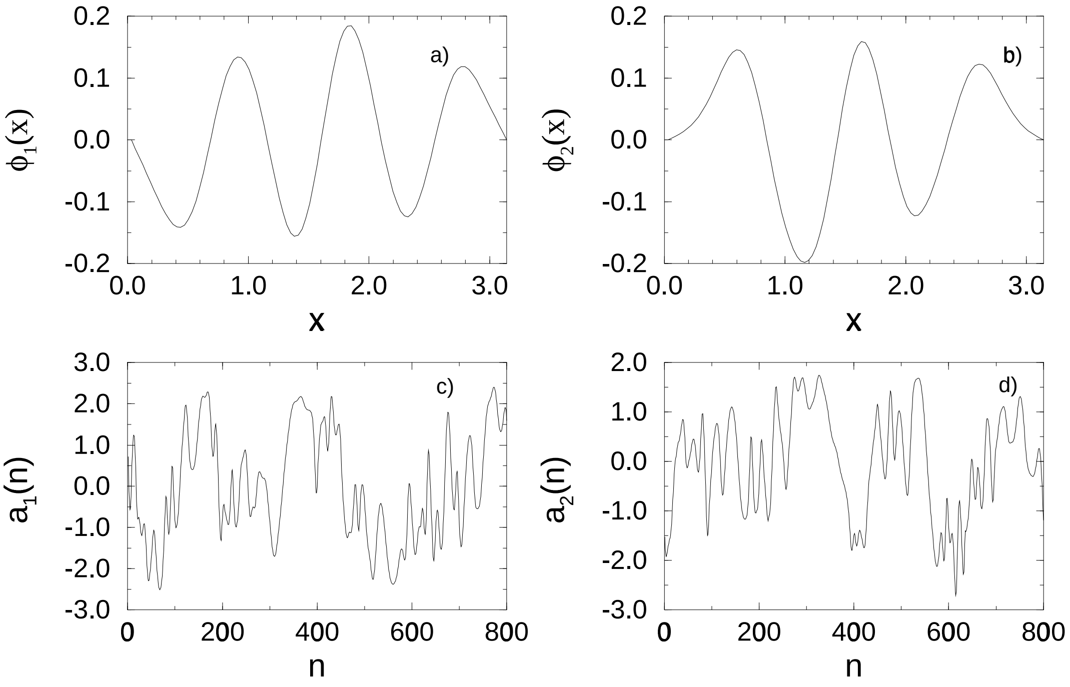

Figure 7.2: The first two EOF's (a and b), and the corresponding time amplitude functions (c and d) from the training set at $q = 0.16$.

The number of relevant EOF's (which we define to be those accounting for at least 99% of the data variance[100]) are respectively 9, 11, 13, and 15. We note that this confirms the expected approximate linear scaling of the number of EOF's with increasing system size L ($\propto q^{-1}$)[105]. It is somehow surprising that this extensive scaling appears even when chaos is not homogeneous, but still influenced by the boundaries. This fact has been observed in other systems before [97, 99]. For illustrative purposes, we show in Fig. (7.3) the two most relevant EOF's from our training set at $q = 0.16$, and the corresponding temporal amplitude functions. The chaotic character of these series is evident.

We next apply the GA to each of the amplitude functions of the relevant EOF's. We use the following parameters for all the values of q: number of generations in the evolutionary process 2000, number of individuals in each generation 120, maximum number of symbols allowed for each symbolic string 20, maximum delay in (7.2) or (7.3) $D = 18$ [106]. Tuning of these parameters for each particular value of q would improve forecasting, but would make comparisons more difficult. Predictions for the field $u(x, t)$ are then build up by reconstruction according to (7.1) with K the number of relevant EOF's defined above. In Fig. (7.3) we show the one-step-ahead forecasted fields, more concretely the prediction for the first step beyond the training set, $n = 801$. It is compared with the actual numerical pattern in the validation set, for $q = 0.12, 0.14$ and $q = 0.16$, displaying an excellent performance.

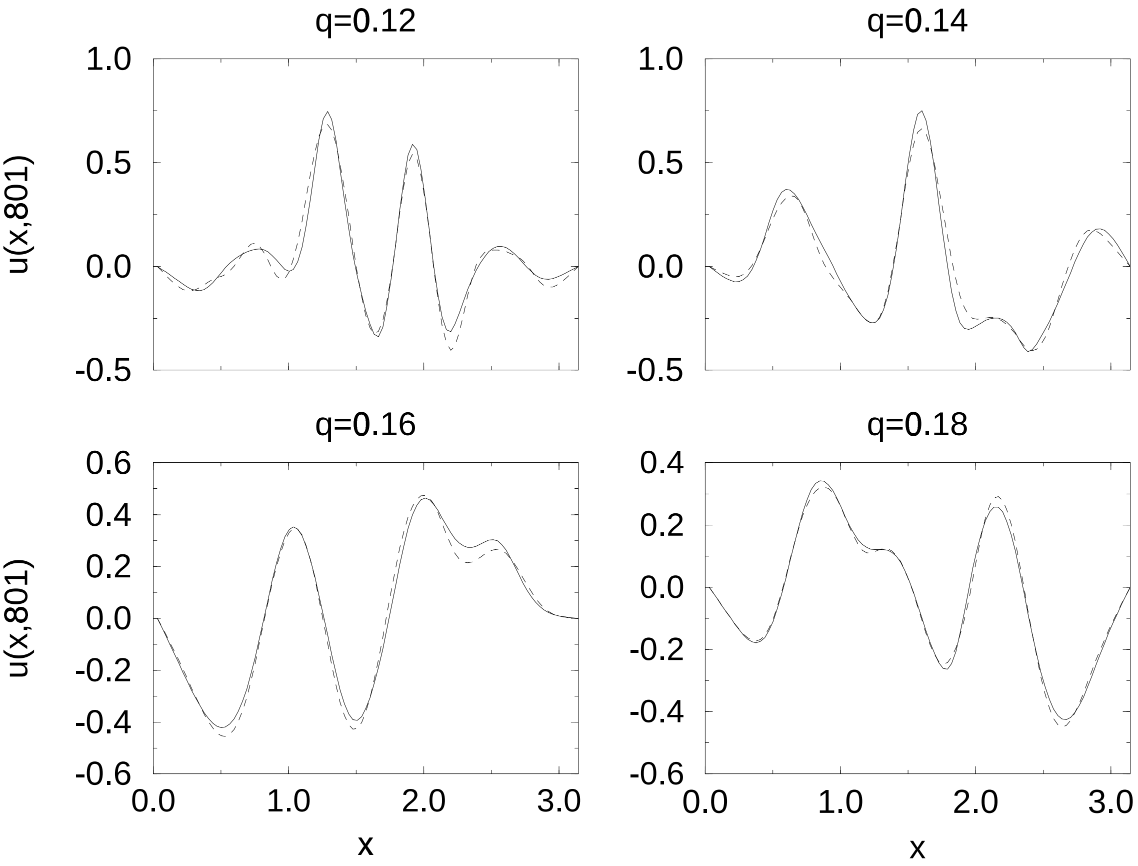

Figure 7.3: The forecasted moduli fields (dashed line) as compared to the real ones (solid) for one-step-ahead prediction for several values of q.

We quantify the quality of the prediction in terms of the mean square error $\epsilon_q(n)$:

$$\epsilon_q^2(n) \equiv \frac{1}{M}\sum_{j=1}^{M}\left(\tilde{u}^K(x=j\Delta,n) - u(x=j\Delta,n)\right)^2, \tag{7.5}$$

where $\tilde{u}^K(x,n)$ is the predicted pattern reconstructed from Eq. (7.1) and $u(x,n)$ is the actual pattern from the validation set. As stated before, GA's can be used to predict future values some time steps ahead, without the need of iterating the one-step-ahead predictor (which early becomes useless because of the expected exponential growth of errors). Figure (7.4) shows $\epsilon_q(n)$ as a function of n for $q = 0.16$ calculated from: a) the one-step-ahead prediction formulae obtained from the training set, but applied to obtain the pattern at step n from the previous D values in the validation set; b) iteration of the one-step-ahead formulae starting from the last D data in the training set; c) five-steps-ahead prediction from a formula of the type (7.3) with $T = 5$, obtained by the GA in the training set, and used into the validation set. We see that the improvement in accuracy is notorious when iteration is avoided. We note that the errors in methods a) and c) remain bounded even when n is far from the values from which the prediction formulas were estimated (i.e. the training set $n < 800$). This confirms that the method is not simply fitting data, but rather

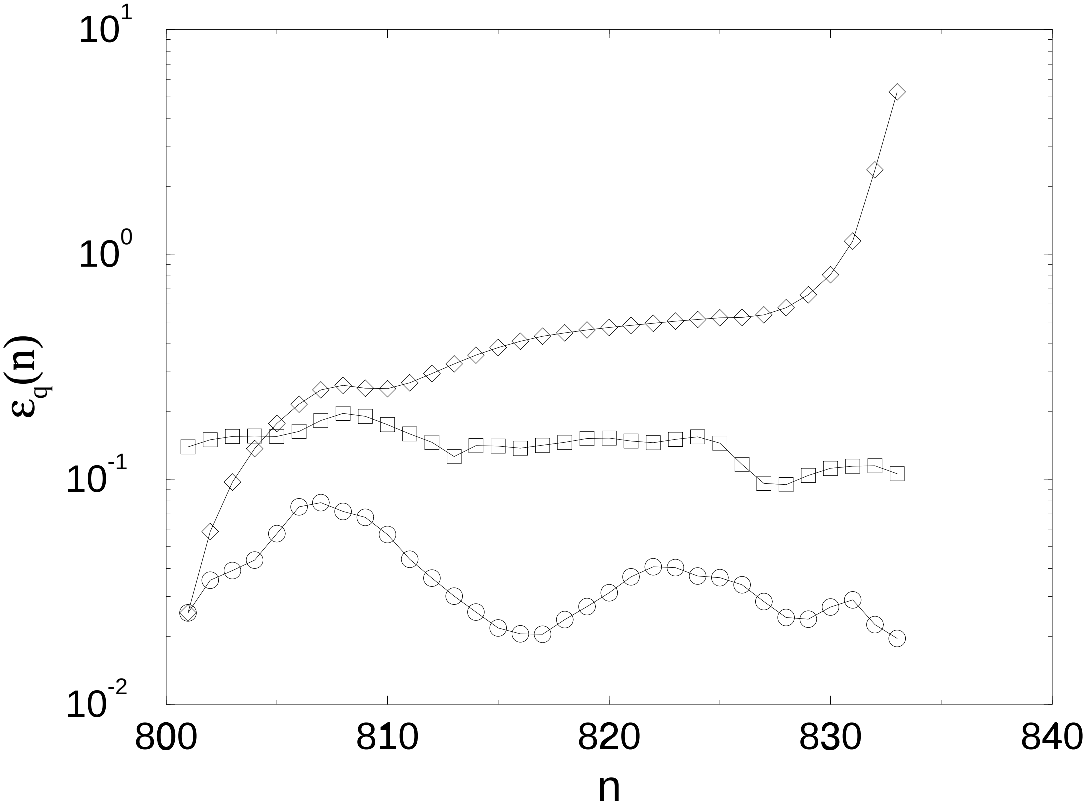

Figure 7.4: Errors as a function of n in the validation set, for $q = 0.16$. Circles: one-step-ahead prediction. Diamonds: iteration of the one-step-ahead formulae starting from the training set ($n \leq 800$). Squares: five-steps-ahead prediction.

it has really found approximate dynamical rules within the deterministic spatiotemporal series.

Figure (7.3) displays the average error $< \epsilon_q >$, which is the temporal average of $\epsilon_q(n)$ with n in the validation range displayed in Fig. (7.4), as a function of q (for one-step-ahead prediction). Despite we are including more EOF's in the reconstruction for decreasing q, the prediction error shows a tendency to increase. This is a consequence of the increase in complexity (and in attractor dimension) of the dynamics by the effective increase in system size ($\approx q^{-1}$). Since we keep the maximum delay D fixed, the embedding of the data set becomes more incomplete at smaller q and the prediction deteriorates. In addition, for smaller q the *confined* or *boundary influenced* character of the spatiotemporal chaos in the system is lost and a description in terms of local structures will be certainly more efficient [92].

7.4 Conclusions

In summary, we have presented a method to forecast the evolution of spatially extended systems based in the combination of POD and GA's. The method performs very well in

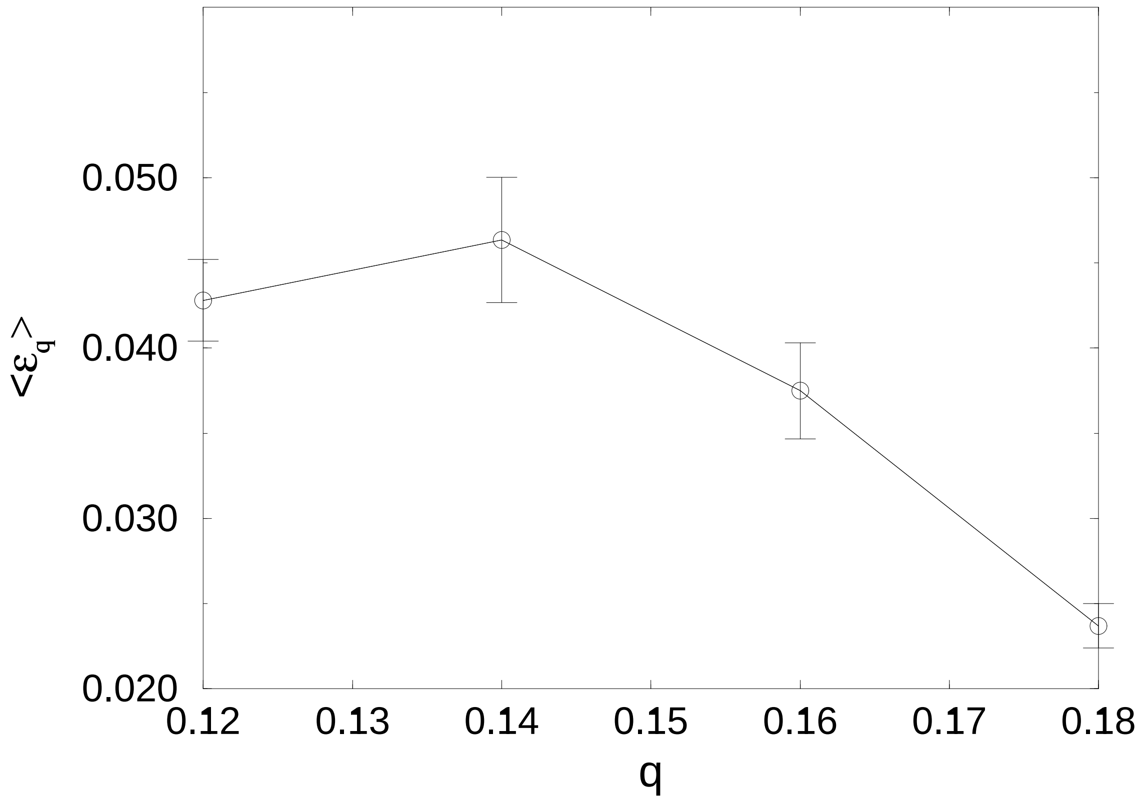

Figure 7.5: Mean error for one-step-ahead prediction in the validation set as a function of q.

situations of confined spatiotemporal chaos as exemplified by the CGLE in a finite interval. We mention here that we are exploring the possibilities of the method for prediction from noisy natural data sets. Results obtained in forecasting Sea Surface Temperature patterns in an area of the Mediterranean Sea are encouraging, and are presented in the next Chapter.

Chapter 8

Forecasting the SST space-time variability of the Alboran Sea with genetic algorithms

We propose a nonlinear ocean forecasting technique based on a combination of genetic algorithms and empirical orthogonal function (EOF) analysis. The method is used to forecast the space-time variability of the sea surface temperature (SST) in the Alboran Sea. The genetic algorithm finds the equations that best describe the behaviour of the different temporal amplitude functions in the EOF decomposition and, therefore, enables global forecasting of the future time-variability.

8.1 Introduction

Traditionally, ocean forecasting is carried out integrating forward in time the equations of motion. This approach usually requires the derivation of the dynamical laws controlling the ocean processes as well as the detailed knowledge of the initial conditions. Unfortunately, this level of knowledge or the computer power needed for the numerical simulation of the ocean is not always accessible. In these cases, an alternative approach to forecast ocean evolution consists in extracting dynamical information directly from the empirical data without imposing an explicit dynamical model. The extracted information about the past of the system is then used to predict its future evolution. The classical techniques in this type of approach consist on modeling the dynamics as a random process, using nondeterministic and linear laws of motion [108]. However, new techniques that explicitly take into account the nonlinear nature of the time evolution are demonstrating a high predictive power. Proposals based on genetic algorithms are beginning to appear in different contexts [94]. Briefly stated, genetic algorithms are methods to solve optimization problems in which the optimal solution is searched through steps inspired in the Darwinian processes of natural selection and survival of the fittest [101]. In the forecasting context, the optimization problem to be solved is to find the empirical model best describing observed past data. The empirical model so obtained may then be used to forecast the future, and may reveal functional relationships underlying the data. Recently, [94] has already shown the robustness of genetic algorithms to forecast the behavior of one-variable chaotic dynamical systems.

The aim of this Chapter is to extend the work of [94] to spatially extended dynamical systems, thus permitting application to real oceanographic data. More explicitly, we focus on using genetic-algorithm methods to predict the space-time variability of the sea surface temperature (SST) of the Alboran Sea. The reasons for this particular election arise from the circulation structure of this basin, the westernmost of the Mediterranean sea, characterized by a wavelike front with two anticyclonic gyres generated by the inflow of Atlantic waters into the Mediterranean through the Strait of Gibraltar [114, 116]. This circulation pattern has a strong signature in the SST field, which provides the chance to observe its space-time variability from satellite imagery.

The Chapter is organized as follows: Section II presents the technique; Section III briefly describes the characteristics of the satellite data employed in this study. The results obtained from the application of the method are shown in Section IV, and Section V concludes the Chapter.

8.2 Nonlinear forecasting of two-dimensional fields with genetic algorithms

The methods of [94] are adequate to forecast the time evolution of one or a small set of variables. Two-dimensional SST fields obtained by satellite imagery are too large for direct application of the technique. A method to encode the time series of satellite images into a smaller set of numbers is thus required. This can be accomplished by using the Empirical Orthogonal Function (EOF) technique [10, 111]. Briefly, EOF analysis decomposes the space-time distributed satellite data into modes ranked by their temporal variance. As a result, a set of spatial modes and associated temporal amplitude functions are obtained. The spatial modes provide information of the spatial structures while the amplitude functions describe their dynamics. The complete state of the system (i.e., the original sequence of satellite images) can be well approximated by simple linear combination of the most relevant spatial modes multiplied by their corresponding amplitude functions [10, 111]. The problem of forecasting the dynamics of a two-dimensional field has thus been reduced to predicting the amplitude functions, a small set of time-series, corresponding to the most relevant EOFs.

The works of [113], [109], and many others have established the methodology for non-linear modeling of chaotic time series. Explicitly, Takens' theorem [113] establishes that given a deterministic time series $\{\mathbf{x}(t_k)\}, t_k = k\Delta t, k = 1, ..., N$ there exists a smooth map P satisfying:

$$\mathbf{x}(t) = P\left[\mathbf{x}(t-\Delta t), \mathbf{x}(t-2\Delta t), \cdots, \mathbf{x}(t-m\Delta t)\right] \tag{8.1}$$

where m is called the embedding dimension obtained from a state-space reconstruction of the time series [107], [91]. Our aim is to obtain with a genetic algorithm the functions $P(\cdot)$ in Eq. (8.1) that best represents the amplitude function associated to each one of the most representative EOFs, and then use them to predict the future state of the system. The algorithm proceeds as follows (for details see [94], [102]): first, for the j-amplitude function, $A_j(t)$, a set of candidate equations (the population) for $P(\cdot)$ is randomly generated. These equations (individuals) are of the form of Eq. (8.1) and their right hand sides are stored in the computer as sets of character strings that contain random sequences of the variable at previous times ($A_j(t-\Delta t), A_j(t-2\Delta t), ..., A_j(t-m\Delta t)$), the four basic arithmetic symbols ($+$,$-$,$\times$, and $/$), and real-number constants. A criterion that measures how well the equation strings perform on a training set of the data is its fitness to the data, defined as the sum of the squared differences between data and forecast from the equation string. The strongest individuals (equation strings with best fits) are then selected to exchange parts of the character strings between them (reproduction and crossover) while the individuals less fitted to the data are discarded. Finally, a small percentage of the equation strings' most basic elements, single operators and variables, are mutated at random. The process is repeated a large number of times to improve the fitness of the evolving population. More details of the algorithm are given in the Appendix B.

In order to minimize the effects of the stochastic components introduced into the amplitude functions by the measurement and environmental noise, and by neglecting the EOFs of small variance in the reconstruction processes, a noise-reduction method based on Singular Spectral Analysis (SSA) or data adaptive approach [110], to be described below, is first applied to the noisest amplitude functions.

8.3 Data

In the present study we have considered a series of 68 monthly averaged SST images of the Alboran Sea, ranging from March-1993 to October-1998. Each monthly image is based on the daily maximum images using the average for every single pixel's position. The monthly composition normally consists of approximately 160 AVHRR-MCSST (Advanced Very High Resolution Radiometer - Multichannel Sea Surface Temperature) passes. Each image is constituted by 415×250 pixels corresponding to a spatial resolution of 1.1 km. Several tests ensure that SST values are derived only for cloud free water surfaces. All pixels flagged as cloud are excluded from all further processing. The data set is available from the German Remote Sensing Data Center (DFD) of the German Aerospace Center (DLR) (You can visit the URL at http://www.dfd.dlr.de/index.html).

8.4 Results

Figure 1a, b, c and d show the mean, 1^{st}, 2^{nd} and 3^{rd} spatial modes respectively obtained from the EOF analysis, while the solid lines in Figure 2 represent the temporal amplitude functions associated with each spatial mode. Basically, the 1^{st} EOF mode captures the variability associated with the seasonal changes in the surface temperature of Atlantic and Mediterranean waters. The 2^{nd} spatial mode appears to be associated with variability in the intensity of the two gyres. Finally, the 3^{rd} mode essentially describes the spatial variability related to the Almeria-Oran Front. These three modes account for 98.64% of the total variance of the data. A Complex EOF analysis of satellite altimetry data in the same area was performed by [115].

The amplitude functions of the 2^{nd} and 3^{rd} EOFs show a time dependence much more complex than the simple seasonal variation displayed by the 1^{st} one. This could be an indication either of complex deterministic evolution or of contamination from random noise. To disentangle both components, the signals were filtered using the SSA method: The filtered time series obtained from the amplitude functions of the 2^{nd} and 3^{rd} EOFs (red dashed lines in Figs. 2b and c) were built considering the first eight and five SSA eigenvalues (that account for 70% and 65% of each amplitude variance) in the respective original time series. The criterion to identify this amount of deterministic variability in each signal was based on a nonlinear prediction approach [112]. Essentially, the signal to be filtered is rebuilt using only a certain number of eigenvalues obtained from the SSA decomposition. Then, the genetic algorithm is employed to find the equation that best fits the data in one part of the dataset, the training set, ranging from March-1993 to June-1998. The predictability skill of the solution equation is then validated with data ranging from July-1998 to October-1998, the validation set, previously unknown for the algorithm. If the forecast performance of the solution equation is high in the validation set (more than 80% of agreement between data and forecast) the rebuilt signal is considered to be mainly deterministic. A new time series is then rebuilt from the original one considering a larger number of eigenvalues and the previous process is repeated. The procedure is stopped when the inclusion of new eigenvalues deteriorates the forecasting skills, since then it can be argued that the variability represented by the new eigenvalues has a strong noisy component. The final filtered signal is thus rebuilt with the maximum number of eigenvalues that provide a good forecast skill in the validation set.

Specific details concerning the algorithm, as well as the resulting empirical equations obtained from it for the three temporal amplitude functions are written in the Appendix B.

Figures 2a, b and c show the results of applying the solution equations. The blue dash-

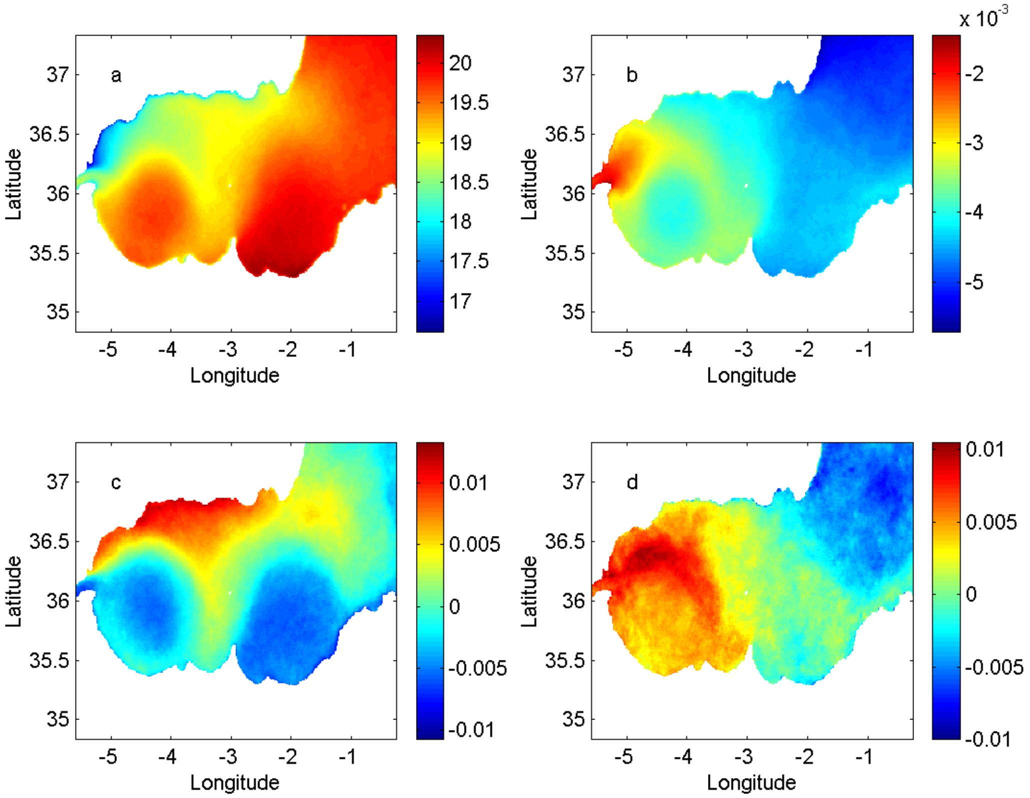

Figure 8.1: a) Mean SST of the Alboran Sea; b), c) and d) shows the 1^{st}, 2^{nd} and 3^{rd} EOF respectively.

dotted line shows the results of applying the solution equation in the training set: all the points in the line are one-month-ahead predictions, i.e. they are obtained from the equations in the Appendix B and the observed values of the (filtered) temporal amplitude at m previous months. Blue circles are the one-month-ahead predicted values in the validation set, i.e., the time interval for which measurements were used in the filtering process but not in the final genetic forecasting.

In order to discriminate if the excellent agreement between data and predictions in the validation set comes from artificial dependencies in the data introduced by the filtering procedure or from an intrinsic dynamical behavior well captured by the evolutionary algorithm, the solution equations are tested in a third set of data called the forecasting set (from November-1998 to January-1999) that has not been used in the filtering process. The crosses are one-month-ahead forecasts in this set of data. The agreement in all cases is excellent, thus indicating that the genetic algorithm has been able to capture the main time variability of each EOF. It is remarkable that this has been achieved without the use of any explicit knowledge of the ocean dynamics, and using data just from the upper layer of the sea.

It remains, to close the procedure, to obtain the total forecasted SST spatial field. This

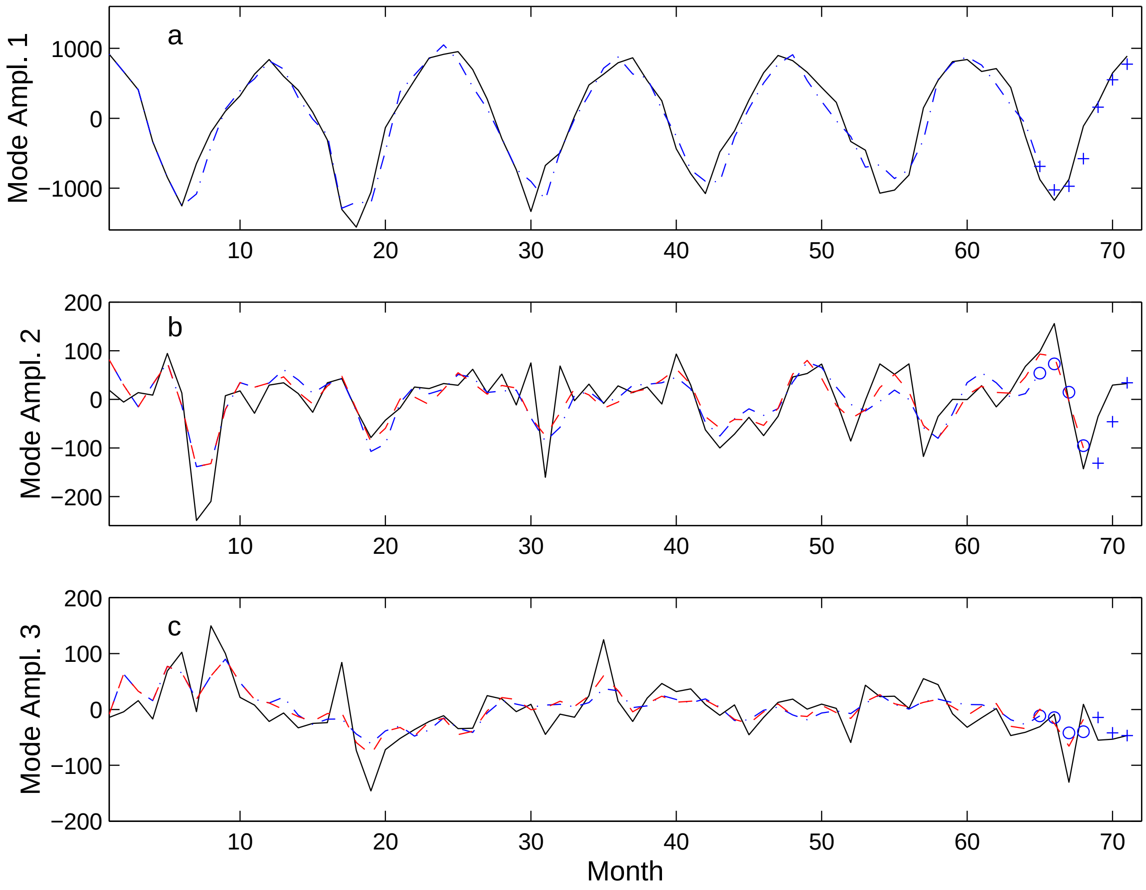

Figure 8.2: a) Amplitude function corresponding to the 1st EOF (solid black line); the blue dash-dotted line shows the results of applying the solution equation in the training set while the crosses are one-month-ahead forecasts in the forecasting data set. b) The solid black line represents the observed amplitude of the 2nd EOF. The red dashed line represents the SSA-filtered mode amplitude. The dash-dotted line represents the fitting of the solution equation to the SSA-filtered mode amplitude in the training set. Circles and crosses represent one-month-ahead forecasts in the validation and forecasting data sets, respectively; c) same as b) but for the 3rd EOF.

is accomplished by adding the three EOFs multiplied by their predicted amplitudes. This has been carried out for the forecasting set. Figures 3a and b show the monthly averaged SST field for November-1998 and the corresponding one-month-ahead forecast. The result correctly reproduces the main SST structure of the gyres in particular and the Alboran Sea in general. The technique slightly overestimates the SST of the two gyres. Since the agreement with the filtered time-series was rather good, this discrepancy should correspond to the part of the observation that has been identified as stochastic by the algorithm. The results obtained for December-1998 are shown in Figures 3c and d. In this case, the forecasted field still keeps a slight signature of the two gyres, a feature that is not found in the real data, although the presence of warm Atlantic waters in the gyre areas is well repro-

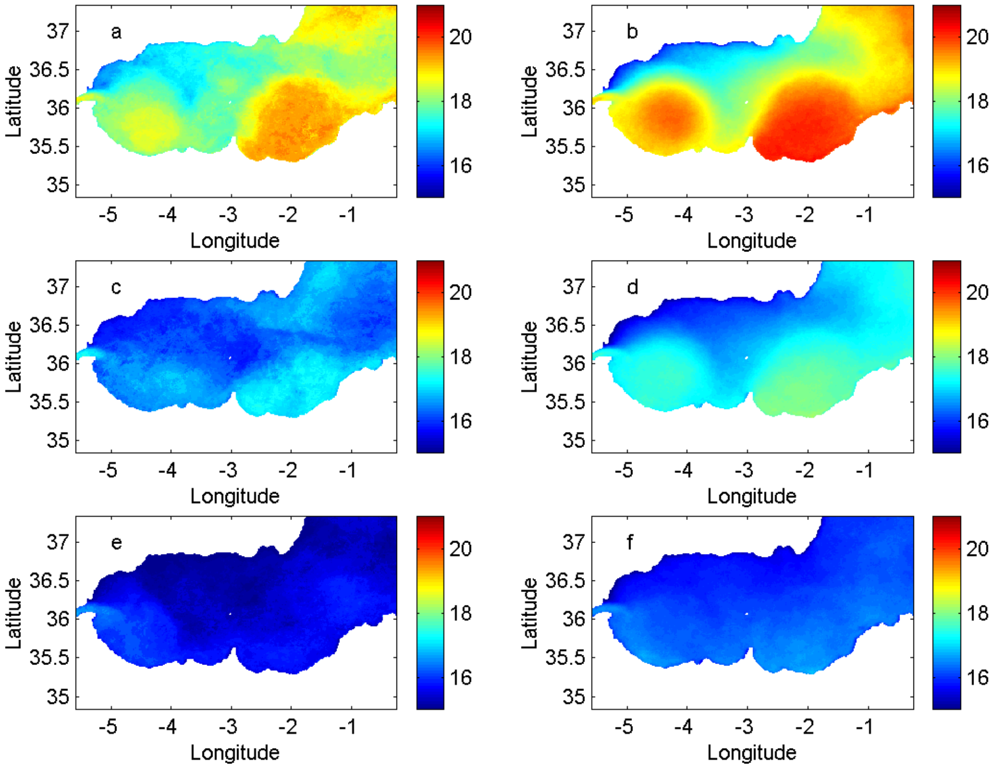

Figure 8.3: a) Monthly mean SST of the Alboran Sea corresponding to November-1998 and b) forecast obtained for November-1998 one month in advance; c) Monthly mean SST of the Alboran Sea corresponding to December-1998 and d) forecast obtained for December-1998; e) Monthly mean SST of the Alboran Sea corresponding to January-1999 and f) forecast obtained for this month.

duced. Finally, Figures 3e and f describe the results obtained for January-1999. The real as well as the forecasted fields show a general cooling of the basin with the disappearance of the Alboran gyres.

8.5 Conclusion

We have proposed a new technique that allows prediction of ocean features using satellite imagery. We first compute the dominant spatial EOF modes from a time series of satellite data, and next we forecast their time evolution using genetic algorithms. A major advantage of employing genetic algorithms versus other non-linear forecasting techniques such as neural networks is that explicit analytical expressions of the dynamical evolution of each EOF are obtained. This feature simplifies the analysis and characterization of the dynamics and provides a powerful operational tool. Besides, genetic algorithms require less user specifications.

The technique has been applied to the one-month-ahead prediction of the SST field of the Alboran sea, and has demonstrated a good performance. We expect the method to perform well in any other situations in which ocean structures are sufficiently permanent for the EOF method to provide large data compression, and in which the dominant EOFs contain a strong deterministic-evolution component as compared to the stochastic one. The method can be applied to any field observable from satellite (SST, dynamic height, surface ocean colour), and the information obtained could be useful for operational needs such as fisheries, naval operations and even for assimilation into numerical models. Future work will extend the technique to track moving structures such as Rossby waves and eddies.

Chapter 9

Summary

Let us briefly conclude this work with the main topics discussed and the principal results obtained. It has become clear that two main parts compose this Thesis. The first one (Chapters 2, 3, 4, and 5) could be entitled *On the Influence of chaotic advection on the spatial structues of reactive substances*, and some of the achievements are outlined in the following:

- In the limit of negligible diffusion the general advection-reaction-diffusion system is equivalent to two coupled dynamical systems: one for the flow dynamics and the other for the reacting dynamics. The coupling between these last dynamical systems is via a spatially unhomogenous source of the reacting subtances.

- The flow is always considered to be turbulent in the Lagrangian frame (with a positive Lyapunov exponent), though laminar in the Eulerian one, and the reacting dynamics is as simple as possible, with a negative Lyapunov exponent.

- Depending on the relative strength (Lyapunov exponents) of the stirring due to the flow and the convergence of the reacting dynamics, two different regimes are observed: a) the spatial pattern of the reacting substances is smooth, that is differentiable everywhere, when the convergence of the reacting dynamics is stronger, and b) the pattern is filamental, that is, fractal or nondifferentiable everywhere and along all directions except one, where it is smooth.

- When a single bulk Lyapunov exponent of the flow is assumed, that is, no fluctuations around its most probable value are considered, the Hölder exponent of the patterns are explicitly calculated in terms of this bulk flow Lyapunov exponent and of the Lyapunov exponent corresponding to the reacting dynamics.

- The above mentioned regimes, i.e. smooth and filamental, appear in both open and chaotic flows. The only difference between these is just that, in the case of open flows, smooth and fractal areas appear interwoven together.

- A more detailed study of the above patterns show their multifractal properties. Multifractality comes from the fluctuations around the bulk value of the finite time Lyapunov exponents. Most importantly the scaling exponents for the structure functions of the spatial patters are strongly affected when chemical activity is considered, and they differ for the exponents calculated in the absence of chemical dynamics.

- All the above considerations can be used to explain the qualitative features of the multifractal structure of the planckton patterns observed in real data.

- The use of maps for the study of advection-reaction-diffusion (in the limit of small diffusivity) systems holds some promise. In particular, the generalisation to study positive chemical Lyapunov exponents (a very difficult task in terms of continuous time description) and other kinds of nontrivial chemistry, may seem easier to study in terms of maps.

- We have also realised that, even in very simple mathematical models, the spatial distribution of predators may follow that of the nutrients, when both are advected by a flow. Moreover, the localisation of nutrients may give rise also to different spatial patterns for the predators.

Concerning the second part, which now could be named as *Modelling and forecasting of spatiotemporal chaotic systems: the role of the coherent structures*, we next summarise some of its attempts and results:

- Analysing real data of the ocean with the POD allows us to identify a moving vortex in a specific geographical area. Then, we have been able to obtain a very simple system of ordinary differential equations suitable to describe the dynamics of this vortex.

- We have introduced a new way to forecasting spatiotemporal time series. This consists in the succesive use of the POD to reduce the full dynamics to a *small* number of time series, which are associated to the modes of the most relevant coherent structures present in the system, and then, with the use of genetic algorithms, predictions of these time series are performed. Finally, the forecasting of the future states of the system is made after recovering the full signal.

- The above technique works well for confined systems displaying spatiotemporal chaos. This is mainly because the number of time series to predict is reasonably small.

- We have applied the forecasting technique to data obtained from numerical simulation of the Complex Ginzburg-Landau equation, and for real data of the Sea Surface Temperature of the Alboran Sea. In both cases, the results are promising.

Finally, if I remit to the introduction where I wanted *to reach some experience in a particular complex system that could be applied to any other one*, the author would like to conclude this work summarising some of these experiences that, at the moment of writing these words, he considers to be the cornerstones of his contributions, though maybe they are wellknown in the scientific community. So, along the first Chapters of this work, the ones corresponding to the first part as defined above, it is clear that putting together very simple flows (nonturbulent in the Eulerian sense) with very simple reactive dynamics (decaying chemistry), can give rise to very complicated spatial patterns of the reacting substances. Moreover, some of the dynamical properties (Lyapunov exponents) of the flow and the reactions play a fundamental role in order to characterise the spatial patterns formed in the system. In addition, in the second part of this Thesis, I have learned that reducing the full complex dynamics of a system to the dynamics of the most relevant coherent structures, can help to understand the evolution of a spatiotemporally chaotic system. And, with the help of this assumption, we have introduced a novel and general technique that could help to make predictions of chaotic extended systems.

Appendix A

Mathematical expression of the coefficient $q_{10,2}$ in (6.12)

If we denote the scalar product by $\{\phi_3, \phi_4\} = \int_A \phi_3(x,y)\phi_4(x,y)dxdy$, and we define also:

$$c_{k,l} = -\{\triangle\phi_k, \phi_l\}, \tag{A.1}$$

$$\begin{aligned} e_{k,l} &= \{-\beta\frac{\partial\phi_k}{\partial x} + \nu\nabla^4\phi_k - \frac{g}{f_0}\frac{\partial <\psi>}{\partial x}\frac{\partial\triangle\phi_k}{\partial y} + \frac{\partial\triangle <\psi>}{\partial y}\frac{\partial\phi_k}{\partial x} \\ &- \frac{\partial <\psi>}{\partial y}\frac{\partial\triangle\phi_k}{\partial x} - \frac{\partial\triangle <\psi>}{\partial x}\frac{\partial\phi_k}{\partial y} - \frac{g}{f_0R_1^2}(U\frac{\partial\phi_k}{\partial x} - V\frac{\partial\phi_k}{\partial y}), \phi_l\}, \end{aligned} \tag{A.2}$$

$$p_{k,l} = \frac{g}{f_0R_1^2}\{\frac{\partial <\psi>}{\partial y}\frac{\partial\phi_k}{\partial x} - \frac{\partial <\psi>}{\partial x}\frac{\partial\phi_k}{\partial y}, \phi_l\}, \tag{A.3}$$

$$\begin{aligned} f_{k,l} &= \{-\frac{f_0}{H_2}(\frac{\partial\tau}{\partial y}\frac{\partial\phi_k}{\partial x} - \frac{\partial\tau}{\partial x}\frac{\partial\phi_k}{\partial y}) - \beta\frac{\partial\phi_k}{\partial x} - C_b\triangle\phi_k + \nu\nabla^4\phi_k \\ &- \frac{g}{f_0}(\frac{\partial\triangle\phi_k}{\partial y}V - \frac{\partial\triangle\phi_k}{\partial x}U) - \frac{g}{f_0R_2^2}(\frac{\partial <\psi>}{\partial y}\frac{\partial\phi_k}{\partial x} - \frac{\partial <\psi>}{\partial x}\frac{\partial\phi_k}{\partial y}), \phi_l\}, \end{aligned}$$

$$h_{k,l} = -\frac{g}{f_0R_2^2}\{V\frac{\partial\phi_k}{\partial y} - U\frac{\partial\phi_k}{\partial x}, \phi_l\}, \tag{A.4}$$

$$\begin{aligned} q_{1,l} &= \{-\frac{g}{f_0}\frac{\partial <\psi>}{\partial x}\frac{\partial\triangle <\psi>}{\partial y} + \frac{g}{f_0}\frac{\partial <\psi>}{\partial y}\frac{\partial\triangle <\psi>}{\partial x} - \frac{g}{f_0R_1^2}U\frac{\partial <\psi>}{\partial x} \\ &+ \frac{g}{f_0R_1^2}V\frac{\partial <\psi>}{\partial y} - \beta\frac{\partial <\psi>}{\partial x} + \nu\nabla^4 <\psi>, \phi_l\}, \end{aligned} \tag{A.5}$$

$$\begin{aligned} q_{2,l} &= \{-\frac{g}{f_0R_2^2}V\frac{\partial <\psi>}{\partial y} + \frac{g}{f_0R_2^2}U\frac{\partial <\psi>}{\partial x} + \frac{f_0}{H_2}U\frac{\partial\tau}{\partial x} \\ &- \frac{f_0}{H_2}V\frac{\partial\tau}{\partial y} - \beta V, \phi_l\}, \end{aligned} \tag{A.6}$$

$$d_{1,l} = -\frac{g}{f_0}\{\frac{\partial\phi_3}{\partial x}\frac{\partial\triangle\phi_3}{\partial y} - \frac{\partial\phi_3}{\partial y}\frac{\partial\triangle\phi_3}{\partial x}, \phi_l\}, \tag{A.7}$$

$$d_{2,l} = -\frac{g}{f_0}\{\frac{\partial\phi_4}{\partial x}\frac{\partial\triangle\phi_4}{\partial y} - \frac{\partial\phi_4}{\partial y}\frac{\partial\triangle\phi_4}{\partial x}, \phi_l\}, \tag{A.8}$$

$$d_{3,l} = \{-\frac{g}{f_0}(\frac{\partial\phi_3}{\partial x}\frac{\partial\triangle\phi_4}{\partial y} - \frac{\partial\phi_3}{\partial y}\frac{\partial\triangle\phi_4}{\partial x} + \frac{\partial\phi_4}{\partial x}\frac{\partial\triangle\phi_3}{\partial y} - \frac{\partial\phi_4}{\partial y}\frac{\partial\triangle\phi_3}{\partial x}, \phi_l\}, \tag{A.9}$$

with $j, l = 3, 4$, we finally obtain,

$$\begin{aligned} q_{10,2} &= \frac{1}{k_1}\Big({R_1}^2{R_2}^4 d_{3,3}c_{4,4}c_{3,4} - {c_{3,3}}^2 d_{3,4}{R_2}^4{R_1}^2 + {R_2}^4 d_{3,3}c_{3,4} + c_{1,2}{R_1}^4 d_{3,4}{R_2}^2 c_{4,3} \\ &+ {R_1}^2{R_2}^2 c_{3,4}d_{3,3} - c_{3,3}{R_1}^2 d_{3,4}{R_2}^2 - c_{4,4}{R_1}^4 c_{3,3}d_{3,4}{R_2}^2 - c_{4,4}{R_1}^2 c_{3,3}{R_2}^4 d_{3,4} \\ &- c_{3,3}{R_2}^4 d_{3,4} + c_{3,4}{R_1}^4 d_{3,4}{R_2}^4 c_{4,3}c_{3,3} - {c_{3,4}}^2{R_1}^4 c_{4,3}{R_2}^4 d_{3,3} + c_{4,4}{R_1}^4 c_{3,3}{R_2}^4 c_{3,4}d_{3,3} \\ &- c_{4,4}{R_1}^4{c_{3,3}}^2 d_{3,4}{R_2}^4 + c_{3,3}{R_2}^4 c_{3,4}{R_1}^2 d_{3,3}\Big)\,. \end{aligned} \tag{A.10}$$

Where

$$\begin{aligned} k_1 &= -2c_{4,3}{R_2}^2 c_{3,4}{R_1}^2 + {c_{4,4}}^2{R_2}^2{R_1}^4 c_{3,3} + {c_{4,4}}^2{R_2}^4{R_1}^2 c_{3,3} + {c_{4,4}}^2{R_2}^4{R_1}^4{c_{3,3}}^2 \\ &+ c_{4,4}{R_1}^4 c_{3,3} - c_{4,4}{R_1}^4 c_{4,3}{R_2}^2 c_{3,4} + 2c_{4,4}{R_1}^2 c_{3,3}{R_2}^2 + c_{4,4}{R_1}^4{c_{3,3}}^2{R_2}^2 - c_{4,3}{R_2}^2 c_{3,4}{R_1}^4 c_{3,3} \\ &+ {c_{4,3}}^2{R_2}^4{c_{3,4}}^2{R_1}^4 - c_{4,3}{R_2}^4 c_{3,4}{R_1}^2 c_{3,3} - c_{4,4}{R_2}^4 c_{4,3}c_{3,4}{R_1}^2 + c_{4,4}{R_2}^4 c_{3,3} + c_{4,4}{R_2}^4{c_{3,3}}^2{R_1}^2 \\ &- c_{3,4}{R_1}^4 c_{4,3} - 2c_{4,4}{R_2}^4 c_{3,4}{R_1}^4 c_{4,3}c_{3,3} - c_{3,4}{R_2}^4 c_{4,3} \end{aligned} \tag{A.11}$$

Appendix B

Analytical expressions for EOF amplitude functions

The values of the parameter m are $m = 6, 12$ and 12 for the 1^{st}, 2^{nd} and 3^{rd} EOF respectively and the maximum number of symbols allowed for each tentative equation is 20. Each generation consists of a population of 120 randomly generated equations. A number of 10000 generations are considered in each run of the genetic algorithm, requiring around 120 seconds of CPU time on an Alpha-XP1000 workstation (the previous step of EOF decomposition takes approximately 145 seconds on a SGI computer with a MIPS R10000 processor). More details on the genetic code can be found in [102]. The solutions obtained for the 1^{st}, 2^{nd} and 3^{rd} amplitude functions are the following expressions:

$$\begin{aligned} A_1(t) = 0.33\,\{2\,A_1(1) - [A_1(3) + A_1(6) + (A_1(1) \\ \left[A_1(2)^{-1}\,(9.3 - A_1(1)) - 3.78\right]^{-1}\Big)\Big]\Big\}\,. \end{aligned} \tag{B.1}$$

$$\begin{aligned} A_2(t) \quad &= A_2(1) - A_2(2) - 0.134\,\{A_2(4) - (A_2(5) \\ &-\; A_2(12) - 3.45\,[A_2(5) + A_2(8)])\}\,. \end{aligned} \tag{B.2}$$

$$\begin{aligned} A_3(t) \;&=\; 0.4A_3(12) - 0.4 - 0.59\,[2.5 - A_3(3) \\ &+\; A_3(9) - A_3(1)]\,. \end{aligned} \tag{B.3}$$

In the expressions above, $A_1(1)$, $A_3(12)$, etc... are shortcuts for $A_1(t-1)$, $A_3(t-12)$, etc..., where time is in months.

Bibliography

[1] E.N. Lorentz, J. Atmos. Sci. **29**, 130 (1963).

[2] J. Pedlosky, *Geophysical Fluid Dynamics (2nd edition)*. Springer-Verlag, New York, 1987.

[3] B. Cushman-Roisin, *Introduction to Geophysical Fluid Dynamics*. Prentice-Hall, New Jersey, 1994.

[4] E. Ott, *Chaos in Dynamical Systems*, Cambridge Univ. Press, Cambridge, 1993.

[5] A. Crisanti, M. Falcioni, G. Paladin and A. Vulpiani, Riv. Nuov. Cim. **14**, 1 (1991); J.H.E. Cartwright, M. Feingold and O. Piro, *An introduction to chaotic advection* in *Mixing: Chaos and Turbulence*, H. Chaté, E. Villermaux, and J.-M. Chomaz, eds., Kluwer Academic/Plenum Publishers, New York, 1999.

[6] H. Aref, J. Fluid Mech. **143**,1 (1984); J. M. Ottino, *The kinematics of mixing: stretching, chaos and transport*, Cambridge University Press, Cambridge, 1989; S. Wiggins, *Chaotic transport in dynamical systems*, (Springer-Verlag, 1991); *Chaos applied to fluid mixing* Ed. H. Aref, M. S. El Naschie, Pergamon/Elsevier, 1995.

[7] J. Guckenheimer and P. Holmes, *Nonlinear Oscillations, Dynamical systems, and Bifurcations of Vector Fields*, Springer-Verlag, New York, 1983.

[8] A.J. Lichtenberg and M.A. Lieberman, *Regular and Chaotic Dynamics*, Springer-Verlag, New York, 1992.

[9] A. M. Ozorio de Almeida, *Hamiltonian Systems: Chaos and Quantization*, Cambridge University Press, New York, 1988.

[10] P. Holmes, J.L. Lumley and G. Berkooz, *Turbulence, Coherent Structures, Dynamical Systems and Symmetry*, Cambridge University Press, Cambridge, 1996; P. Holmes, J.L. Lumley, G. Berkooz, J.C. Mattingly, and R.W. Wittenberg, Phys. Rep. **287**, 337 (1997); G. Berkooz, P. Holmes, and J.L. Lumley, Annu. Rev. Fluid Mech. **25**, 539 (1993).

[11] M. Kirby, Physica D **57**, 466 (1992).

[12] F. Kwasniok, Phys. Rev. E **55**, 5365 (1997).

[13] G. Berkooz, *PhD. Thesis*, Cornell University, 1997.

[14] H. Lipson and J. B. Pollack, Nature **406**, 974 (2000); M. J. B. Krieger, J. B. Billeter and L. Keller, Nature **406**, 992 (2000).

[15] N. Goldenfeld and L. Kadanoff, Science **284**, 87 (1999).

[16] I. R. Epstein, Nature **374**, 321 (1995).

[17] I. M. Sokolov, A. Blumen, Int. J. Mod. Phys. B **5**(20), 3127 (1991).

[18] E. R. Abraham, Nature **391**, 577 (1998).

[19] S. Edouard, B. Legras, F. Lefèvre and R. Eymard, Nature **384**, 444 (1996); D. W. Waugh et. al, J. Geophys. Res. **99**, 1071 (1994).

[20] G. Metcalfe and J.M. Ottino, Phys. Rev. Lett. **72**, 2875 (1994).

[21] R. Reigada, F. Sagués, I. M. Sokolov, J. M. Sancho and A. Blumen, Phys. Rev. Lett. **78**, 741 (1997).

[22] Z. Toroczkai, Gy. Károlyi, Á. Péntek, T. Tél and C. Grebogi, Phys. Rev. Lett. **80**, 500 (1998).

[23] C. Jung, T. Tél and E. Zemniak, Chaos **3**, 555 (1993); A. Péntek, Z. Toroczkai, T. Tél, C. Grebogi and J.A. Yorke, Phys. Rev. E **51**, 4076 (1995).

[24] Y. Kuramoto, *Chemical Oscillations, Waves and Turbulence*, Springer Verlag, Berlin, 1984.

[25] a similar computational method has been used for the passive tracer problem in F. Városi, M. Antonsen and E. Ott, Phys. Fluids A **3**, 1017 (1991).

[26] D. L. Turcotte, *Fractals and chaos in geology and geophysics*, Cambridge University Press, Cambridge, 1997.

[27] S. K. Scott, *Chemical chaos*, Oxford University Press, 1991.

[28] L. Matthews and J. Brindley, Dynamics and Stability of Systems **12**(1), 39 (1997).

[29] C. Marguerit, D. Schertzer, F. Schmmitt and S. Lovejoy, J. Mar. Sys. **16**, 69 (1998).

[30] G. Metcalfe and J.M. Ottino, Phys. Rev. Lett. **72**, 2875 (1994).

[31] J.-P. Eckmann and D. Ruelle, Rev. Mod. Phys. **57**, 617 (1985).

[32] E. Abraham, *A note on the wavenumber spectra of sea-surface temperature and chlorophyll*, preprint (1999).

[33] E. Ziemniak, C. Jung and T. Tél, Physica D **76**, 123 (1994).

[34] T. Tél, in *Directions in Chaos*, Vol. 3, edited by Hao Bai-Lin, World Scientific, Singapore, 1990.

[35] J.C. Sommerer, H.-C. Ku and H.E. Gilreath, Phys. Rev. Lett. **77**, 5055 (1996).

[36] T. Bohr, M. Jensen, G. Paladin and A. Vulpiani, *Dynamical Systems Approach to Turbulence*, Cambridge Univ. Press, Cambridge, 1998.

[37] K. Nam, T.M. Antonsen, Jr., P.N. Guzdar and E. Ott, Phys. Rev. Lett. **83**, 3426 (1999).

[38] T. M. Antonsen, Jr. Z. F. Fan and E. Ott, Phys. Rev. Lett. **75**, 1751 (1995).

[39] M. Chertkov, Phys. Fluids **10**, 3017 (1998); `chao-dyn/9803007`.

[40] E. Ott and T. M. Antonsen, Jr., Phys. Rev. Lett. **61**, 2839 (1988); Phys. Rev. **A 39**, 3660 (1989).

[41] T. M. Antonsen, Jr. and E. Ott, Phys. Rev. A **44**, 851 (1991).

[42] M. Falcioni, G. Paladin and A. Vulpiani, Phys. Rev. Lett., **64**, 698 (1990); E. Ott, T.M. Antonsen Jr., Phys. Rev. Lett., **64**, 699 (1990).

[43] G.-C. Yuan, K. Nam, T. M. Antonsen, Jr., E. Ott and P. N. Guzdar, *Power spectrum of passive scalars in two-dimensional chaotic flows*, CHAOS .

[44] M. Chertkov, Phys. Fluids **11** 2257 (1999); `chao-dyn/9809010`.

[45] J.T. Bacmeister, S.D. Eckermann, L. Sparling, K. Roland, M. Loewenstein and M.H. Profitt, *Analysis of intermittency in aircraft measurements of velocity, temperature and atmospheric tracers using wavelet transforms*, In: Gravity Wave Processes: Their Parameterization in Global Climate Models, ed. K. Hamilton; Heidelberg, Springer-Verlag, 85, (1997).

[46] A.F. Tuck and S.J. Hovde, Geophys. Res. Lett. **26**, 1271 (1999).

[47] L. Seuront, F. Schmitt, Y. Lagadeuc, D. Schertzer, S. Lovejoy and S. Frontier, Geophys. Res. Lett. **23**, 3591 (1996).

[48] I. Scheuring, G. Károlyi, Á. Péntek, T. Tél and Z. Toroczkai, *A model for resolving the plankton paradox: coexistence in open flows*, Freshwater Biology, (to appear, 1999).

[49] A.S. Bower, J. Phys. Oceanogr. **21**, 173 (1991).

[50] M. Cencini, G. Lacorata, A. Vulpiani and E. Zambianchi, J. Phys. Ocean. **29**, 2578 (1999); chao-dyn/9801027.

[51] K.L. Denman and A.E. Gargett, Annu. Rev. Fluid Mech. **27**, 225 (1995).

[52] P. H. Haynes, *Transport, stirring and mixing in the atmosphere* in *Mixing: Chaos and Turbulence*, H. Chaté and E. Villermaux (eds.), Kluwer, Dordretch, 1999.

[53] S.A. Levin and L.A. Segel, Nature **259**, 659 (1976).

[54] D.L. Mackas, K.L. Denman and M.R. Abbott, Bull. Mar. Sci., **37**, 652 (1985).

[55] J.D. Mahlman, D.G. Andrews, D.L. Hartmann, T. Matsuno and R.G. Murgatroyd, *Transport of trace constituents in the stratosphere*. In Dynamics of the Middle Atmosphere, ed. J. Holton and T. Matsuno; Tokyo, Terrapub, Dordrecht, Reidel, 387 (1984); J.D. Mahlman, H. Levy II and W.J. Moxim, J. Geophys. Res., **91**, 2687 (1986).

[56] M. Pascual, F.A. Ascioti and H. Caswell, J. Plankton Res., **17**, 1209 (1995).

[57] Á. Péntek, T. Tél and Z. Toroczkai, J. Phys. **A 28**, 2191 (1995).

[58] J. H. Steele (ed.). *Spatial pattern in plankton communities.* Plenum Press, New York, 1978.

[59] M.J.R. Fasham, Oceanogr. Mar. Biol. Ann. Rev., **16**, 43 (1978).

[60] J.H. Steele and E.W. Henderson, Phil. Trans. R. Soc. Lond. B, **343**, 5 (1994).

[61] L. Mazzella, M.C. Buia, M.C. Gambi, M. Lorenti, G.F. Russo, M.B. Scipione and V. Zupo, *Plant-animal trohic relationships in the Posidonia Oceanica ecosystem of the Mediterranean Sea: a review*, in: D.M. John, S.J. Hawkins and J.H. Price (eds) Plant-animal interactions in the marine benthos, Clarendon Press, Oxford, 165, 1992.

[62] I.R. Jenkinson and B.A. Biddanda, Journal of Plankton Research, **17**, 2251 (1995).

[63] I.R. Jenkinson, T. Wyatt and A. Malej, Progress and Trends in Rheology **5**, 57 (1998).

[64] J.H.E. Cartwright, M. Feingold and O. Piro, Physica D **76**, 22 (1994).

[65] V. Loreto, G. Paladin, M. Pasquini and A. Vulpiani, Physica A **232**, 189 (1996).

[66] C.-H. Lai, Changsong Zhou, Europhys. Lett. **43**, 376 (1998).

[67] R. Toral, C.R. Mirasso, E. Hernández-García and O. Piro *Synchronization of Chaotic Systems by Common Random Forcing* in *Unsolved Problems of Noise and Fluctuations: UPON'99, Second international conference.* D. Abbot, L. Kish, editors, AIP, Melville, 2000.

[68] C. Canuto, M. Y. Hussaini, A. Quarteroni and T. A. Zang, *Spectral methods in fluid dynamics*, Springer-Verlag, New York, 1988.

[69] J.L. Lumley, *Stochastic Tools in Turbulence* , Academic Press, New York, 1971.

[70] R. W. Preisendorfer, *Principal Component Analysis in Meteorology and Oceanography*, Elsevier, Amsterdam, 1988.

[71] A. Palacios, D. Armbruster, E.J. Kostelich, and E. Stone, Physica D **96**, 132 (1996).

[72] F. Qin, E.E. Wolf, and H.-C. Chang, Phys. Rev. Lett. **72**, 1459 (1994).

[73] A.E. Deane, I.G. Kevrekidis, G.E. Karniadakis, and S.A. Orszag, Phys. Fluids A **3**, 2337 (1991).

[74] R.A. Sahan, A. Liakopoulos, H. Gunes, Phys. Fluids **9**, 551 (1997).

[75] N. Aubry, P. Holmes, J.L. Lumley, E. Stone, J. Fluid Mech. **192**, 115 (1988).

[76] N. Aubry, P. Holmes, J.L. Lumley, E. Stone, Physica D **37**, 1 (1989).

[77] M. Ghil, *Dynamic Meteorology: Data Assimilation Methods*, Springer-Verlag, New York, 1981.

[78] K. Hasselmann, J. Geophys. Res. **93**, 11015 (1988).

[79] C. Uhl, R. Friedrich, and H. Haken, Phys. Rev. E **51**, 3890 (1995).

[80] U. Achatz, G. Schmitz, and K.-M. Greisiger, J. Atmos. Sci. **52**, 3201 (1995).

[81] F. Kwasniok, Physica D **92**, 28 (1996).

[82] See the different numbers of the AVISO Newsletter, available on-line at `http://sirius-ci.cst.cnes.fr:8090/HTML/information/general/welcome.html`.

[83] The MSLA products are supplied by the CLS Space Oceanography Division (France), with financial support from the CEO programme (Center for Earth Observation) and Midi-Pyrénées regional council. CD ROMs are produced by the AVISO/Altimetry operations center. The ERS products were generated as part of the proposal *Joint analysis of ERS-1, ERS-2 and TOPEX/POSEIDON altimeter data for oceanic circulation studies* selected in response to the Announcement of Opportunity for ERS-1/2 by the European Space Agency (Proposal code: A02.F105); P. Y. Le Traon, J. Stum, J. Dorandeu, P. Gaspar and P. Vincent, J. Geophys. Res. **99**, 24619 (1994); P. Y. Le Traon and F. Ogor, J. Geophys. Res. **103**, 8045 (1998).

[84] U. End, J. Font, G. Kraichman, C. Millot, M. Rhein and J. Tintoré, Prog. Oceanog. **44**, 37 (1999).

[85] C. Bouzinac, J. Vazquez and J. Font, J. Geophys. Res. **103**, 8059 (1998).

[86] G. R. North, T. L. Bell, R. R. Cahalan and F.J. Moeng, Mon. Wea. Rev. **110** (1982).

[87] C. Bouzinac, *PhD. Thesis*, U. Pierre et Marie Curie, Paris, 1997.

[88] F. P. Bretherton and M. Karweit, National Academy of Science, 237 (1983).

[89] M. Lesieur, *Turbulence in Fluids*. Kluwer, Dordretch, 1990.

[90] J. Guckenheimer, A. Back, J. Guckenheimer, M. Myers, F. Wicklin and P. Worfolk, Notices of the American Mathematical Society, **39**, 303 (1992).

[91] H.D.I. Abarbanel, *Analysis of Observed Chaotic Data* (Springer-Verlag, Berlin, 1996). H. Kantz and T. Schreiber, *Nonlinear Time Series Analysis*, Cambridge University Press, Cambridge, 1997.

[92] U. Parlitz and G. Mayer-Kress, Phys. Rev. E **51**, R2709 (1995); U. Parlitz and C. Merkwirth, Phys. Rev. Lett. **84**, 1890 (2000).

[93] S. Ørstavik and J. Stark, Phys. Lett. A **247**, 145 (1998).

[94] G.G. Szpiro, Phys. Rev. E **55**, 2557 (1997).

[95] V.K. Yadavalli, R.K. Dahule, S.S. Tambe, and B.D. Kulkarni, CHAOS **9**, 789 (1999).

[96] B.J. Gluckman, C.B. Arnold and J.P. Gollub, Phys. Rev. E **51**, 1128 (1995); L. Ning, Y. Hu, R.E. Ecke and G. Ahlers, Phys. Rev. Lett. **71**, 2216 (1993).

[97] S.M. Zoldi, J. Liu, K.M.S. Bajaj, H.S. Greenside and G. Ahlers, Phys. Rev. E **58**, R6903 (1998).

[98] V.M. Eguíluz, P. Alstrøm, E. Hernández-García and O. Piro, Phys. Rev. E **59**, 2822 (1999).

[99] M. Meixner, S.M. Zoldi, S. Bose and E. Schöll, Phys. Rev. E **61**, 1382 (2000).

[100] L. Sirovich, Physica D **37**, 126 (1989); J.D. Rodriguez and L. Sirovich, Physica D **43**, 77 (1990); L. Sirovich, J.D. Rodriguez and B. Knight, Physica D **43**, 63 (1990).

[101] J. H. Holland, *Adaptation in natural and artificial systems*, University of Michigan Press, Ann Arbor, 1992.

[102] A. Álvarez, A. Orfila, and J. Tintoré, preprint, 2000.

[103] The parameters c_0 and ρ of the notation of Sirovich et al. [100] are related to ours by $c_0 = 1/\alpha$, and $\rho = -1/\beta$. Their time and space variables need to be multiplied by factors ρ and $\sqrt{\rho/c_0}$, respectively, to obtain our time and space variables.

[104] Our parameter regime leads to the so-called 'defect chaos' in the large-size limit. See B.I. Shraiman, A. Pumir, W. van Saarloos, P.C. Hohenberg, H. Chaté, and M. Holen, Physica D **57**, 241 (1992).

[105] S. Zoldi and H. Greenside, Phys. Rev. Lett. **78**, 1687 (1997).

[106] To find each of the temporal amplitude predictors takes about 400 seconds of CPU time in a AlphaStation 600s/333.

[107] H.D.I. Abarbanel, R. Brown, J. Sidorowich, and L. S. Tsimring, Rev. Mod. Phys. **65**, 1331 (1993).

[108] A. Barnston and C. F. Ropelewski, J. Climate **5**, 1316 (1992).

[109] M. Casdagli, Physica D **35** 335 (1989).

[110] C. Penland, M. Ghil, and K. M. Weickmann, J. Geophys. Res. **96**, 22659 (1991).

[111] R. W. Preisendorfer, *Principal Component Analysis in Meteorology and Oceanography*, Elsevier, The Netherlands, 1988.

[112] A. A. Tsonis and J. B. Elsner, Nature **358**, 217 (1991).

[113] F. Takens, in *Dynamical systems and turbulence*, edited by D. Rand and L. S. Young, Springer-Verlag, Berlin, 1981.

[114] J. Tintoré, D. Gomis, S. Alonso, and G. Parrilla, J. Phys. Oceanogr. **21**, 811 (1991).

[115] J. Vázquez-Cuervo, J. Font, and J. J. Martínez-Benjamín, J. Phys. Oceanogr. **26**, 1426 (1996).

[116] A. Viúdez, J. Tintoré, and R. L. Haney, J. Phys. Oceanogr. **26**, 684 (1996).